DESIGN AND SIMULATION OF A COMPACT RADIATING SYSTEM FOR HIGH POWER MICROWAVES IN THE 4 TO 6 GHZ RANGE

A Thesis

presented to

the Faculty of the Graduate School

at the University of Missouri-Columbia

In Partial Fulfillment

of the Requirements for the Degree

Master of Science

By

ERIK C. BECKER

Dr. Scott Kovaleski, Thesis Supervisor

MAY 2011

The undersigned, appointed by the dean of the Graduate School, have examined the thesis entitled

DESIGN AND SIMULATION OF A COMPACT RADIATING SYSTEM FOR HIGH POWER MICROWAVES IN THE 4 TO 6 GHZ RANGE

presented by Erik C. Becker,

a candidate for the degree of master of science,

and hereby certify that, in their opinion, it is worthy of acceptance.

Dr. Scott Kovaleski, Thesis Supervisor
Electrical and Computer Engineering

Dr. John Gahl
Chemical Engineering

Dr. Naz Islam
Electrical and Computer Engineering

Acknowledgements

First and foremost, I would like to thank my advisor, Dr. Scott Kovaleski, for his guidance and leadership throughout my graduate career. Especially, thank you for persuading me to pursue graduate school by presenting me with an opportunity I would enjoy. I would also like to thank Dr. John Gahl for his additional guidance. I thank him, as well as Dr. Naz Islam, for their insightful comments and suggestions regarding my research.

I would also like to thank my fellow researchers, present and past, who I have worked with over the past two years. Thank you Brian for offering your time that you didn't always have, and trying to turn me into a morning person. I would like to thank Jim, Dan, Emily, Brady, Alec, and Andy for your friendship, help, advice, and camaraderie over the last two years.

Additionally, thank you to my parents and grandparents for all the guidance, love, and support you have provided throughout my life. Thank you to my brother, sisters, aunts, and uncles for all your support. Thank you Courtney for your patience and support.

Contents

List of Figures

List of Tables

Chapter 1

Introduction

High power microwave technology is the result of the confluence of several scientific discoveries dating back to 19th century. Ultra high frequency (UHF) radio waves were first generated artificially by Heinrich Hertz in the late 1800s. His discovery led to the invention of low frequency radio in the early 20th century. Higher frequency radio followed in the 1930s through the coupling of resonant cavities to electrical circuits. An explosion of microwave technology occurred during World War II, which included the development of the magnetron and the invention of the traveling wave tube and backward wave oscillator. By the 1970s, there was strong emergence of lower-power, but compact, solid-state based microwave sources.

In plasma physics, scientists were putting effort toward controlling thermonuclear fusion for energy production in the 1950s. These efforts led to a detailed understanding

of the interaction between particles and waves. It ultimately led to the requirement for new microwave tube developments using gyrotrons for higher average power at frequencies approaching to over 100 GHz. In the 1960s, electrical technology was further expanded with the introduction of pulsed power. Pulsed power led to the production of charged particle beams with currents exceeding 10 kA at voltages of 1 MV or more. These beams were used to simulate the effects of nuclear weapons, explore inertial confinement fusion, and open the door to other high energy density physics experiments. The availability of intense relativistic beams, coupling with the knowledge gained of wave-particle interaction from plasma physics, opened the door to the generation of high power microwaves [1],[2].

The first high power microwave sources were improved versions of conventional microwave sources, such as the magnetron, backward wave oscillator, and traveling wave tube. Higher powers were achieved by operating at higher currents as well as stronger wave-particle coupling in the interaction region. New sources were created by utilizing high voltage from a pulsed power system to generate relativistic electron beams. The availability of these high energy beams led to the development of three notable sources: the relativistic klystron, gyrotron, and virtual cathode oscillator (vircator) [1].

High power microwave sources are connected to a radiating system which shapes the radiation characteristics for a desired application. Often times a mode converter is placed between the source and the antenna to obtain a particular mode. These devices convert TE to other TE modes, TE to TM, or vice versa. They also have the ability to convert between circular and rectangular waveguide geometries [1], [3]. The goal of

these devices is to convert from the optimal microwave generation mode to the optimal radiating mode.

High power microwave antennas are a direct extrapolation of conventional antenna technology with an allowance for high electric fields and shorter pulses. The type of antenna for a given high power microwave system is dependent on the desired frequencies and radiation characteristics, which include radiation pattern and directive gain. Antennas can be grouped based on the bandwidth of the source. Many microwave sources, such as the magnetron and vircator, are narrowband. The most common narrowband antenna is the horn (pyramidal, conical and TEM) because of its ability to easily couple to a waveguide [1], [4], [5]. The Vlasov and helical antennas are also well suited for narrowband operation [1], [6]. Other systems that have very short microwave pulses are considered ultrawideband, and require special antennas. A parabolic dish antenna called the Impulse Radiating Antenna (IRA) is the leading radiator for ultrawideband systems at this time [1], [7], [8]. The selection of a high power microwave antenna is highly dependent on the application, the microwave source, and the radiating frequencies.

The development of high power microwave sources and radiators has led to numerous technologies including plasma heating, high power radar, particle acceleration, space propulsion, power beaming, active denial, IED neutralization, and microwave weapons [1], [2], [9-11]. Microwave weapons are of interest to the military because they are non-lethal to humans, produce little collateral damage, have little sensitivity to atmospheric conditions, can enter through the front or back door, and cost little compared to conventional munitions [1]. They have the ability to produce physical damage to

electronics, temporally disrupt electronics, jam microwave and RF receivers, as well as deceive electronic systems. Active denial systems use beamed microwave energy that inflicts pain without actually injuring a person. This system can be used to disperse out of control crowds or prevent unauthorized personal from entering a prohibited area. High power microwaves are also envisioned to be used to destroy the circuits in an IED, or jam the detonating device. Ultrawideband high power microwave systems are used for high power radar because of high power transmission at very short pulses. Using high power microwaves for radar applications will increase the maximum detection range and address some of radar's basic limitations [9]. Power beaming is being explored because it is believed that large amounts of energy can be transferred between Earth and space. High power microwaves have also been used to heat plasmas to thermonuclear temperatures, in hope to find a new clean energy source through controlled thermonuclear fusion. The method of heating currently receiving the most attention is electron cyclotron resonance heating. The interaction of electrons and high power microwaves is also used in particle accelerators. The goal is to use high power microwaves to accelerate beams with energies of greater than 1 TeV that will explore high-energy physics theories that include the discovery of the elusive Higgs particle, supersymmetry, and string theory [1].

As these technologies evolve, the demands from some of these areas are calling for the development of more compact devices, which is especially true in military applications. This trend is evident from the numerous recent publications on the advancing technology of compact high power microwave sources [12-23]. Texas Tech University has recently developed a compact high power microwave source. It is

composed of a compact triode vircator that is driven by either a low impedance Marx generator or flux compression generator [24]. The viractor is six inches in diameter and eleven inches long. As discussed, the device utilizes a high energy electron beam. The beam is created by a positively driven anode and grounded cathode in the center of the 6 x 11 inch cavity. The cathode is made of solid aluminum with machined grooves. The anode is a 70% transparent honeycomb structure made of stainless steel. Electrons from the cathode travel toward the anode. Many of them will pass to the other side of the anode because of its transparency. The space charge limit is exceeded in the anode to grounded cavity wall region, and a virtual cathode is formed. The virtual cathode oscillates at roughly the beam plasma frequency as the amount of charge in the gap varies over time. The electron movement produces electromagnetic waves, predominately in the TE_{11} mode, correlating to the virtual cathode oscillation [1].

The output of the vircator starts at very low magnitudes at just over 2 GHz. The frequency then chirps up from 4 GHz up to 7 GHz as the diode current increases. The highest magnitudes of power output from the device are in the 4 to 6 GHz range, but the peak power and output waveforms vary considerably from shot to shot. The maximum estimated peak power output from the viractor to date is 135 MW, but it is not uncharacteristic to get power levels in the 50 MW range for a shot [24].

Currently, the radiation pattern of the vircator developed at Texas Tech is not known. As a result, the total radiated power measurements are rough estimates due to a fairly crude approximation of the radiation pattern. A compact radiating system is needed for the vircator that produces known radiation characteristics. The goal of this system is to maximize power transfer of the TE_{11} mode from the vircator into a forward

directed one main lobe radiation pattern that has a directivity of approximately 10-15 dB. The radiating system must be no larger than 6 inches (15.24 cm) in diameter and be as short as possible in the longitudinal direction. This thesis presents the research performed at the University of Missouri of the design and simulation of the compact radiating system for the Texas Tech vircator. A diagram of the system is shown in Figure 1.1.

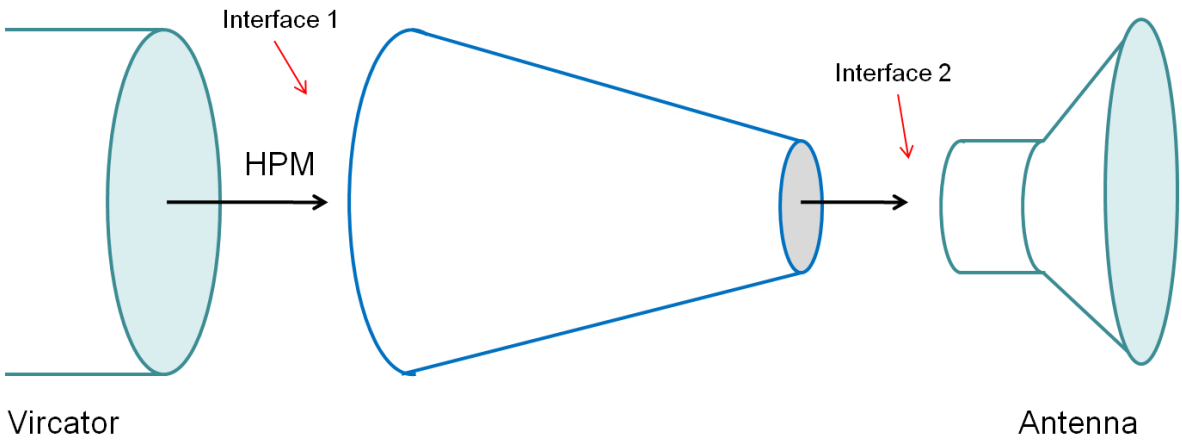

Figure 1.1: System layout of the vircator and compact radiating system.

Simulations on the system were completed using COMSOL Multiphysics, a software that implements the finite element method. This method is a numerical technique for obtaining an approximate solution to a field problem by converting the governing differential equations into a set of linear algebraic equations [25]. The domain is discretized in many small elements, referred to as finite elements. The equations obtained for each element, which include domain and boundary conditions, are assembled together with adjoining elements to form the global finite element equations for the entire domain [26],[27]. An equation solver is then used to solve the system of

equations to arrive at an approximate solution of the problem. The solutions of these equations dictate the answer to the design questions of the compact radiating system.

This thesis begins by detailing the development of the conical horn antenna in Chapter 2. Design theory is reviewed, and a horn is developed. Chapter 3 discusses the simulation and results of the conical horn antenna. Geometric parameters are varied and their effect on the reflection coefficient and directivity are explored. Chapter 4 details the design and simulation of the taper that couples the conical horn and high power microwave source. Chapter 5 investigates reflection and electric field properties of the dielectric window that separates the vacuum conditions inside the vircator and the air inside the antenna. Chapter 6 concludes the thesis and proposes possible future studies. The thesis is supplemented with a guide to the COMSOL RF Module in Appendix A, a complete set of plots of the Electric Field per $\text{Power}^{1/2}$ for all tapers explored (Chapter 4) in Appendix B, and MATLAB code used to calculate the peak Electric Field and perform a regression analysis (Chapter 5) in Appendix C.

Chapter 2

Conical Horn Antenna

The first stage of system development was to design a compact conical horn antenna that would produce the desired radiating characteristics from the high power microwave source. Design constraints require the conical horn antenna must be no larger than 6 inches (15.24 cm) in diameter, be as compact as possible, radiate the TE_{11} mode effectively, provide a directivity of approximately 10-15 dB, and transfer as much power from the source to free space as possible. This chapter describes the theory behind the development of the conical horn antenna.

Design Theory

Design of the conical horn antenna was driven by geometrical size and the directivity constraints. The design process began by consulting [4], which has an

extensive section on horn antennas. A conical horn antenna was the geometry of choice because of the cylindrical profile of the source. A cylindrical waveguide can be attached to feed the conical horn.

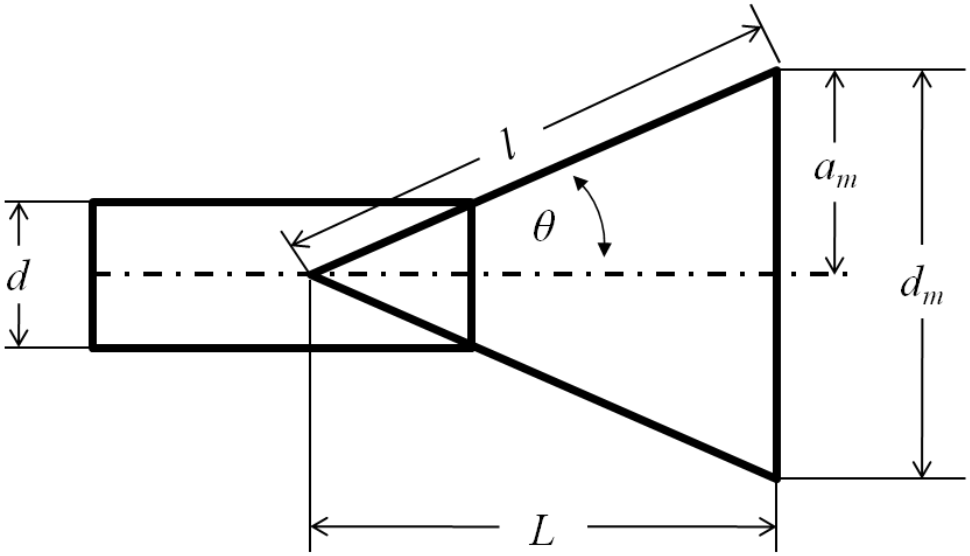

Figure 2.1: Cross section of a conical horn antenna with design parameters.

Simulations were used to tweak the device, but the baseline geometry for the conical horn was found using formulas in [4]. A basic diagram of the conical horn with important design parameters is shown in Figure 2.1. While the field analysis is complex, as shown in [28], and an important aspect of antennas, it is not the most efficient way to approach this particular antenna design. Since previous desired directivity results are known, the design of the conical horn began by utilizing these directivity results [4], [29]. The directivity of a conical horn antenna with aperture efficiency, ϵ_{ap}, which is the ratio of the maximum effective area of the antenna to its physical area, and aperture circumference, *C*, can be found using

$$D(dB) = 10\log_{10}\left[\epsilon_{ap}\frac{4\pi}{\lambda^2}\left(\pi {a_m}^2\right)\right] = 10\ \log_{10}\left(\frac{C}{\lambda}\right)^2 - L(s) \quad (2.1)$$

where a_m is the radius of the horn at the aperture, λ is the wavelength of the radiating wave and

$$L(s) = -10 \log_{10} \epsilon_{ap}. \tag{2.2}$$

In equation (2.1), the first term represents the directivity of a uniform circular aperture whereas the second term, seen in equation (2.2) and referred to as the loss figure, is a correction to account for the loss in the directivity due to the aperture efficiency. The loss figure, which was computed in decibels using [30], [31], can be found from

$$L(s) \cong (0.8 - 1.71\, s + 26.25\, s^2 - 17.79\, s^3) \tag{2.3}$$

where *s* is the maximum phase deviation, in wavelengths, and is equal to

$$s = \frac{{d_m}^2}{8\lambda l}. \tag{2.4}$$

The directivity of the conical horn will be optimal when its diameter is equal to

$$d_m = \sqrt{3l\lambda} \tag{2.5}$$

and this value corresponds to a maximum aperture phase deviation of 3/8 wavelengths and a loss figure of about 2.9 dB.

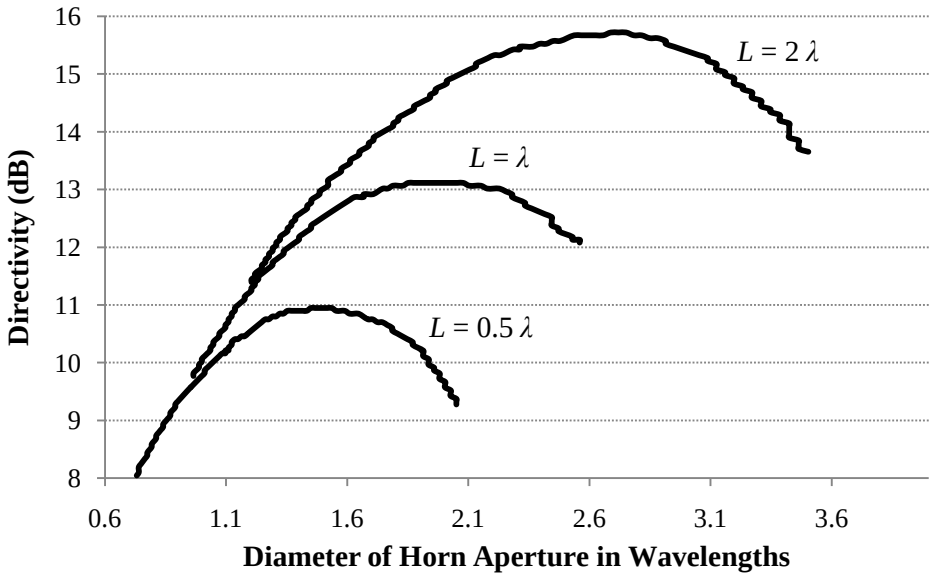

Figure 2.2: Directivity of a conical horn versus aperture diameter and for three axial horn lengths [29].

King describes the directivity of a conical horn as a function of aperture diameter, d_m, and axial length, L [29]. The relationship is shown in Figure 2.2. Since the desired device is compact, the important curves of the directivity versus diameter of horn aperture trends are those with smaller diameters. The desired radiating frequency of 4 to 6 GHz corresponds to wavelengths of 7.5 to 5 cm. With a maximum aperture diameter of 15.24 cm set by the design constraints, the radiating range corresponds to a wavelength dimension maximum of 2 to 3 λ. An important trend to take from Figure 2.2 is that the maximum directivity is set by the axial length, L, and that as the axial length increases, the maximum possible directivity increases.

The design of the conical horn began by computing the length, l, for a frequency of 4 GHz (λ = 7.5 cm) and a horn aperture diameter of 13.2 cm from equation (2.5). This value of aperture diameter was selected to ensure the device is within the design constraints, as room must be allowed for material thickness and for a reflection reducing

geometry, which is discussed later. The length, *l*, was calculated to be 10 cm. This length corresponded to an axial length, *L*, of 8.5 cm. As seen in Figure 2.2, this geometry produces a directivity of approximately 13 to 14 dB, which is too high. This geometry was a starting point for simulations, but the axial length needed to be decreased to 7.3 cm (~ 1 wavelength) in order to obtain the desired directivity across the entire spectrum which was then verified through simulation.

To improve conical horn efficiency, curved surface sections are attached outside of the aperture edges [4],[32]. A diagram of the new geometry can be seen in Figure 2.3. Adding these sections reduces diffractions at sharp edges at the end of the horn, and in turn, reduces the amount of reflection back into the horn. In [32], good results were obtained using cylindrical surfaces of $2.5\ \lambda \leq a \leq 5\ \lambda$ where a is the radius. Due to the design constraints, surfaces of this size were not plausible. In an effort to decrease the amount of reflection back into the source from the horn, curved surfaces were added at the aperture edges in a trial and error process and analyzed in simulation to generate a device with less reflection. This process and the results are discussed in the next chapter. To further decrease the amount of reflection back into the source, a curved surface is added at the horn-waveguide junction. Removing the sharp point at this junction reduces the amount of reflection back into the waveguide, and thus decreasing the reflection from the device. The choice of the radii of curvature for this tapered throat was also performed in a trial and error process and is discussed in the next chapter.

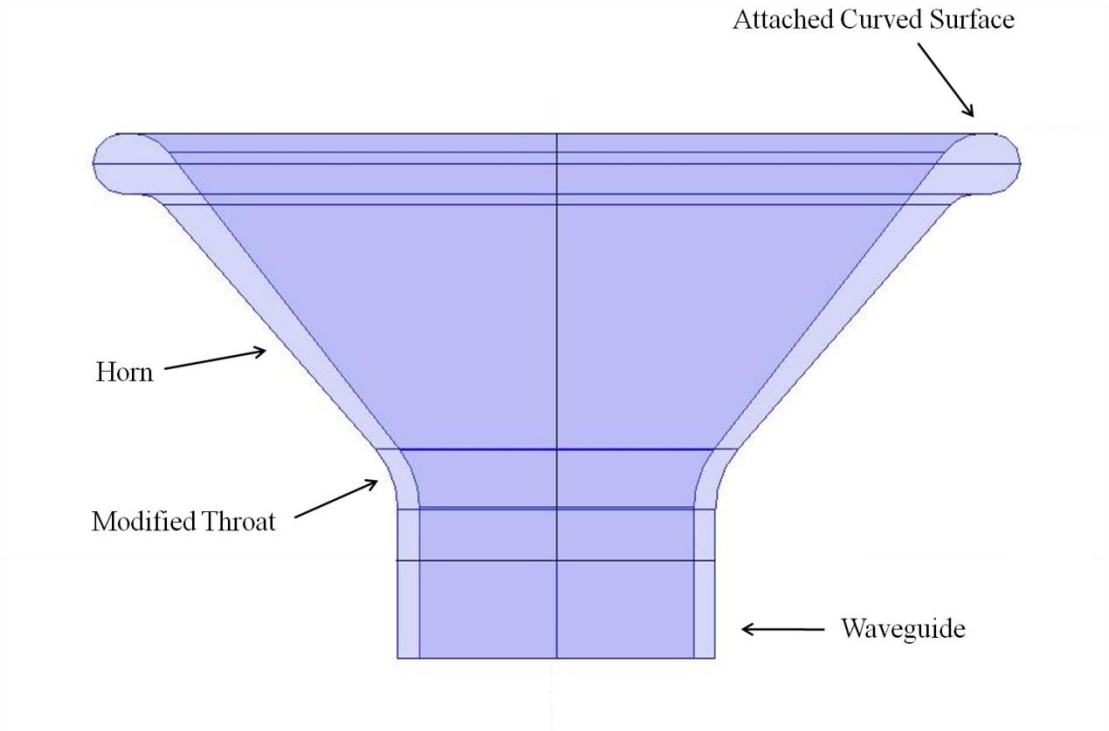

Figure 2.3: Geometry of an aperture matched horn.

The design of the waveguide feeding into the horn is also of interest. This element determines the frequencies that will propagate into the horn antenna. In [33], Balanis covers the derivation of the fields inside a circular waveguide, the phase constant, guide wavelength, guide impedance, and guide cutoff frequency. Because the system's goal is the efficient radiating of the dominant mode, TE_{11}, the field for a cylindrical waveguide will be solved for the TE mode. The TE mode is derived by letting vector potentials **A** and **F** be equal to

$$\mathbf{A} = 0 \tag{2.6}$$

$$\mathbf{F} = \hat{z}F_z(r, \Phi, z). \tag{2.7}$$

The vector potential **F** of equation (2.7) satisfies the wave equation

$$\nabla^2 F_z(r, \Phi, z) + \beta^2 F_z(r, \Phi, z) = 0 \tag{2.8}$$

which in cylindrical coordinates reduces to

$$\frac{\partial^2 F_z}{\partial r^2} + \frac{1}{r}\frac{\partial F_z}{\partial r} + \frac{1}{r^2}\frac{\partial^2 F_z}{\partial \Phi^2} + \frac{\partial^2 F_z}{\partial z^2} + \beta^2 F_z = 0. \tag{2.9}$$

Solving for F_z, the following is obtained:

$$F_z(r, \Phi, z) = [A_1 J_m(\beta_r r) + B_1 Y_m(\beta_r r)] \times [C_2 \cos(m\Phi) + D_2 \sin(m\Phi)][A_3 e^{-j\beta_z z} + B_3 e^{j\beta_z z}] \tag{2.10}$$

where

$$\beta_r{}^2 + \beta_z{}^2 = \beta^2. \tag{2.11}$$

To obtain the constants A_1, B_1, C_2, D_2, A_3, and B_3 from equation (2.10), the boundary conditions of the cylindrical waveguide are applied to the solution. At the wall of the waveguide, the tangential component of the electric field must be equal to zero, the electric and magnetic fields must be finite everywhere, and the electric and magnetic fields must repeat every 360° in the Φ direction. Because the fields must be finite everywhere, $B_1 = 0$ since $Y_m(r = 0) = \infty$. Because the fields must repeat every 360°, m = 0,1,2,3,… Assuming waves only propagate in the $+z$ direction, and applying the boundary conditions from above, equation (2.10) reduces to

$$F_z{}^+ = A_{mn} J_m(\beta_r r)[C_2 \cos(m\Phi) + D_2 \sin(m\Phi)] e^{-j\beta_z z}. \tag{2.12}$$

The electric field can be found from the vector potential **F** through the following expressions

$$E_r{}^+ = -\frac{1}{\varepsilon r}\frac{\partial F_z{}^+}{\partial \Phi} \tag{2.13}$$

$$E_{\Phi}{}^{+} = \frac{1}{\varepsilon}\frac{\partial F_z{}^{+}}{\partial r} \tag{2.14}$$

and are equal to the following:

$$E_r{}^{+} = -A_{mn}\frac{m}{\varepsilon r}J_m(\beta_r r)[-C_2\sin(m\Phi) + D_2\cos(m\Phi)]e^{-j\beta_z z} \tag{2.15}$$

$$E_{\Phi}{}^{+} = A_{mn}\frac{\beta_r}{\varepsilon}J_m{}'(\beta_r r)[C_2\sin(m\Phi) + D_2\cos(m\Phi)]e^{-j\beta_z z} \tag{2.16}$$

where $' = \frac{\partial}{\partial(\beta_r r)}$.

Taking equation (2.16) and applying the boundary condition that the electric field at the wall of the waveguide is equal to zero results in

$$E_{\Phi}{}^{+}(r = a, \Phi, z) = A_{mn}\frac{\beta_r}{\varepsilon}J_m{}'(\beta_r r)[C_2\sin(m\Phi) + D_2\cos(m\Phi)]e^{-j\beta_z z} = 0. \tag{2.17}$$

Equation (2.17) is only satisfied when

$$J_m{}'(\beta_r r) = 0 \Rightarrow \beta_r = \frac{\chi_{mn}{}'}{a}. \tag{2.18}$$

In equation (2.18), χ'_{mn} is the *n*th zero (*n* = 1,2,3…) of the derivative of the Bessel function J_m of the first kind of order *m* (*m* = 0,1,2,3,…). A list of the zeroes χ'_{mn} can be found in [33] in Table 9-1. The dominant mode of the waveguide is found through the zero with the lowest magnitude. The smallest value for the TE mode is χ'_{mn} = 1.8412 which corresponds to *m*=1, *n*=1. This verifies that the dominant TE mode for a cylindrical waveguide is TE_{11}. As verified later, the TE_{11} is the dominant mode for the waveguide as it has the lowest cutoff frequency of all modes.

To determine the cutoff frequency for a given mode in a waveguide, the phase constant in the z direction is computed from equation (2.11).

$$(\beta_z)_{mn} = \begin{cases} \sqrt{\beta^2 - {\beta_r}^2} = \sqrt{\beta^2 - \left(\frac{\chi_{mn}{}'}{a}\right)^2} \text{ when } \beta > \beta_r = \frac{\chi_{mn}{}'}{a} \\ 0 \text{ when } \beta = \beta_r = \frac{\chi_{mn}{}'}{a} \\ -j\sqrt{{\beta_r}^2 - \beta^2} = -j\sqrt{\left(\frac{\chi_{mn}{}'}{a}\right)^2 - \beta^2} \text{ when } \beta < \beta_r = \frac{\chi_{mn}{}'}{a} \end{cases} \quad (2.19)$$

The cutoff of the waveguide is defined when $(\beta_z)_{mn}$ is equal to zero, and therefore

$$\beta_c = \beta_r = \frac{\chi_{mn}{}'}{a} = \omega_c\sqrt{\mu\varepsilon} = 2\pi f_c\sqrt{\mu\varepsilon}. \quad (2.20)$$

Solving for f_c yields the following:

$$(f_c)_{mn} = \frac{\chi_{mn}{}'}{2\pi a\sqrt{\mu\varepsilon}}. \quad (2.21)$$

Equations (2.20) and (2.21) can be used to rewrite equation (2.19) as

$$(\beta_z)_{mn} = \begin{cases} \sqrt{\beta^2 - {\beta_r}^2} = \beta\sqrt{1 - \left(\frac{f_c}{f}\right)^2} \text{ when } f > f_c \\ 0 \text{ when } f = f_c \\ -j\sqrt{{\beta_r}^2 - \beta^2} = -j\beta\sqrt{\left(\frac{f_c}{f}\right)^2 - 1} \text{ when } f < f_c. \end{cases} \quad (2.22)$$

The impedance of a TE mode is defined as

$$Z_m{}^+ = \frac{\mu\omega}{(\beta_z)_{mn}}. \quad (2.23)$$

Using equation (2.23), the waveguide impedance for a particular mode is found to be dependent upon the propagating frequency and the cutoff frequency, which is found by substituting equation (2.22) into (2.23).

$$Z_{mn}{}^{+} = \begin{cases} \dfrac{\mu\omega}{\beta\sqrt{1-\left(\frac{f_c}{f}\right)^2}} = \dfrac{\eta}{\sqrt{1-\left(\frac{f_c}{f}\right)^2}} & \text{when } f > f_c \\ \dfrac{\mu\omega}{0} = \infty \quad \text{when } f = f_c \\ \dfrac{\mu\omega}{-j\beta\sqrt{\left(\frac{f_c}{f}\right)^2-1}} = \dfrac{j\eta}{\sqrt{\left(\frac{f_c}{f}\right)^2-1}} & \text{when } f < f_c \end{cases} \tag{2.24}$$

Equation (2.24) reveals some important properties regarding waveguides. Above the cutoff frequency, the impedance of the waveguide is real and finite. The impedance close to cutoff is greater than that of the intrinsic impedance, and as the frequency increases to infinity, the impedance approaches that of the intrinsic impedance. At the cutoff frequency, the impedance is infinite, or an open circuit. Below cutoff, the impedance is imaginary and inductive, which indicates that the waveguide will behave as an inductive storage element in the TE mode.

A very similar process is done to solve the system for TM waves, which begins by equating the vector **F** to zero, and setting the vector potential **A** to $\hat{z}A_z(r, \Phi, z)$. The derivation can be found in [33], and the results are summarized here. As a note, the zeros χ_{mn} can be found in Table 9-2 of [33].

$$(f_c)_{mn} = \frac{\chi_{mn}}{2\pi a\sqrt{\mu\varepsilon}} \tag{2.25}$$

$$(\beta_z)_{mn} = \begin{cases} \sqrt{\beta^2 - {\beta_r}^2} = \beta\sqrt{1 - \left(\frac{f_c}{f}\right)^2} \text{ when } f > f_c \\ 0 \text{ when } f = f_c \\ -j\sqrt{{\beta_r}^2 - \beta^2} = -j\beta\sqrt{\left(\frac{f_c}{f}\right)^2 - 1} \text{ when } f < f_c \end{cases} \quad (2.26)$$

$$Z_{mn}{}^{+} = \frac{(\beta_z)_{mn}}{\omega\varepsilon} = \begin{cases} \frac{\beta\sqrt{1-\left(\frac{f_c}{f}\right)^2}}{\omega\varepsilon} = \eta\sqrt{1 - \left(\frac{f_c}{f}\right)^2} \text{ when } f > f_c \\ \frac{0}{\omega\varepsilon} = 0 \text{ when } f = f_c \\ \frac{-j\beta\sqrt{\left(\frac{f_c}{f}\right)^2-1}}{\omega\varepsilon} = -j\eta\sqrt{\left(\frac{f_c}{f}\right)^2 - 1} \text{ when } f < f_c \end{cases} \quad (2.27)$$

It is important to note that for the TM mode, that above the cutoff frequency the impedance is real and smaller than the intrinsic impedance. As the propagating frequency approaches infinity, the impedance will approach the intrinsic impedance. At cutoff, the impedance is zero, or a short circuit. Below cutoff, the waveguide will act as a capacitive energy storage element.

Using equations (2.21) and (2.25), the cutoff frequencies for TE_{mn} and TM_{mn} modes can be calculated and ranked from lowest order mode upward. The cutoff frequencies were calculated for the first nine modes for various radii between 2 and 4.5 cm and are shown in Table 2.1. It can be seen that as the radius decreases, the cutoff frequency increases. The choice of radius will have an effect on the properties of the conical horn which is verified through simulation. It is also of importance to ensure that only the desired mode will be able to propagate in the waveguide. For example, for a desired radiating range of 4 to 6 GHz, a waveguide with a radius of 3 cm will allow TE_{11} through TE_{31} to propagate through the system, but for a waveguide with radius 2.25 cm,

only TE_{11} and TM_{01} are allowed to propagate. As a starting point for simulation, a waveguide was connected to the conical horn that had a radius of 2.25 cm because it allowed only two modes to propagate in the radiating range. The selection of the final value of the radius and the justification behind it are explained in the results section of Chapter 3.

Table 2.1: List of cutoff frequencies (GHz) for the lowest 9 modes for a cylindrical waveguide with radius *a*.

Radius (cm)	4.5	4	3.5	3	2.5	2.25	2
Mode	**Frequency (GHz)**						
TE11	1.95	2.20	2.51	2.93	3.51	3.91	4.39
TM01	2.55	2.87	3.28	3.83	4.59	5.10	5.74
TE21	3.24	3.64	4.16	4.86	5.83	6.48	7.29
TM11	4.06	4.57	5.22	6.10	7.31	8.13	9.14
TE01	4.06	4.57	5.22	6.10	7.31	8.13	9.14
TE31	4.46	5.01	5.73	6.68	8.02	8.91	10.03
TM21	5.45	6.13	7.00	8.17	9.80	10.89	12.25
TE41	5.64	6.34	7.25	8.46	10.15	11.28	12.69
TE12	5.65	6.36	7.27	8.48	10.18	11.31	12.72

By combining the design principles from a conical horn antenna and a cylindrical waveguide, a radiating system was designed. This design served as the starting point for simulations, and was tweaked in order to produce a final design. The conical horn with feeding waveguide is shown in Figure 2.4 and values for the parameters going into the first simulation are in Table 2.2.

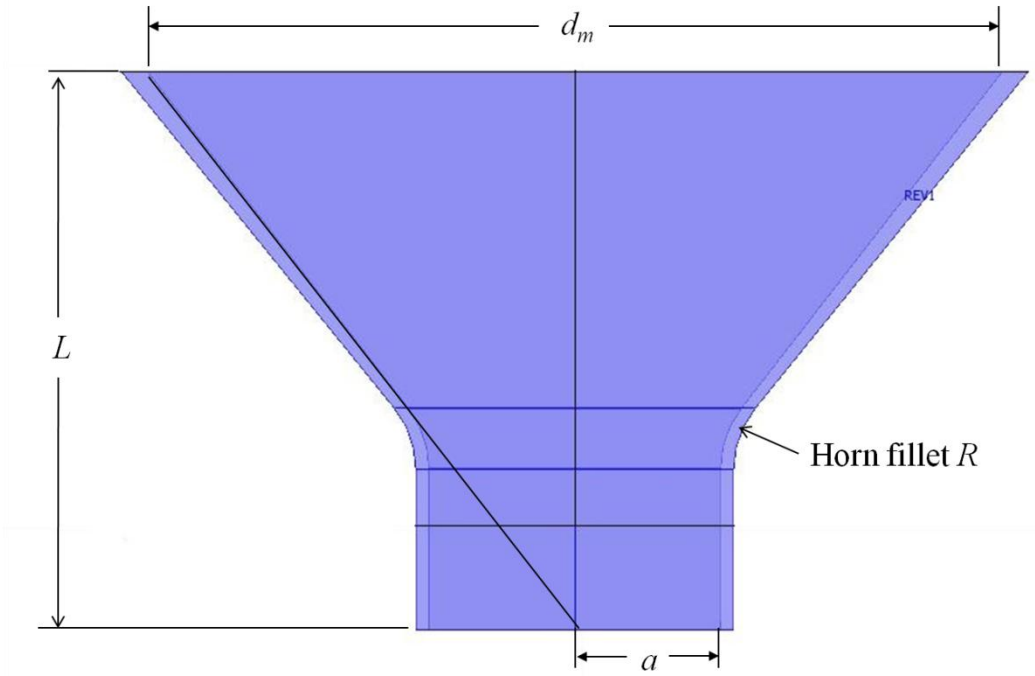

Figure 2.4: Conical horn antenna and feeding waveguide with labeled design parameters.

Table 2.2: Values for design parameters shown in Figure 2.4.

Parameter	Value
d_m	13.2 cm
L	8.5 cm
a	2.25 cm
R	1.5 cm

Chapter 3

Simulation Concepts and Conical Horn Simulation

After the conical horn was designed based on theoretical concepts, the next step was to simulate the design to verify the desired characteristics. If either the radiating or reflection characteristics are not desirable, the design parameters are fine tuned such that they are met. This chapter begins by first discussing the concepts of 3D electromagnetic simulation, and then proceeds with the analysis of the simulation results from the designed conical horn.

3D Electromagnetic Simulation Concepts

Before specific simulation setups are described, it is of importance to discuss concepts and tools pertaining to electromagnetic simulations. All information is taken

from [34] unless noted otherwise. In simulation, a given geometry is divided into subdomains and boundaries, and it is essential to define properties for each in simulation space. The properties of the subdomain correlate to the material properties and include the relative permittivity, conductivity, and relative permeability. For a given subdomain, the governing equation when solving for the electric field is a form of the wave equation, and is shown in equation (3.1).

$$\nabla \times (\mu_r{}^{-1} \nabla \times \mathbf{E}) - k_0{}^2 \left(\varepsilon_r - \frac{j\sigma}{\omega \varepsilon_0}\right) \mathbf{E} = 0 \tag{3.1}$$

where μ_r is the relative permeability, k_0 is the wave number, ε_r is the relative permittivity, σ is the material conductivity, ω is the angular wave frequency, and ε_0 is the permittivity of free space.

It is also important to note how the electric and magnetic fields behave at the boundary of two materials. In the general form, the boundary conditions are described in equations (3.2) and (3.3).

$$-\hat{n} \times (\mathbf{E}_2 - \mathbf{E}_1) = \mathbf{M_s} = 0 \tag{3.2}$$

$$\hat{n} \times (\mathbf{H}_2 - \mathbf{H}_1) = \mathbf{J_s} \tag{3.3}$$

where $\mathbf{E}_{1,2}$ and $\mathbf{H}_{1,2}$ represent the electric and magnetic field on either side of the boundary, and $\mathbf{J}_s$ and $\mathbf{M}_s$ are the electric and magnetic current densities. These boundary conditions can be simplified dependent on the type of boundary desired. The following boundary conditions and their simplifications were used in the modeling of the radiating system. For a perfect electric conductor, which is used to simulate metallic boundaries, the boundary condition simplifies to equation (3.4).

$$\hat{n} \times \mathbf{E} = 0 \tag{3.4}$$

As a result of drawing geometries, many boundaries exist that are not necessarily boundaries from an electromagnetic perspective. These boundaries are said to be continuous, and the general form simplifies to equations (3.5) and (3.6) for this boundary type.

$$\hat{n} \times (\mathbf{E}_1 - \mathbf{E}_2) = 0 \tag{3.5}$$

$$\hat{n} \times (\mathbf{H}_1 - \mathbf{H}_2) = 0 \tag{3.6}$$

On an external boundary, waves can be excited on a boundary knowing the properties of an incident electric field $\mathbf{E}_0$. Based on the geometry properties, $\mathbf{E}_0$ replaces either $\mathbf{E}_1$ or $\mathbf{E}_2$ in equation (3.2).

The simulation space has many equations correlating to subdomains and boundary conditions that need to be solved. In this thesis, the finite element method is used to solve these equations. This method is a numerical technique for obtaining an approximate solution to the electromagnetic problem by converting the governing differential equations into a set of linear algebraic equations [25]. The domain is discretized or meshed into many small elements, referred to as finite elements. The equations obtained for each element are assembled together with adjoining elements to form the global finite element equations for the entire domain [26],[27]. An equation solver is then used to solve the system of equations to arrive at an approximate solution of the problem.

To solve large 3D electromagnetic problems, iterative solvers are popular because direct linear solvers require too much memory and excessive computation times in large

domains. Simulation time is also dependent on the mesh. As the number of mesh elements increases, a larger set of algebraic equations exists, and therefore higher computation times are required to solve the equation set. A lesser number of elements will decrease simulation time at the cost of simulation accuracy. Converging to a solution depends on the stability, or Nyquist, criterion related to the size of the mesh element. Therefore it is imperative to ensure a proper mesh is created. For 3D electromagnetic wave problems, the Nyquist criterion is such that there must be at least two mesh elements per wavelength everywhere in the geometry. In an iterative solver, due to the fact that a direct solver is used to solve subdomain and boundary equations in the coarsest mesh, it is desirable to be as close to the Nyquist criterion as possible in order to reduce memory usage and decrease computation time.

The iterative solver that works well for 3D electromagnetic wave problems is the generalized minimum residual method or GMRES. GMRES solves the linear system of the form $A*x = b$ by approximating the exact solution by a vector in Krylov space that minimizes the norm of the residual. The specifics of the GMRES algorithm are presented in work by Saab and Schultz in [35]. At a high level, the GMRES method completes one step of the Arnoldi method (finding eigenvalues), then finds the eigenvalue that minimizes the norm of the residual, approximates the value of the vector x, and then repeats if the residual is not yet small enough. A preconditioner is often added to the GMRES method to achieve convergence faster. The preconditioner is a matrix M such that $M^{-1}* A* x = M^{-1}*b$. The system converges faster due to the fact that the result of $M^{-1}* A$ is closer to the identity matrix. For many 3D electromagnetic problems, the

geometric multigrid preconditioner is the best selection. Convergence to a solution is found using the following convergence criterion shown in equation (3.7).

$$\rho|M^{-1}\,(b - Ax)| < tol\ \cdot |M^{-1}b| \tag{3.7}$$

where ρ is the factor in error estimate, M is the preconditioned matrix, and *tol* is the relative tolerance. The solver will iterate until the condition in equation (3.7) is met, or until the maximum number of allowed iterations is achieved.

Two important quantities solved for in 3D antenna problems are scattering parameters (S parameters) and far field radiation characteristics. The S parameters are complex, frequency dependent matrices that describe the transmission and reflection of electromagnetic energy at various ports. The S parameter matrix is as follows for an *n* port device

$$S = \begin{bmatrix} S_{11} & \cdots & S_{1n} \\ \vdots & \ddots & \vdots \\ S_{n1} & \cdots & S_{nn} \end{bmatrix}. \tag{3.8}$$

The S parameter matrix is utilized in the following relationship

$$\begin{bmatrix} b_1 \\ b_2 \\ \vdots \\ b_n \end{bmatrix} = [S] \begin{bmatrix} a_1 \\ a_2 \\ \vdots \\ a_n \end{bmatrix} \tag{3.9}$$

where the vector **a** is the incident wave and vector **b** is the reflected wave. From equations (3.8) and (3.9), it is shown that S_{11} is the forward reflection coefficient, S_{21} is the forward transmission coefficient from port 1 to port 2, S_{12} is the transmission from port 2 to port 1, etc. The S parameters can be calculated from known voltages, electric

fields, or power levels. For high frequency problems where voltages are not a well defined entry into the simulation, the S parameters are calculated using the electric field and/or the power flow. If the electric field pattern, $\mathbf{E}_n$, is known on a port, and assuming that the field is normalized with respect to the integral of the power flow across each port cross section, the S parameters can be calculated by equations (3.10) and (3.11).

$$S_{nn} = \frac{\int_{port\ n}((\mathbf{E}_c - \mathbf{E}_n)\cdot\mathbf{E}_n{}^*)dA_n}{\int_{port\ n}(\mathbf{E}_n\cdot\mathbf{E}_n{}^*)dA_n} \tag{3.10}$$

$$S_{mn} = \frac{\int_{port\ m}(\mathbf{E}_c\cdot\mathbf{E}_m{}^*)dA_m}{\int_{port\ m}(\mathbf{E}_m\cdot\mathbf{E}_m{}^*)dA_m} \tag{3.11}$$

where $\mathbf{E}_c$ is the computed electric field on the port, which consists of the excitation electric field and the reflected electric field, and *m* is any port that is not the excitation port *n*. If the magnitude of the S parameters is only necessary, they can be calculated using the power flow. This is advantageous because the electric field pattern $\mathbf{E}_n$ does not need to be known. The definition of the S parameters in terms of power flow is found in equation (3.12).

$$S_{mn} = \sqrt{\frac{\text{Power reflected from port } m}{\text{Power incident on port } n}} \tag{3.12}$$

The power flow is given by the time average Poynting vector, $\mathbf{S}_{av}$, and the power flow out of a port is given by the normal component of the Poynting vector, as show in equation (3.13).

$$\mathbf{n}\cdot\mathbf{S}_{\mathrm{av}} = \mathbf{n}\cdot\frac{1}{2}\,\mathrm{Re}(\mathbf{E}\times\mathbf{H}^*) \tag{3.13}$$

If the wave mode is known, the power flow can be expressed in terms of the electric field and the impedance. These relationships are shown in equations (3.14) to (3.16).

$$\mathbf{n} \cdot \mathbf{S}_{\text{av}} = \frac{1}{2\, Z_{TE}} |\mathbf{E}|^2 \tag{3.14}$$

$$\mathbf{n} \cdot \mathbf{S}_{\text{av}} = \frac{1}{2\, Z_{TM}} |\mathbf{n} \times \mathbf{E}|^2 \tag{3.15}$$

$$\mathbf{n} \cdot \mathbf{S}_{\text{av}} = \frac{1}{2\, Z_{TEM}} |\mathbf{E}|^2 \tag{3.16}$$

where Z_{TE} is equal to $\frac{\omega\mu}{\beta}$, Z_{TM} is equal to $\frac{\beta}{\omega\varepsilon}$, and Z_{TEM} is equal to $\sqrt{\frac{\mu}{\varepsilon}}$, and β is the propagation constant, μ is the permeability, ω is the angular frequency, and ε is the permittivity.

Because it is impossible to simulate all of free space to find the far field, there needs to be a method that will model how all of free space behaves. This behavior is represented by a perfectly matched layer (PML). The PML is a subdomain region that absorbs waves in the forward propagating direction and does not reflect any waves back into the simulation domain. The basic concept of a PML is to have a coordinate transformation in which coordinates are mapped to complex numbers and thus replacing oscillating waves by exponentially decaying waves. A common implementation for an electromagnetic PML that absorbs waves in the direction *t* is found in equation (3.17).

$$t' = t\frac{\lambda}{\delta t}(1 - i) \tag{3.17}$$

where t is the coordinate, and δt is the width representing the infinite element region.

The far field is also of interest because it defines how the antenna radiation pattern will behave at large distances from the radiating source. The far field is defined as the region of space where the electric and magnetic field are orthogonal to each other and form TEM waves. The fields radiated by an antenna are spherical waves close to the source. The amplitude variation due to the radius r in each component (r,θ,φ) are of the form $1/r^n$. By neglecting higher order terms of $1/r^n$, the r variations are separable from the θ and φ terms, and can be seen that the radiated electric and magnetic fields only have θ and φ components in the far field region. A full derivation of this fact is found in [4].

As discussed, if a domain was created that contained enough space to measure the far field, the simulation would take excessive and often an impractical amount of time to simulate. Fortunately, there is a method that allows far field approximation from knowledge of the near field. For a spherical wave, the far field is calculated from the near field on the boundary at the beginning of the PML region from the Stratton-Chu formula, which is found in equation (3.18).

$$\mathbf{E}_p = \frac{jk_0}{4\pi}\mathbf{r}_0 \times \int [\mathbf{n} \times \mathbf{E} - \eta_0 \mathbf{r}_0 \times (\mathbf{n} \times \mathbf{H})] \exp(jk_0 \boldsymbol{r} \cdot \boldsymbol{r}_0)\, dS \qquad (3.18)$$

where **E** and **H** are the fields at the aperture, the surface S encloses the antenna, $\mathbf{r}_0$ is the unit vector pointing from the origin to the point p, **n** is the unit normal vector to the surface S, η_0 is the free space wave impedance, k_0 is the free space wave number, **r** is the radius vector of the surface S, and $\mathbf{E}_p$ is the calculated far field at point p. Note that the far field radiation pattern is with respect to power. Because the far field is computed in free space, $\mathbf{H} = \frac{\mathbf{r}_0 \times \mathbf{E}_p}{\eta_0}$, and thus the Poynting vector is proportional to the square of the magnitude of the electric field, $\mathbf{E}_p$.

Simulation Setup – Modeling the Antenna

The first simulations examined the behavior of the proposed design from theory. A cross section of the horn is shown in Figure 3.1. The thickness of the horn walls were designed to be greater than the skin depth for the construction material. The thickness of the material will be dependent upon other characteristics that are not associated with electromagnetic properties. In the 3D geometry, shown in Figure 3.2, a sphere of radius 25 cm was drawn around the horn to model the free space outside an antenna. This size was selected so that near field characteristics could be examined, as well as to constrict the model size so simulation solution times were acceptable. A sphere of radius 30 cm was then drawn in order to create a region that acts as an absorbing boundary for the radiated waves from the antenna.

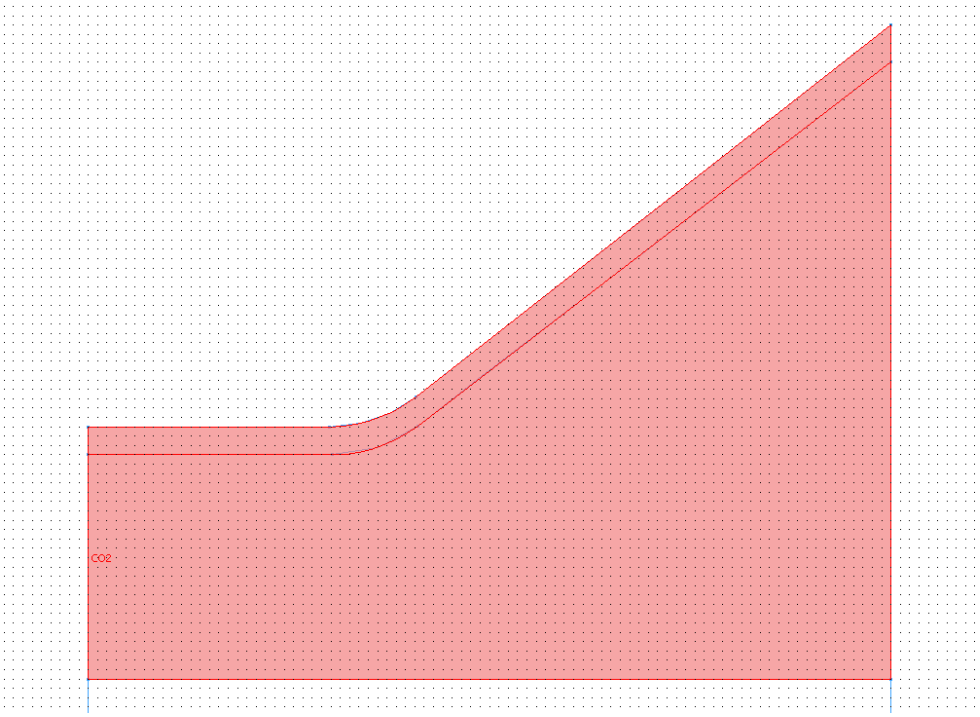

Figure 3.1: Cross section of the simulation model for the antenna radiating into free space.

After the system was drawn, the properties of solid objects were set. The conical horn antenna material was set to copper, which has an electrical conductivity of 5.998×10^7 S/m. The space inside the horn was set to the material properties of air, as well as the area outside of the horn in the forward direction (+z). The PML region was set to have the material properties of free space and to absorb spherical waves.

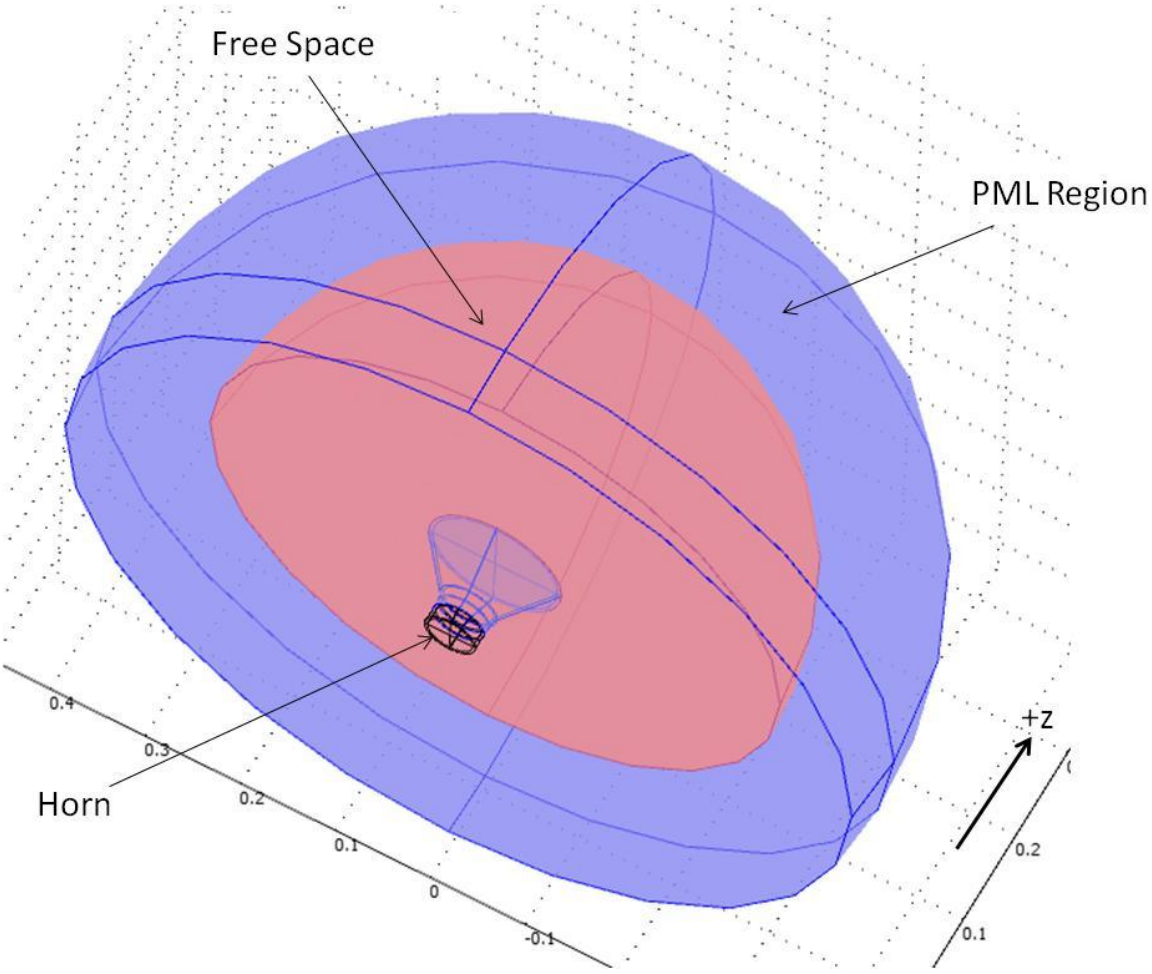

Figure 3.2: 3D geometry of the antenna model.

Once the subdomain settings were set for the model, the boundary conditions are defined. All external boundaries of the PML region were set to a scattering boundary

condition. With this setting, any wave that is not completely absorbed by the PML will be scattered in all directions. The boundaries inside the horn were set to continuity, as the subdomain settings will take care of the conductor properties at the boundary. In order to do far field analysis, a variable Efar was added to contain the results from the Stratton-Chu formula. At the input of the horn, the port boundary condition was selected. The wave was excited in the TE_{11} mode at this boundary, with an input power of 1 W, and phase of 0 degrees. These values were selected because only the radiation and reflection properties are important at this stage.

Simulations are parameterized to analyze 40 frequency samples between 3.95 GHz and 6 GHz. The lowest frequency of a particular simulation is set to be above the cutoff frequency for the feeding waveguide. The linear system solver is set to GMRES, and the preconditioner to achieve faster convergence is set to geometric multigrid (see 3D Simulation Concepts). For the solver settings, the relative tolerance is set to $1x10^{-6}$, the factor in error estimate to 400, the maximum number or iteration before restart to 8000, the number of iterations before restart to 100, and preconditioning set to right. All of the preconditioner settings are left at the defaults for geometric multigrid. Before solving, the system was meshed using the extra fine predefined mesh size. With the maximum expected free space wavelength of 5 cm, the maximum element size was set to 2.5 cm in order to meet the Nyquist criterion.

After the initial simulation was performed, it was observed that the reflection characteristics of the horn were not desirable across the entire frequency spectrum. An effort was put forth to examine how to improve the reflection coefficient, S_{11}, across the spectrum. First, an analysis was performed on how the feeding waveguide radius

affected the reflection of the horn antenna. Simulations were then run with the same setup as the initial simulation, but the waveguide radius was varied between 2.3 cm and 3.1 cm. The fillet radius, R, shown in Figure 2.4, was then varied between 0.5 and 2 cm to analyze its effect on the reflection coefficient.

Once an acceptable reflection response was found, the effect of adding surfaces to the aperture of the horn and its relation to the reflection coefficient was investigated. This was performed in a trial and error process because the necessary size of a rounded surface would exceed the size constraints [32]. First, a flat plane was added from the aperture to the maximum design constraint. Afterwards, curved surfaces were examined by drawing 2^{nd} degree Bezier curves. An example Bezier and flat plane curve is shown in Figure 3.3. The same boundary and subdomain settings from previous simulations were used. Six simulations with differing Bezier curves were run to determine how much the reflection coefficient could be improved.

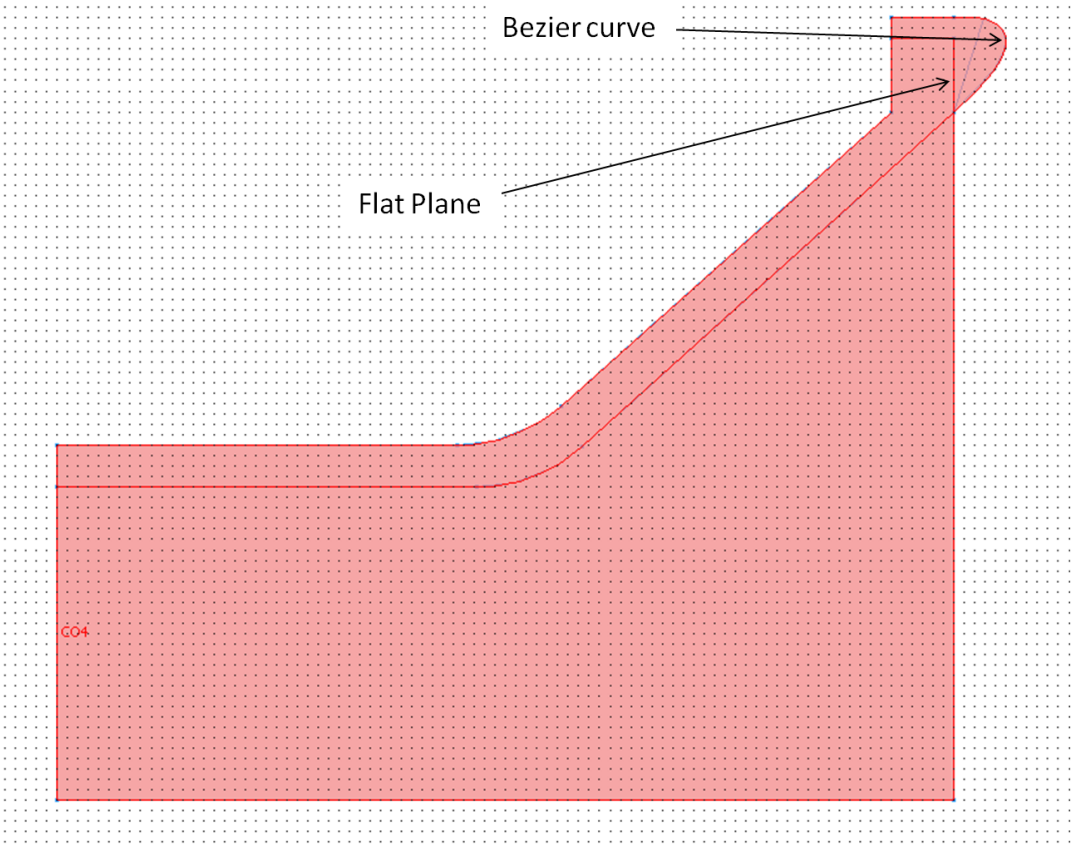

Figure 3.3: 2D workplane of the conical horn antenna with added Bezier curve and flat plane.

Once the reflection characteristics of the device were acceptable, the far field was analyzed. It was found that the horn length *L* was too large and created a directivity that is greater than desired. The device was tweaked to a desired directivity by decreasing the length *L* in small increments until it was met. After a final design was found that effectively radiates the TE_{11} mode in the 4 to 6 GHz range, an analysis was performed to ensure this would be compatible with the source.

Simulation Results

The original design was solved in COMSOL Multiphysics for frequencies between 3.95 and 6 GHz. This design had the parameters shown in Table 2.2. The lower end of the frequency spectrum is slightly above the cutoff frequency for the feeding waveguide. The reflection coefficient was analyzed for the conical horn in order to determine how much power would be transferred from the source to free space. It was found that the reflection characteristics were not desirable for the frequency spectrum, and results from the 5.5 to 6 GHz range did not converge. The reflection coefficient versus frequency can be seen in Figure 3.4.

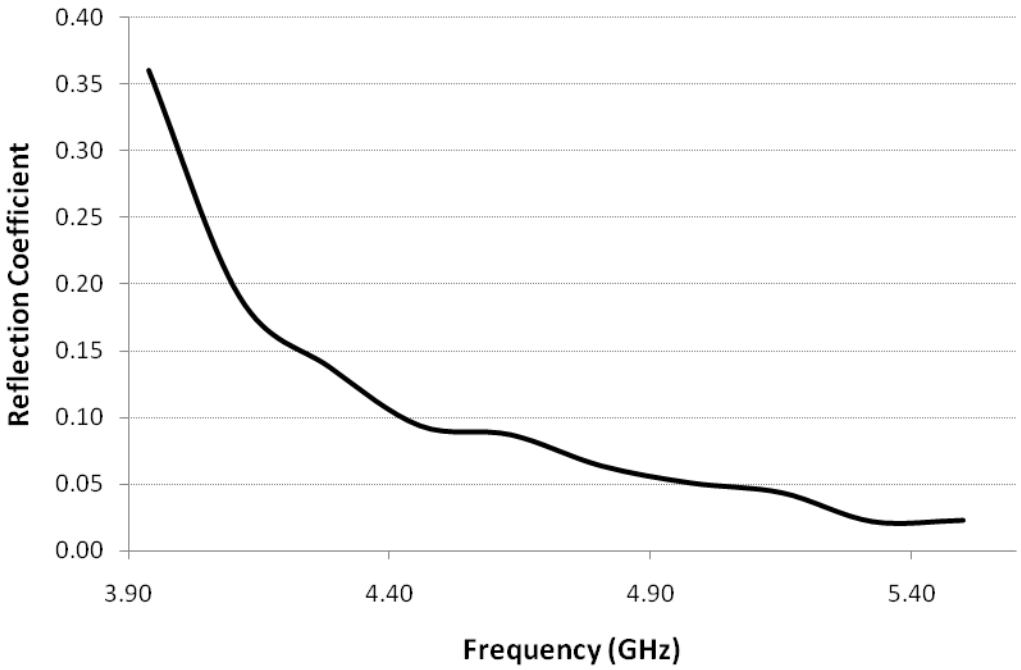

Figure 3.4: Reflection coefficient versus frequency for the original design from the design theory section.

Waveguide Radius

In an attempt to lower the reflection coefficient for the device, the effect of the feeding waveguide radius upon the S_{11} parameter was examined. The radius was varied for values ranging from 2.3 to 3.1 cm. The reflection coefficient versus frequency plots for the various radii are shown in Figure 3.5. The trend from Figure 3.5 shows that as the feeding waveguide radius increases, the characteristic curve of the S_{11} parameter shifts to lower frequencies. From Figure 3.5, it was determined that a feeding waveguide radius of 3 cm would be most desirable to carry the HPM to the antenna. The 3 cm trend line allows for a reduction of the reflection coefficient in the 4 to 6 GHz range, but also in the lower ranges. According to [24], the source has frequency components 2 to 4 GHz range, but they are not at very high power levels. Since the overarching goal of the project is to radiate as much power as possible, it is reasonable to select a feeding guide of 3 cm to couple some of the lower level powers in the sub 4 GHz region.

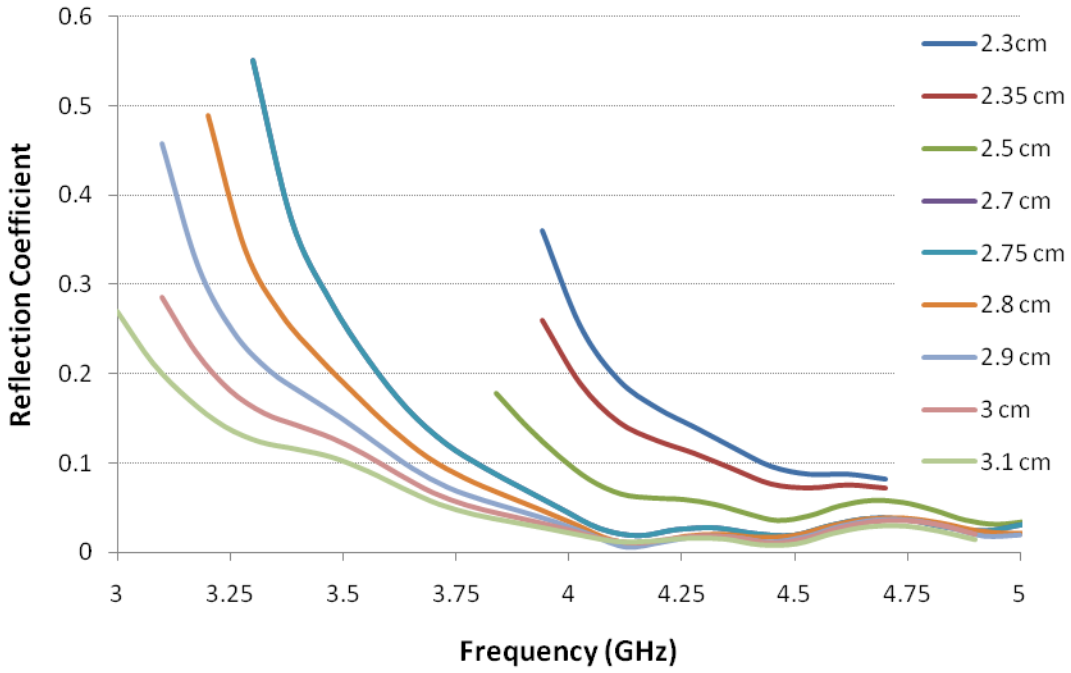

Figure 3.5: Reflection coefficient versus frequency for a conical horn antenna with various feeding waveguide radii.

Fillet Radius

The effect of the curvature connecting the feeding waveguide and the conical horn was examined next. The fillet radius *R*, shown in Figure 2.4, was varied for four different values ranging from 0.5 cm to 2 cm for a feeding waveguide radius of 3 cm. The results of this study are shown in Figure 3.6. It is shown that the fillet radius is not a crucial element to this antenna horn design, as the reflection coefficient characteristics are similar for each curvature. For that reason, the choice of this parameter should be left to manufacturability constraints. The tolerance for this component can be set much higher than other parameters. The choice of this value should be selected such that minimizes device cost as much as possible.

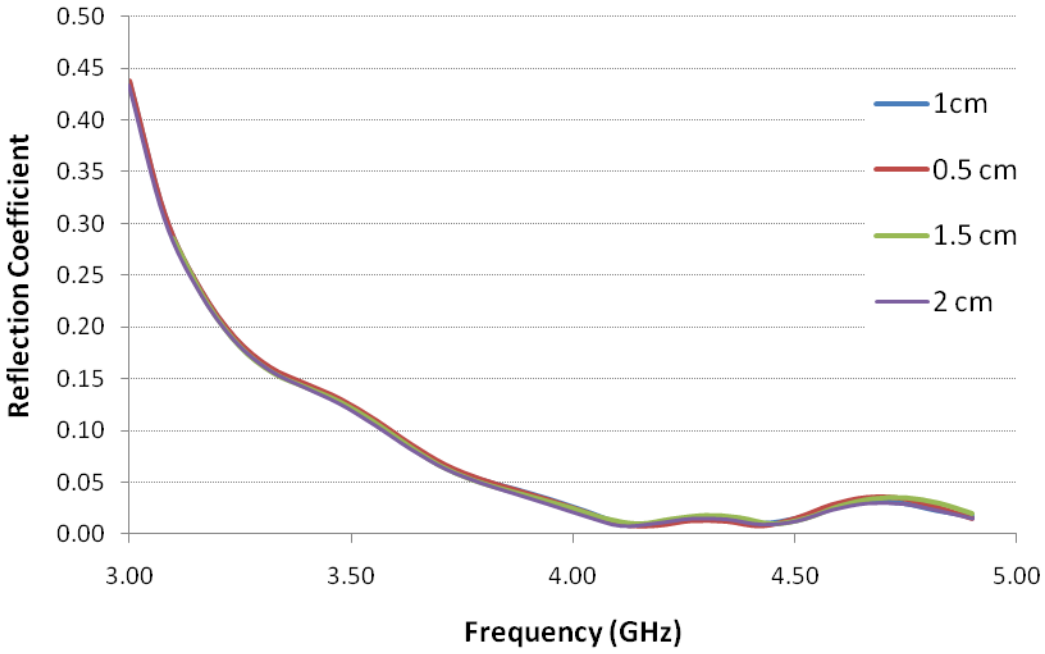

Figure 3.6: Reflection Coefficient versus frequency for four systems with varying fillet radius *R*.

Horn Aperture Geometry

Previous work has shown that adding curvature to the aperture of the conical horn antenna will reduce reflections [4],[32]. For that reason, different aperture geometries were simulated at the output of the conical horn. The first aperture geometry examined added a flat plane from the end of the antenna to the maximum antenna size. The geometry is shown in Figure 3.7. This geometry was examined for the original horn design (feed of 2.25 cm) as well as the 3 cm feed design. The results of the reflection coefficient across the frequency spectrum are shown in Figure 3.8. For the 2.25 cm feed horn, the addition of the plane reduced the reflection coefficient in the frequency range of 4 to 5 GHz, but not enough to warrant using this feed radius for the design. For the 3 cm feed, the effect of this aperture was not as noticeable, but did provide a lower magnitude

of the reflection coefficient across the 4 to 6 GHz range. Therefore, a feed waveguide radius of 3 cm is further proved to be the best choice.

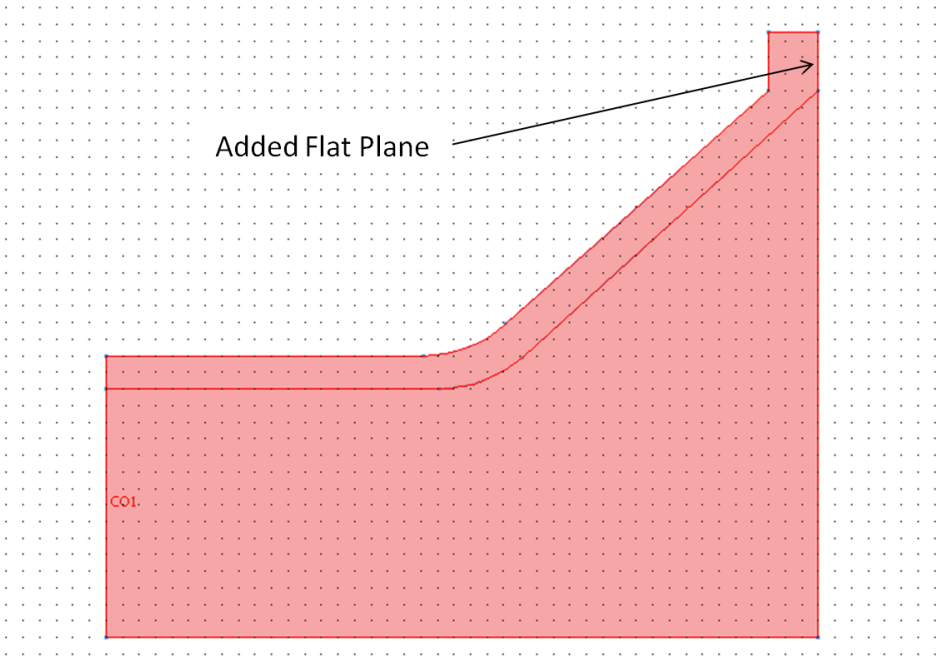

Figure 3.7: 2D view of the conical horn with an added flat plane to the aperture of the conical horn.

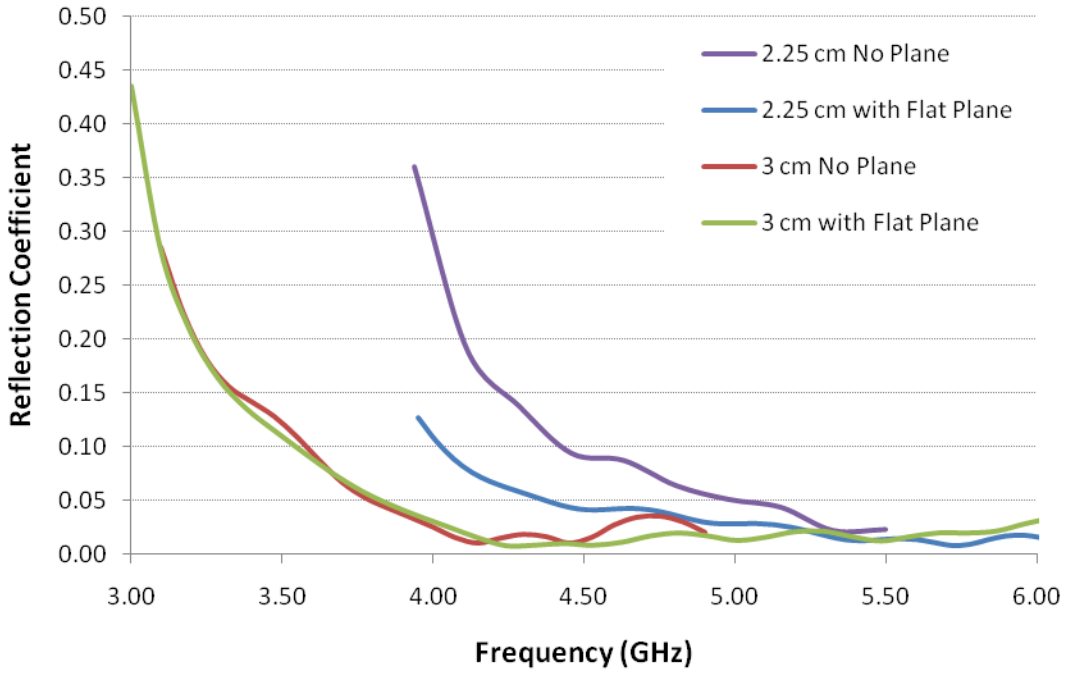

Figure 3.8: Reflection coefficient versus frequency for a flat plane added at the aperture for conical horns with a feeding waveguide radius of 2.25 cm and 3 cm.

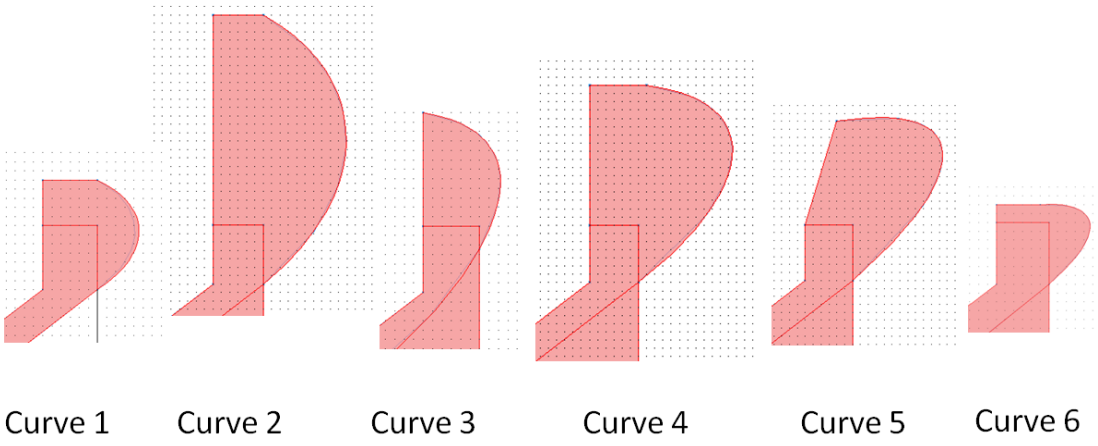

Figure 3.9: Six curves tested on the aperture of the antenna.

After the flat plane aperture was investigated, six different aperture curves were examined. The profiles of these curves are shown in Figure 3.9. The reflection

coefficient versus frequency plot for each of these aperture designs is shown in Figure 3.10. Curve 1 examined how a circular profile affected the reflection coefficient across the spectrum. It was drawn such that the aperture would be within the design size constraints. The reflection coefficient versus frequency was analyzed, and it was found that response was much smoother, but it also raised the reflection coefficient value across the spectrum. In order to determine if it was the circular shape that caused the increase or the size constraints, curve 2 was drawn. This profile neglected the size constraints of the horn to examine the circular profile's effects. The response of the reflection coefficient showed that the circular profile had more of an effect as the response of curve 2 and 1 overlapped each other. Curve 3 was drawn to further investigate this trend. In this profile, the transition from the plane of the antenna to the aperture ending began further inside the antenna. The goal of this simulation was to examine the effects of a slower transition from the horn to the circular aperture. As expected, the response of this aperture was the same as curves 1 and 2. As a circular profile was deemed ineffective, an elliptic profile was examined with curves 4 and 5. It is shown that the elliptic profile provided the desired response of the reflection coefficient in the frequency range as these two designs have overlapping responses. The size constraints were then reintroduced in curve 6. The reflection coefficient is shown to be minimized in the frequency range for curve 6 profile.

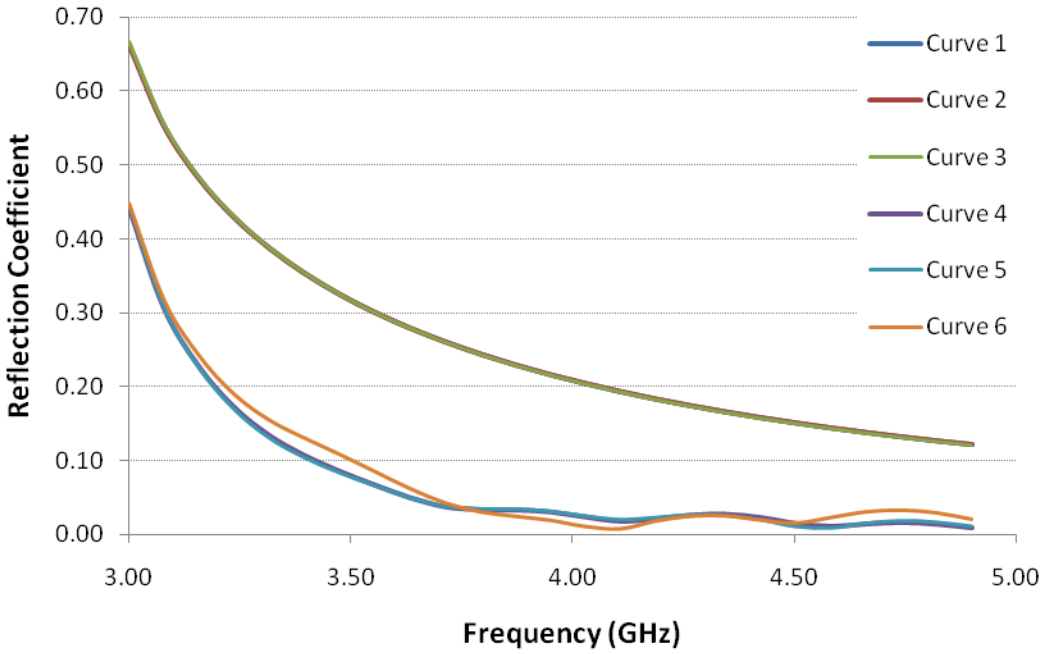

Figure 3.10: Reflection coefficient versus frequency for six curved attached apertures to the conical horn.

With a 3 cm waveguide feed, the three apertures (curve 6, flat plane, no aperture) are compared against each other. The reflection coefficient versus frequency response for each aperture is shown in Figure 3.11. It can be seen that the elliptic profile has its benefits at the lower end of the frequency range, as the reflection coefficient has a lower magnitude. But, its advantages in that range of frequencies do not outweigh other factors. The best choice for an aperture is the flat plane profile. It is shown that is has the best response across the entire range of interest, and has its advantages from a computational perspective. For curved surfaces, many more mesh elements must be constructed around curves in order to properly simulate the geometry, as there are many slow changes. The number of mesh elements was further increased in order to achieve convergence at higher frequencies. This increased number of mesh elements substantially increased simulation time and memory usage. The flat plane surface

required far fewer mesh elements because the features are still linear. Where the elliptic geometry would take 2 days to run 60 frequencies, the flat plane geometry would take 18 hours to run that same set of frequencies. Therefore, all further simulations throughout this thesis involve a horn with the flat plane aperture.

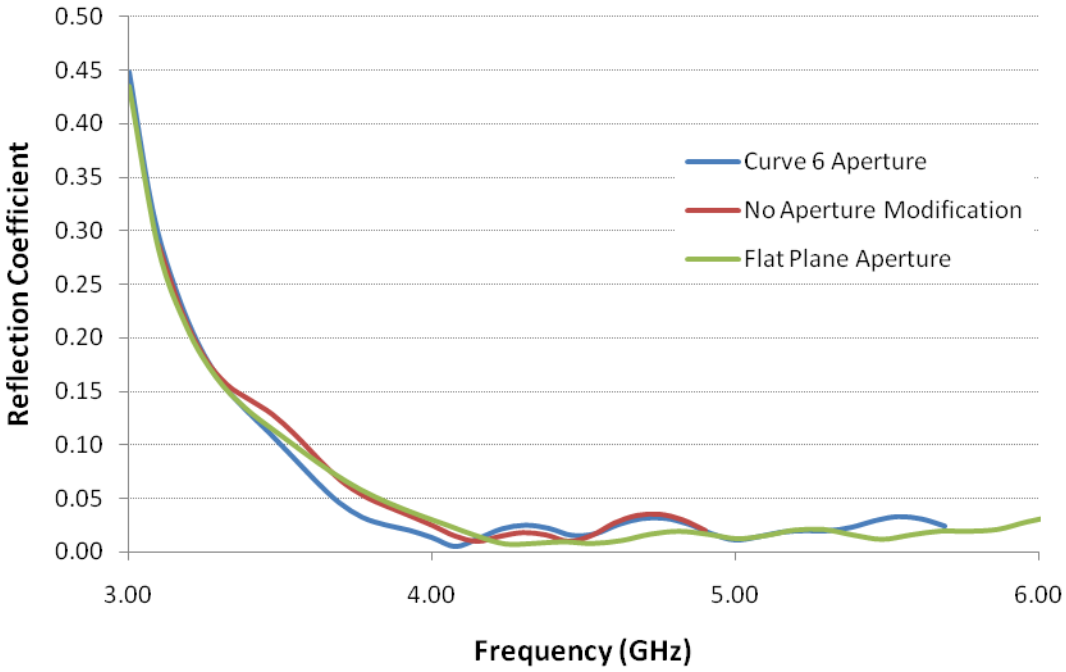

Figure 3.11: Reflection coefficient versus frequency for an added flat plane aperture, added elliptic aperture, and no aperture modification.

Far Field Analysis

Once the reflection characteristics were deemed acceptable, the far field characteristics of the antenna were analyzed. To determine the directivity for a given horn, the electric field in the far field was plotted in the YZ and XZ planes. The half power beamwidth for each plane was then calculated by finding the angles that corresponded with 3 dB below the maximum electric field for a given frequency. Using these perpendicular beamwidths, the directivity was found by using two directivity

approximation formulas used commonly for one main lobe patterns. The first is the Kraus approximation, shown in equation (3.19), and the second is the Tai-Pereira approximation shown in equation (3.20).

$$D_0 = \frac{41{,}253}{\theta_{YZ}\theta_{XZ}} \tag{3.19}$$

$$D_0 = \frac{72{,}815}{{\theta_{YZ}}^2 + {\theta_{XZ}}^2} \tag{3.20}$$

where θ is the half power beamwidth in degrees for each respective plane. The Kraus approximation is more accurate for broader patterns, and the Tai-Pereira approximate is more accurate for narrower lobes [4]. Both of these formulas are used to ensure consistency in results.

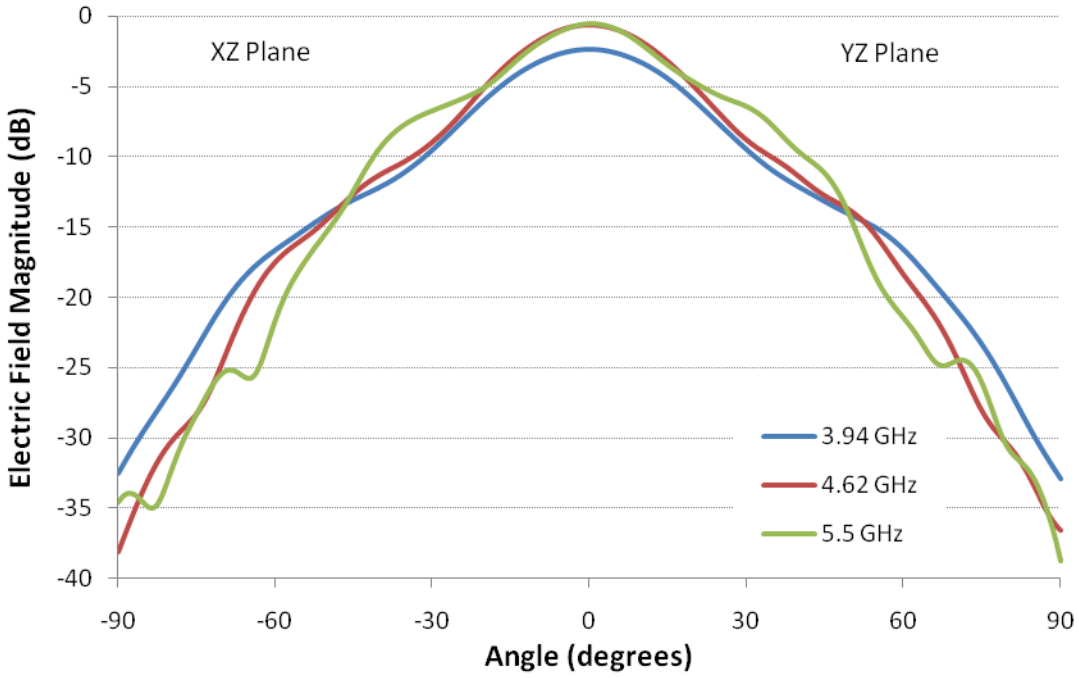

Figure 3.12: Radiation pattern for three frequencies from the original conical horn design based on theory. The XZ plane is shown from -90 to 0 degrees, and the YZ plane from 0 to 90 degrees.

The radiation pattern for the original design from theory is shown in Figure 3.12. Three frequencies are shown, ranging from the low end to the high end of the spectrum of interest. Because the XZ and YZ planes are nearly perfectly symmetric about 0 degrees, Figure 3.12 shows only one half of each plane. For the original design, the directivity varied from approximately 15.5 dB to 17.5 dB across the frequency spectrum. These values stretched too far from the design constraint that the antenna must have a directivity of approximately 10-15 dB.

In order to reduce the directivity, the axial length L was decreased in increments. Axial lengths of 8.2 cm, 7.8 cm, and 7.3 cm were additionally tested. The resulting directivities for each antenna are shown in Figure 3.13. It is shown that as the axial length decreases, the maximum and minimum directivity across the spectrum decreases. For shorter axial lengths, it is shown that the maximum directivity is not at the higher frequencies. This trend relates back to Figure 2.2. At the higher frequencies, the antenna does not operate at the optimal directivity. It operates on the right side of the peak of the characteristic $L = a\lambda$ curve, where a is the wavelength scaling coefficient.

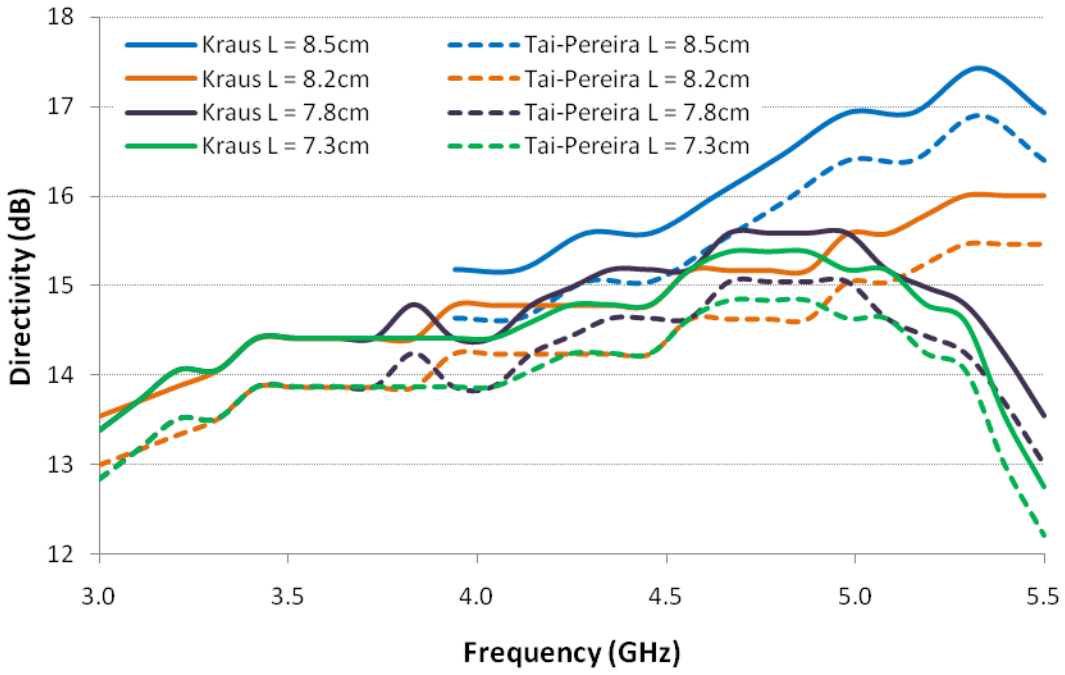

Figure 3.13: Directivity versus frequency for four conical antennas with varying axial length *L*.

Conclusion

Using the studies performed above, the final design of the conical horn antenna was reached. A cross section of the final design with its design parameters are shown in Figure 3.14. An axial length of 7.3 cm was selected because it produced the desired directivity. The feeding waveguide radius was set to 3 cm because it produced the necessary cutoff frequencies and reflection characteristics. The aperture diameter is equal 13.2 cm so that the device meets the size constraints with a flat plane possible at the aperture. The total device length was left at 8.5 cm in order to keep the device as compact as possible in the longitudinal direction.

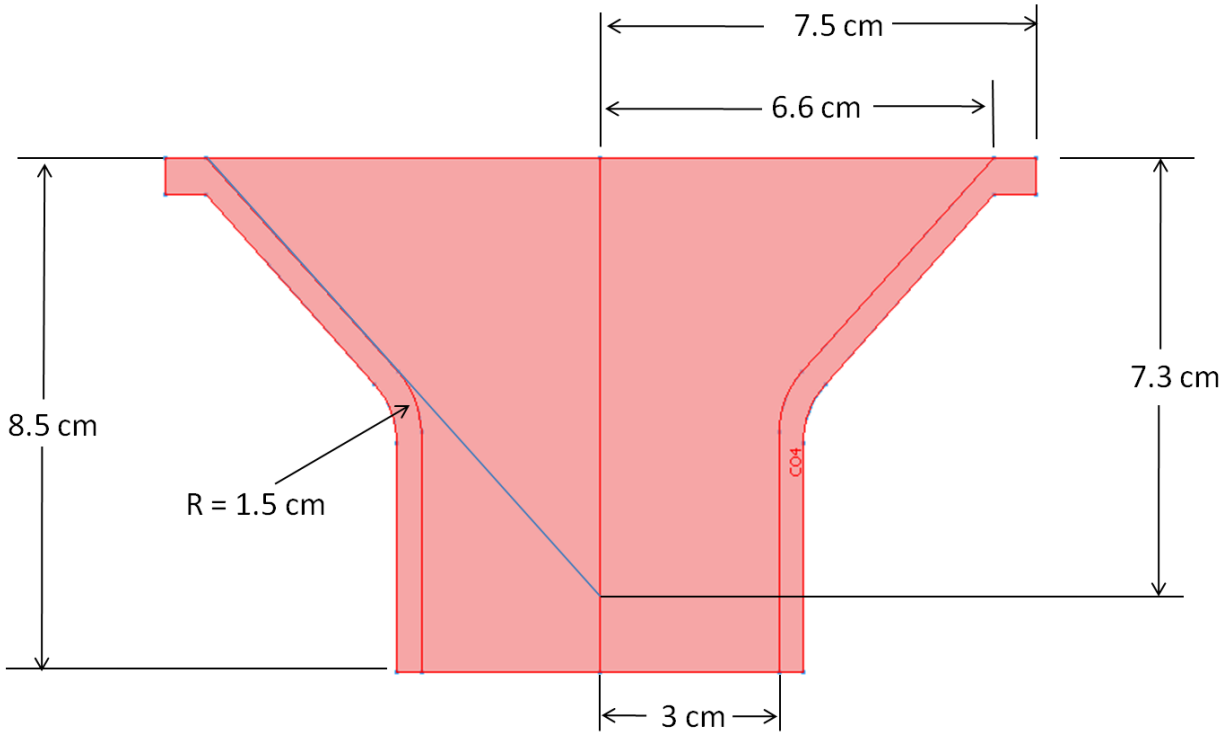

Figure 3.14: Cross section of final design of the conical horn antenna with dimensions of each parameter.

The final design was simulated in COMSOL. The reflection coefficient versus frequency is shown in Figure 3.15. The reflection coefficient remains under a magnitude of 0.05 in the 4 to 6 GHz range. The radiation characteristics of the horn are shown in Figure 3.16. Thirty five frequencies were sampled in the 4 to 6 GHz range, and the electric field magnitude was plotted for each on a scale where 0 dB was the maximum value for the entire spectrum. Figure 3.16 shows the maximum and minimum value for the electric field in the far field, as well as a frequency in the middle of the operating range. The directivity of the device ranges approximately between 12 and 15 dB. All important design criteria have been met for the proposed final design of the conical horn.

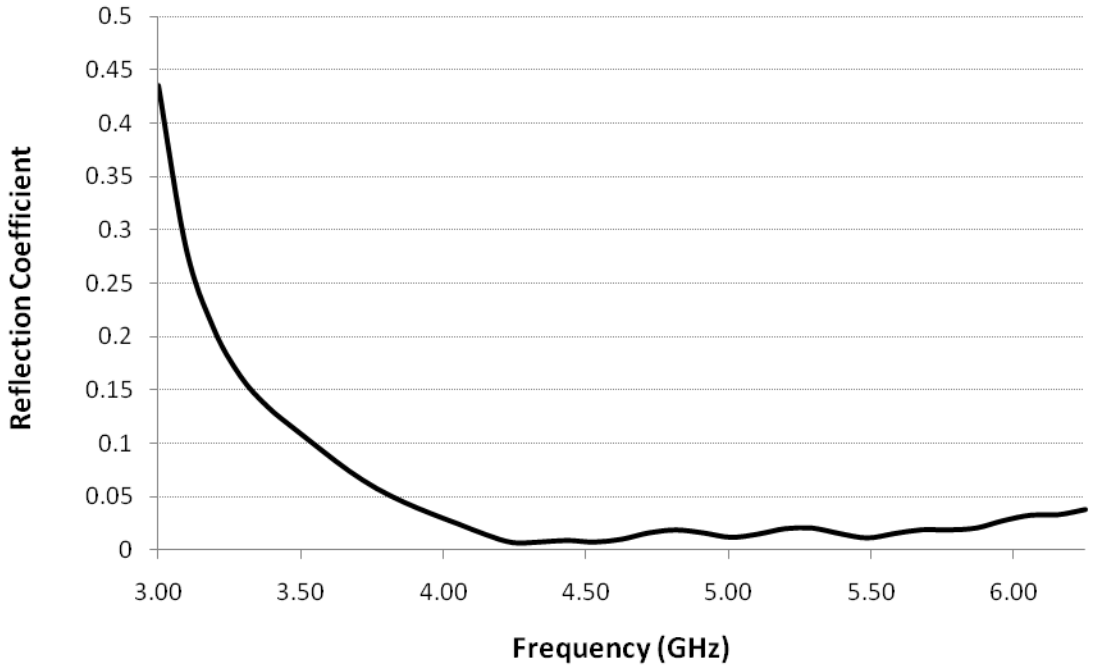

Figure 3.15: Reflection coefficient versus frequency for the final design of the conical horn antenna.

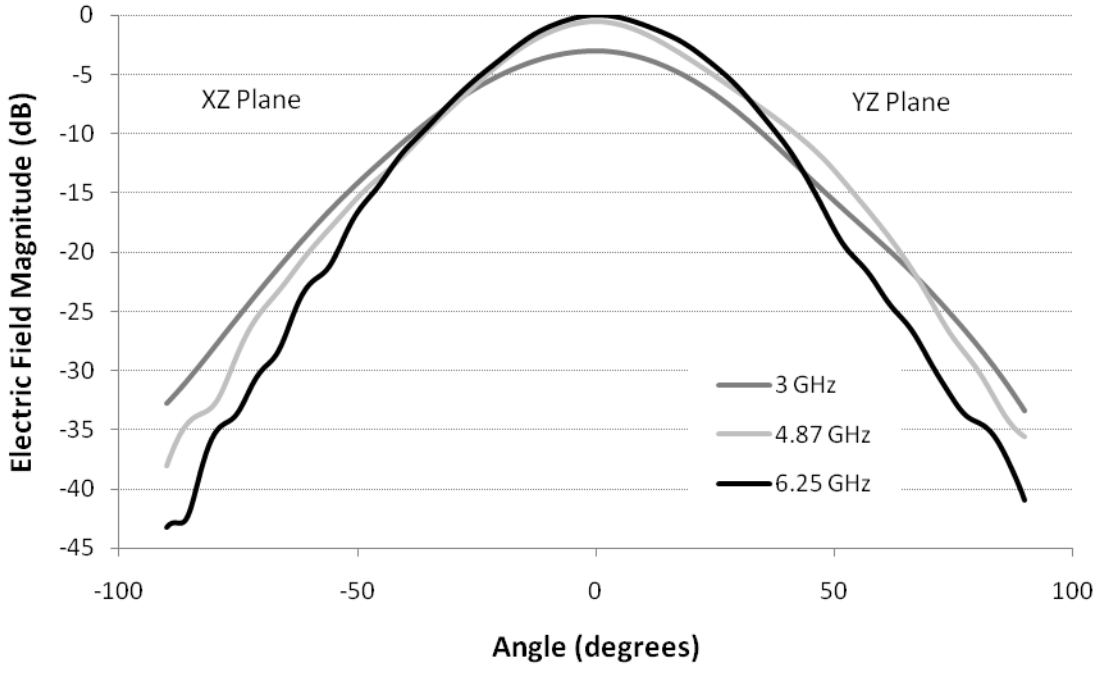

Figure 3.16: Electric field magnitude versus radiating angle for the final design of the conical horn for three frequencies that represent the maximum, minimum, mid range frequencies in the radiating spectrum.

It is important to note how the design would change if the design constraints were altered in any way. Two important parameters that could change are the operating frequency range and the desired directivity. If the source were altered in any way, the operating frequency could change. If the operating frequency spectrum was raised from 4 to 6 GHz to higher frequencies, the feeding waveguide radius would decrease, and the axial length, *L,* would be adjusted to the corresponding wavelengths. If the directivity constraint increased, the axial horn length, *L*, would increase. The goal of this chapter was to produce a design process to be able to produce a horn antenna for any modifications to the design constraints.

Chapter 4

Coupling the Source and Antenna

The conical horn antenna designed in Chapters 2 and 3 meets the constraints for radiation and reflection characteristics. The next stage of development is connecting the antenna to the high power microwave source. This procedure is not as simple as just connecting the 3 cm waveguide on the antenna to the source. The vircator developed at Texas Tech University is currently at the maximum size constraint of 3 inches in radius. In order to couple the source and antenna, a tapered section must be designed that cascades from 7.62 cm in radius to 3 cm that is compact and minimizes reflections. This chapter will discuss the process in which this coupling section was designed, methods taken to improve simulation time, and selection process for a final taper design for the system.

Taper Design

Properties of the high power microwave source greatly influenced the design of the taper connecting the source and antenna. The source generates up to 100 MW of power in the TE_{11} mode and chirps up in frequency from 3 to 7 GHz as time increases. Most of the power from the device is in the 4 to 6 GHz range [24]. It is also important to note that it is possible that the source could produce higher order modes that have vertical electric field profiles in the center. These electric field lines in the center correspond to the vertical electron movement from cathode to anode inside the vircator. Higher order modes that are possibly excited by the device are TM_{11}, TE_{12}, TM_{12}, TE_{12},…TE_{1n}, TM_{1n}. Cross sections of the profiles for the first 30 modes of a circular profile are shown in [33],[36]. Preliminary simulations at Texas Tech have shown that the TM_{11} can be driven at 2.5, 3, 3.6, 4.5, and 5.4 GHz, but have not been verified by experiment. Modes that could be driven and are on center are TE_{12} at 3.4, 3.7, 4.3, 5, 5.9 GHz and TE_{13} at 5.4, 5.6, and 6 GHz. Mode profiles for these modes are shown in Figure 4.1. In this and the next chapter, these higher order modes will be analyzed because of their possible existance. Their greatest influence on the device will be regarding breakdown, but their behavior inside the device is also important.

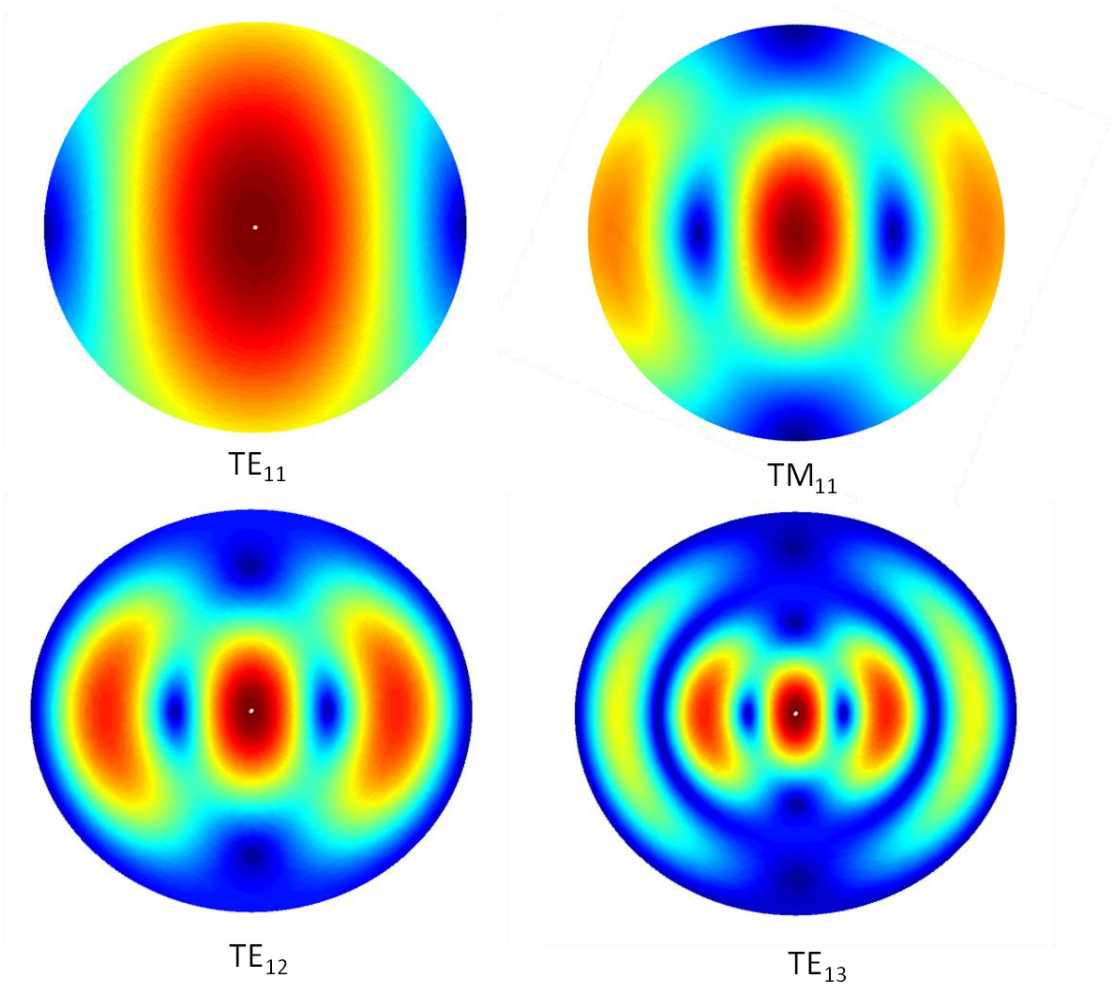

Figure 4.1: Electric field profiles for the possible modes generated by the HPM source.

The primary goal of the taper is to transfer as much power as possible from the TE_{11} mode to the antenna. A device must be designed that reduces the 7.62 cm radius of the vircator to the 3 cm radius of the antenna while transferring as much power as possible. A diagram of the coupling device in the system is shown in Figure 4.2. A tradeoff inherently exists between compactness and the magnitude of the reflection coefficient. The shorter the device is, the more reflection of power back into the source. The aim of simulations is to find a taper that finds a balance between the amount of reflection from the device and the length of the taper, *L*. The linear taper was explored

because a smaller amount of reflection is produced with slow transitions in diameter. A taper that is curved will create a surface at some point along the device that provides more reflection than a constant slope from beginning to end.

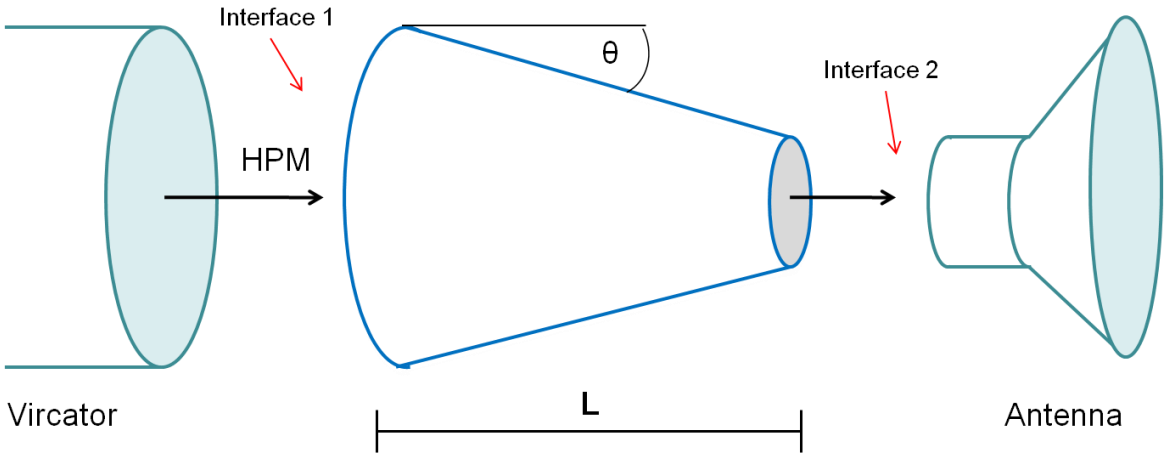

Figure 4.2: System diagram of the coupling device between source and antenna.

Simulations for the taper will analyze the reflection coefficient as a function of the taper length, *L*. The electric field and power flow will be analyzed inside the taper. Also, a method that decreases the simulation time for a particular system layout is determined.

Simulation Setup

The first simulations of the coupling system began by connecting a taper of length *L* to the conical horn antenna. Many of the same settings from Chapter 3 are used for the taper simulations. A port condition was set at interface 1, shown in Figure 4.2, to the circular TE_{11} mode. A mesh was created using the predefined extra fine mesh, but altered such that the element growth rate was set to 1.15, and the maximum element size

was set to 0.025. The parametric version of the GMRES solver was used, the frequency was varied between 3.8 and 6.25 GHz, and the power varied between 1 and 100 MW.

The first simulations performed had the taper coupling to the horn and then radiating into free space. It was found these simulations were impractical and required too much time to complete. Simulations of the entire taper and antenna system were taking on the order of 2 to 3 days for 40 frequencies in the range of 3.8 – 6.25 GHz. Compared to the simulations described in Chapter 3, the larger simulation domain required more mesh elements. Simulations with additional mesh elements increase memory usage and results in increased simulation time. Also, the system may run out of memory before the simulation finishes. For that reason, experiments were performed that would attempt to create a smaller simulation domain and have faster computation times. Faster computation times would allow for more parameters to be swept, and more finely meshed areas of interest.

In an attempt to break up the domain into smaller pieces and reduce simulation time, different cross sections on the device were examined to see if a boundary condition could be created that would approximate the device's behavior from that plane. To determine an appropriate boundary, the electric field at various cross sections in the device was examined. It was found that the mode inside the waveguide that feeds the horn looked very close to TE_{11}. An example cross section is shown in Figure 4.3. Because this mode appeared inside the guide, a TE_{11} boundary condition was placed at the interface between the taper and the conical horn.

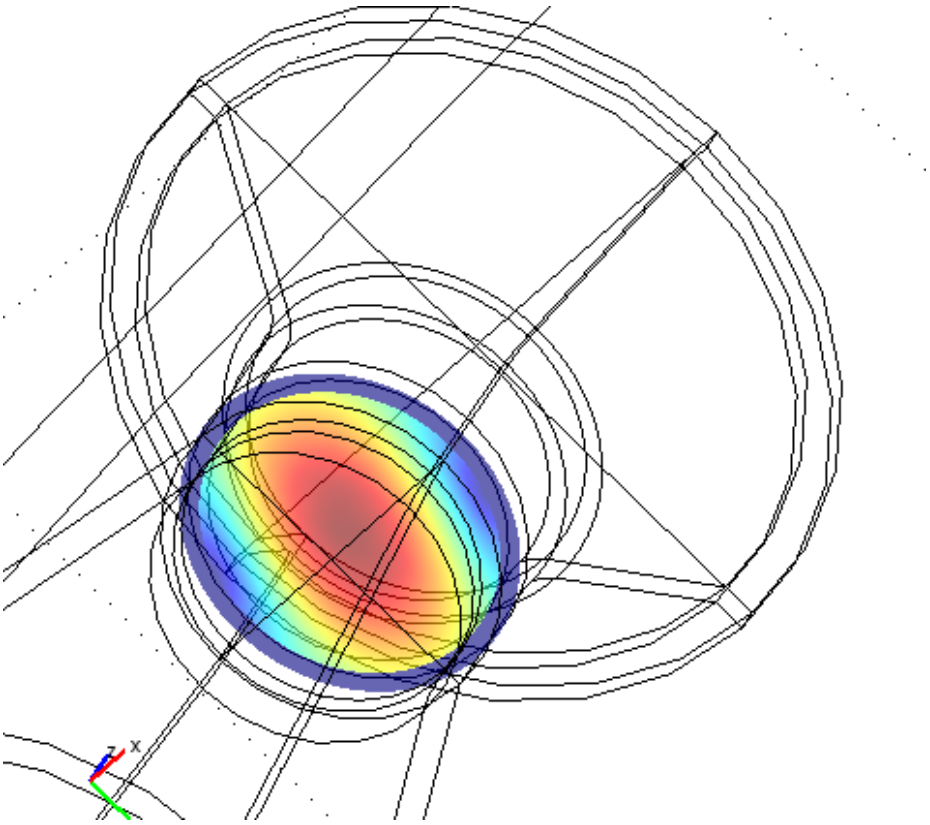

Figure 4.3: Cross section of the TE_{11} mode in the waveguide connecting the taper and horn.

Experiments were then performed that simulated the taper with a port condition set to TE_{11} at interface 2 shown in Figure 4.2. This setup will be referred to as the approximated setup. The reflection coefficient versus frequency trend was then compared between the approximated setup and the full system for three different taper lengths for three different input modes (TE_{11}, TE_{12}, TM_{11}).

After the approximated setup was verified, it was used to do an analysis of the effect of taper length upon the reflection coefficient. Sixteen taper lengths ranging from 4.2 to 29.2 cm long were analyzed. The efficiency of transferring the TE_{11} mode was examined, and the best choice for the length was selected.

Simulation Results

Verification of Approximate Setup

In order to verify the approximate simulation three tapers in three different modes were simulated with the entire taper/waveguide/horn system and the approximate setup. The three tapers simulated had lengths of 2 cm (short), 10 cm (mid), and 20 cm (long), and were analyzed in the TE_{11}, TE_{12}, and TM_{11} modes. The comparisons of the approximated simulation to the entire system are shown in Figure 4.4. It is shown that for the TE_{11} and TE_{12} mode the approximated setup corresponds well with the total system simulations for the entire 4 to 6 GHz range. The TM_{11} has correlation closer to 4 GHz for all taper lengths, but as the taper length increased, the two results diverge from each other at higher frequencies. Because the aim is to maximize power transfer for the TE_{11} mode, the approximate setup is used to analyze the effect of taper length upon the reflection coefficient. The good correlation stems from the fact that the reflection coefficient of the horn has a low magnitude in the 4 to 6 GHz range. For that reason, most reflections will be as a result of the taper, and not the horn. It is important to note that shorter tapers will couple higher order modes into the horn slightly better than longer tapers, but the shorter the taper, the higher the reflection coefficient for the TE_{11} mode. The success of the approximated setup has reduced simulation time from 2-3 days per simulation to 2-3 hours. Using the approximated setup, simulations of the taper could have finer meshes at points of interest, as well as more samples in the frequency range without having unreasonable simulation times.

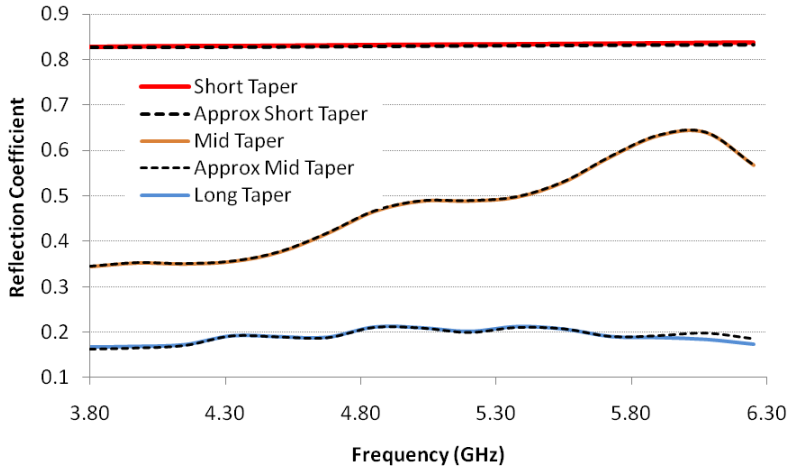

(a)

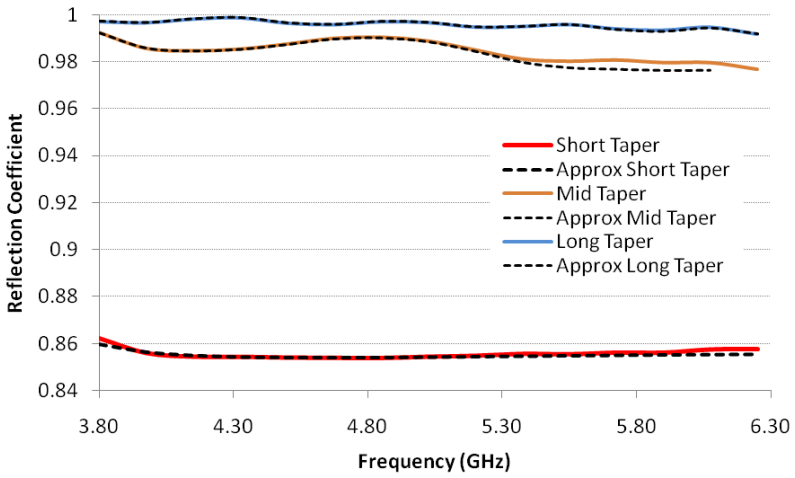

(b)

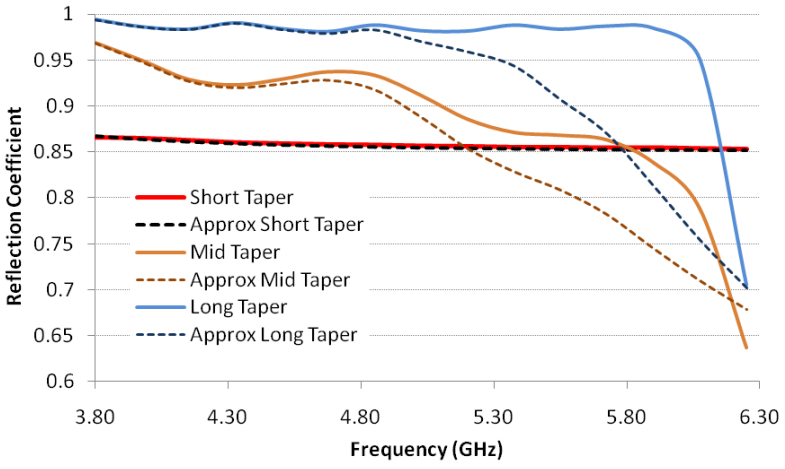

(c)

Figure 4.4: Reflection coefficient comparisons of the approximated setup to the entire system for (a) TE_{11} mode, (b) TE_{12} mode, and (c) TM_{11} mode.

Taper Length vs. Reflection Coefficient

The approximated setup was utilized to find the relationship between the taper length and the reflection coefficient for the input mode TE_{11}. Taper lengths ranging between 4.2 and 29.2 cm were simulated. The reflection coefficient across the spectrum for 6 of the 16 tapers is shown in Figure 4.5. It is shown that as taper length increased, the reflection coefficient decreased across the spectrum. It is inferred that the taper angle has a direct impact on the reflection coefficient, where a taper angle of 0 degrees corresponds to a waveguide of constant radius. As the taper angle increases, the reflection coefficient will increase. In order to reduce the reflection coefficient, the taper length *L* must be increased, but compactness of the device is lost. The selection of taper geometry is dependent on the design constraints, as a balance between compactness and power transfer is found. Currently, a taper length of 20.4 cm is believed to the best selection, as the reflection coefficient has a magnitude of approximately 0.2 in the 4 to 6 GHz range.

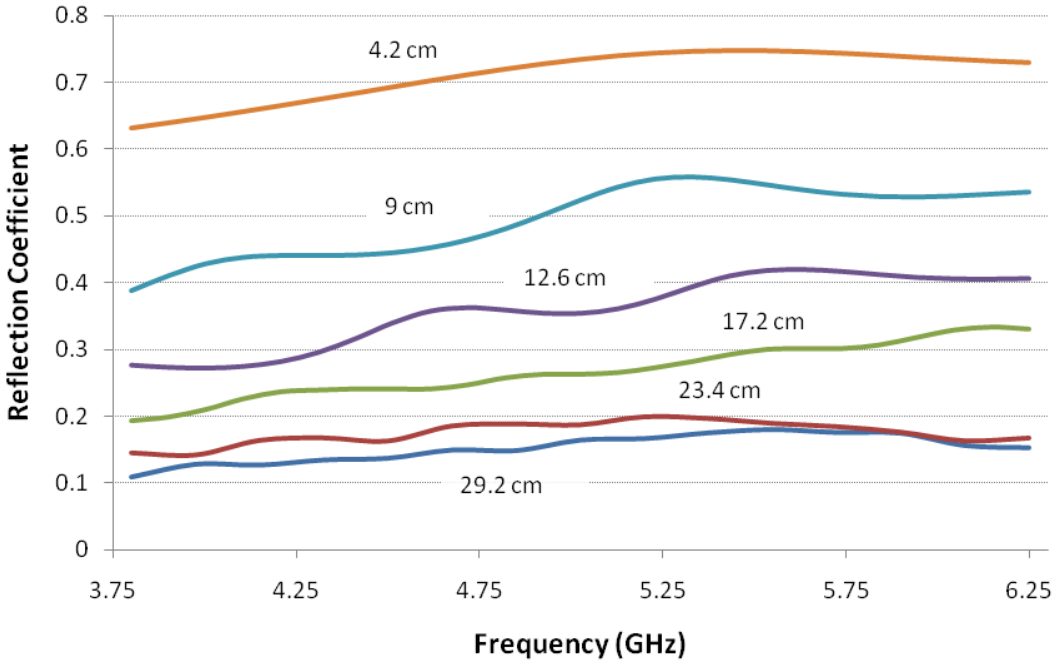

Figure 4.5: Reflection coefficient versus frequency for 6 of 16 taper lengths for an input of TE_{11}.

The power flow and electric field magnitude were also analyzed inside the taper. An example cross section is shown in Figure 4.6. It is shown that electric field profile appears more like the TE_{11} mode as it approaches the feeding waveguide for all tapers across the operating spectrum. There are electric field perturbations near the input port, and they become more apparent near the 6 GHz end of the spectrum. The power flow is in the desired direction throughout the device, with small perturbations near the input end of the device that correspond with electric field perturbations at higher frequencies. These profiles provide insight to the source of reflections in the device.

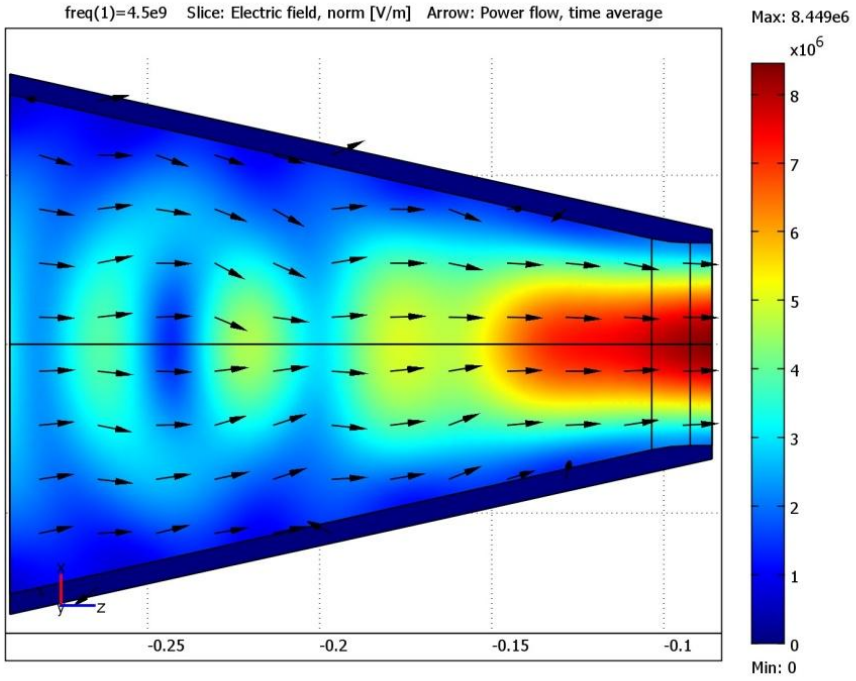

Figure 4.6: Electric field magnitude inside a length 20.4 cm long taper with an input power of 100 MW at 4.5 GHz. The Poynting vector direction is indicated by the arrows.

As shown in Figure 4.4, if higher order modes do exist from the source, they will have a high reflection coefficient. This is because the 3 cm waveguide feeding the conical horn has cutoff frequencies for the TM_{11} (6.1 GHz), TE_{12} (8.48 GHz), and TE_{13} (13.58 GHz) modes that are much higher than 6 GHz. As a result, these modes will be reflected back to the source. It is believed that these modes are at low power, so that is acceptable at this time. The modal characteristics could change as further research is performed on the source. For that reason, it is important to understand the effects of the reflected modes, which is analyzed in Chapter 5.

Chapter 5

Dielectric Window Analysis

Between the source and the antenna, there is a dielectric window that separates the vircator, which is in vacuum, from the air inside the antenna. This window will add reflections due to the discontinuity in the media properties, and therefore decrease the power transfer. The window also is a potential source for breakdown in the device. Preventing breakdown of the dielectric window is essential toward device operation. If the device breaks down, plasma will form at the air-dielectric boundary, and all the power generated from the source will be reflected back or absorbed by the plasma. Research has been performed on window breakdown at Texas Tech University that investigates the physical mechanisms leading to breakdown [2],[37]. Breakdown thresholds, depending on specific geometry and material are on the order of several tens to 100 kV/cm [2]. More recently, research has been exploring breakdown of the air – dielectric boundary at

ground and high altitude pressures [38],[39]. The results from these studies are the motivation behind examining the peak field on the dielectric – air interface, as they will aid in understanding the causes of breakdown if the device were to do so in experiment.

This chapter explores the effect of the dielectric window on reflection and breakdown for the TE_{11}, TE_{12}, and TM_{11} modes by examining the reflection coefficient versus frequency with respect to the vircator, and by looking at electric field magnitudes at the air-dielectric interface. A method that aims to decrease the reflection coefficient across the spectrum is then explored using swarm optimization.

Simulation Setup

To analyze the effects of the dielectric window, a 2 mm thick dielectric cylinder was added to interface 1 shown in Figure 4.2. The same approximate setup from Chapter 4 is used, but for this analysis the input port is the dielectric window. A cross section of the window in the taper is shown in Figure 5.1. The first experiment performed was to analyze the reflection coefficient across the 4 to 6 GHz range with an input mode of TE_{11}. The dielectric window properties were set to common dielectric window materials. Because the selection of window material is not finalized, commonly used materials were studied and included common glass, which has an index of refraction of 1.6, quartz, with an index of refraction of 2.1, and alumina, which has an index of refraction of 3.1 [40],[2].

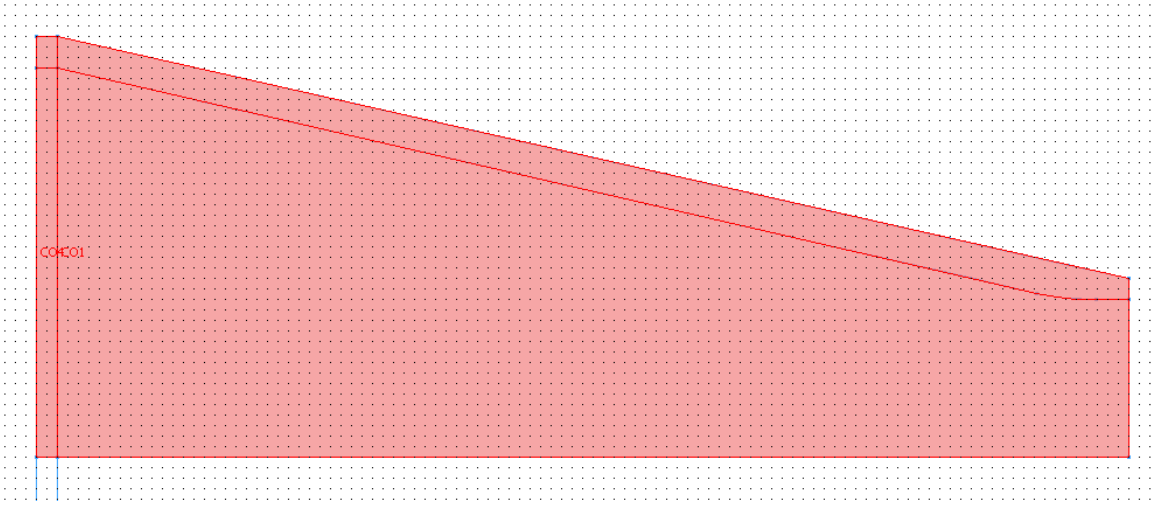

Figure 5.1: Cross section of the taper setup with a dielectric window at the input of the device

After the reflection characteristics were studied, the electric field magnitude on the air-dielectric surface was analyzed. The electric field magnitude on the surface provides insight into possible breakdown of the device. The taper length of 20.4 cm selected in Chapter 4 was the first design analyzed. The peak electric field on the interface was analyzed with 40 samples between 3.8 and 6.25 GHz, at 10 different powers levels between 1 and 100 MW, for the TE_{11}, TE_{12}, TM_{11}, and TE_{13} (when the solution converged). The electric field magnitude on the dielectric window was examined for taper lengths of 15 cm, 17.2 cm, 19.2 cm, 20.4 cm, 25.4 cm, 27 cm, and 29.2 cm. Trends for the field were analyzed, and selection criteria for selecting a taper length based on breakdown potential is formulated.

After the electric field was analyzed, an attempt to reduce the reflection coefficient for the device is explored. An analysis was performed on the effect of adding curvature to the dielectric window to see if it would add a focusing effect, and therefore reduce the amount of reflection from the taper. This lens analysis was performed on the

20.4 cm long taper. The dielectric material is set to common glass, with a dielectric constant of 1.6. The other dielectric constants were not explored at this time, as this analysis is in the proof of concept stage. In order to find the optimal lens curvature, a particle swarm analysis was performed.

Particle swarm is an optimization method that iteratively attempts to improve a set of parameters based on relative error values. At the high level, the particle swarm algorithm is as follows. For all particles, the position is set randomly between an upper and lower boundary in a search space, and the velocity is initialized to zero. Then, until convergence is attained, each particle returns its error value for its set of parameters, and then the error is compared to the global best and that particle's personal best. The positions and velocities are then updated based on the deviation from the global and personal bests, and the next generation is performed.

In the particle swarm implementation, four points in the lens are allowed to vary, and are shown in Figure 5.2. These points create four planes that offer different refraction angles into the taper. The optimal placement of these points is found by minimizing an error value that consists of the sum of the reflection coefficient value and variance of that value in the 4 to 6 GHz range.

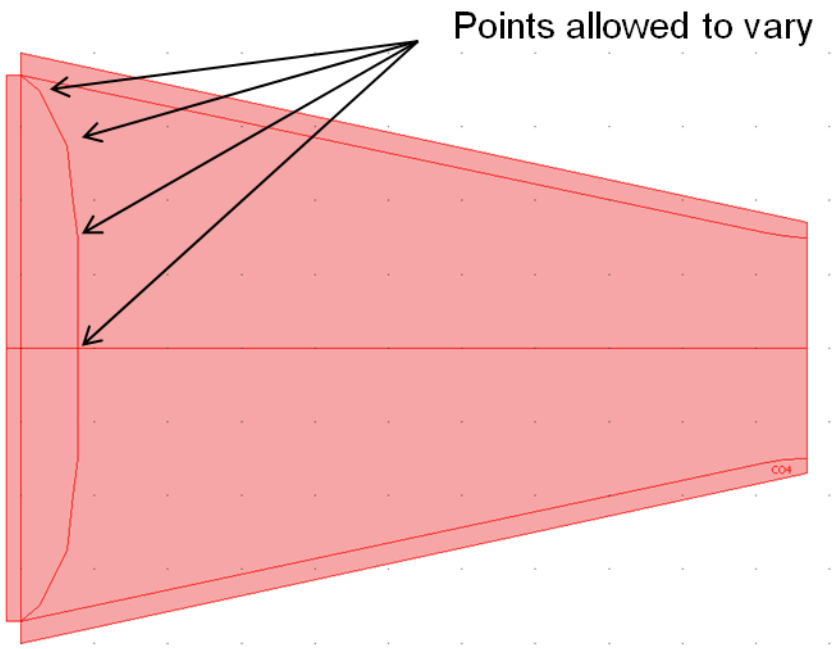

Figure 5.2: Taper shown with four points allowed to vary in the particle swarm analysis.

Simulation Results

Index of Refraction

The reflection coefficient versus frequency was analyzed for the taper of 20.4 cm long with the dielectric window in the simulation. The objective of this experiment was to determine how much reflection was added from the discontinuity in media. The TE_{11} mode was injected into the dielectric window. The reflection coefficient across the spectrum is shown in Figure 5.3. It is shown that as the index of refraction increases, the reflection coefficient across the spectrum increases. This result adds another level of complexity as it has a direct impact upon taper selection. A balance must be achieved between reflection, compactness, and window material. If compactness is most important, then a higher amount of power reflected must be tolerable, or a material with

an index of refraction closer to 1 must be used. If transfer of power is most important, then a longer taper should be selected. If the window material is the limiting factor, then the taper length should be selected accordingly. Ultimately, the selection of the dielectric material is dependent on its effects on the source.

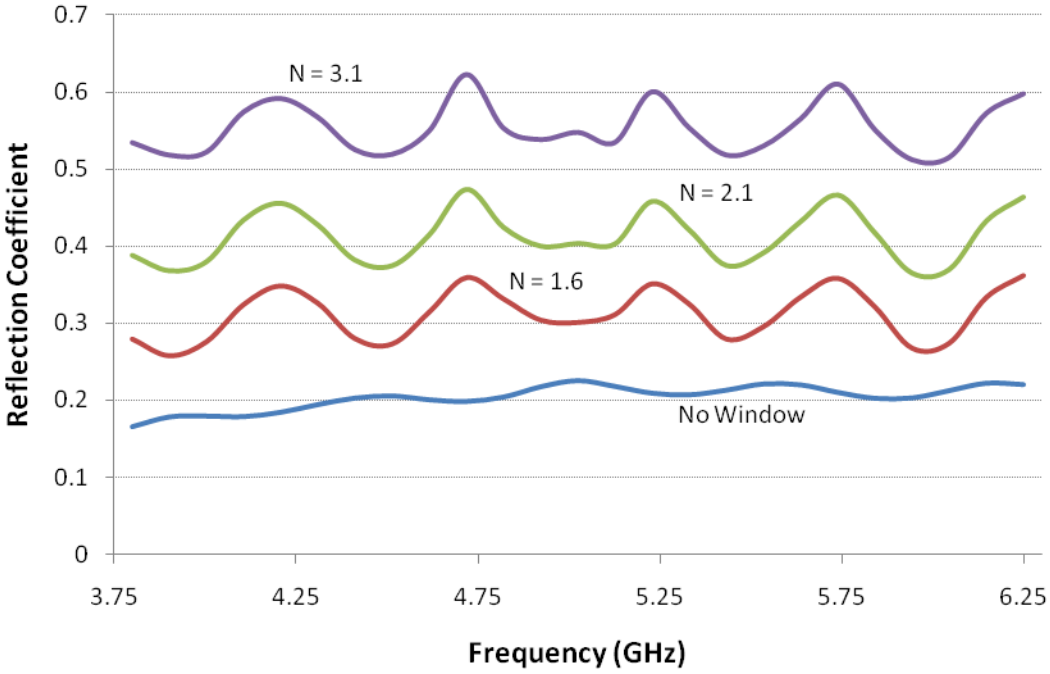

Figure 5.3: Reflection coefficient versus frequency for a 20.4 cm long taper and dielectric window with indices of refraction of 1, 1.6, 2.1, and 3.1.

Interface Electric Field Analysis

The electric field magnitude was analyzed on the air-dielectric interface to see if breakdown is possible. Six taper lengths were analyzed for each dielectric material across the spectrum at multiple power levels. The first goal was to find an expression that will predict the peak electric field as a function of power. In order to do so, the peak electric field was analyzed as a function of input power for each mode. It was found that

a power law regression fit correlated to each frequency. The peak electric field on the interface for any power level can be found through equation (5.1)

$$E_{peak} = A * Power^{1/2} \tag{5.1}$$

The coefficient A is the result of the power law regression. The coefficient A, measured in V / m*Power$^{1/2}$, proves extremely beneficial, as the antenna system can be easily modified as the source's output power increases. If the power level for a given mode is known, the peak electric field due to a mode is found by looking up the coefficient A from the corresponding figure, and utilizing equation (5.1). The maximum possible electric field magnitude is the superposition of the electric field magnitudes for all present modes from the source at their respective power level. As the source is further characterized, these breakdown graphs will provide insight to necessary modifications to the radiating system to prevent breakdown and maximize power transfer. The peak electric field can be compared to dielectric window breakdown studies, and if the electric field is found to be too high, the taper length can be adjusted. For example, the 20.4 cm is connected to the vircator through common glass, and it is found from source data that 5 GHz is driven strongest at 75 MW in the TE_{11} mode. The peak field on the dielectric window would be found by finding the coefficient A for the taper length 20.4 cm at 5 GHz (Figure 5.4a), which is equal to 305, and inserting into equation (5.1) to find a peak field of 26.41 kV/cm.

A full set of plots for the electric field divided by Power$^{1/2}$ for all taper lengths simulated is shown in Appendix B: Electric Field per Input Power$^{1/2}$ Graphs, but the trends for the 20.4 cm long taper developed in Chapter 4 are shown in Figure 5.4. If the TE_{11}, TE_{12}, TE_{13}, and TM_{11} modes are all present in the system at the same power level,

the TE_{11} mode will contribute least to the electric field magnitude, and the TE_{13} will contribute most. At this time, the TE_{11} results are most important as it is believed to carry a much higher percentage of the total power. Therefore, the window and taper should be designed around the TE_{11} mode's contribution. For that reason, the coefficient A for the TE_{11} mode is compared based on index of refraction, and is shown in Figure 5.5. It is shown that as the index of refraction is increased, the electric field / $Power^{1/2}$ decreases slightly. This trend is true for the other modes as well. While the reflection coefficient is larger for a higher refractive index, the peak field is lower. It is believed this is a result of the coherence of the transmitted and reflected wave at the interface. This phenomenon also introduces another trade off of the system, which is reflected power against breakdown threshold.

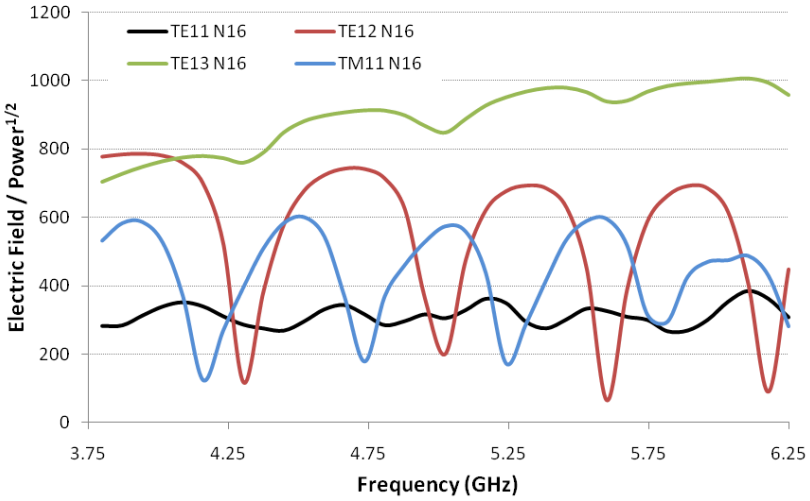

(a)

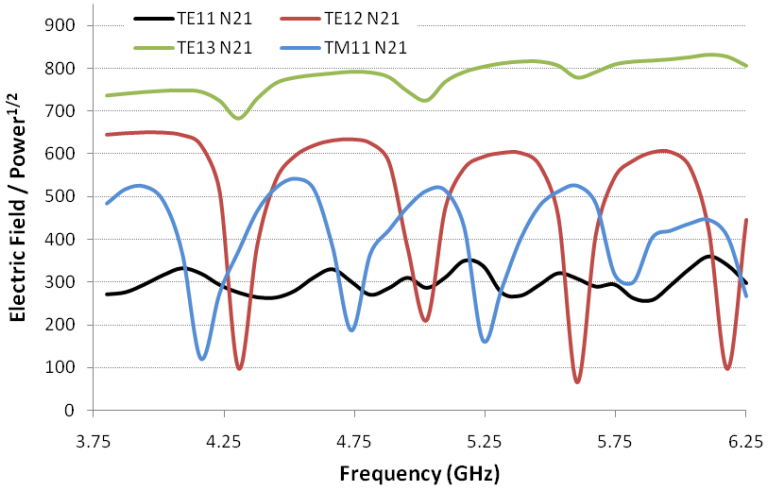

(b)

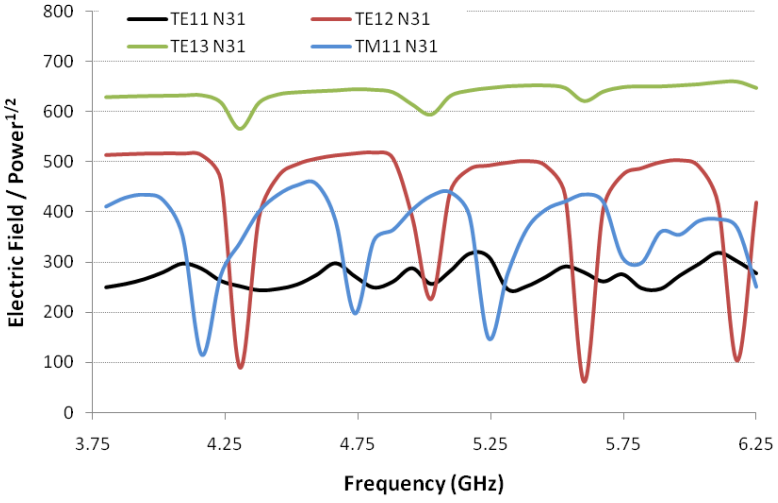

(c)

Figure 5.4: Electric field / Power$^{1/2}$ versus frequency for the TE_{11}, TE_{12}, TE_{13}, and TM_{11} for a taper length 20.4 cm with a dielectric window of index of refraction (a) 1.6, (b) 2.1, and (c) 3.1.

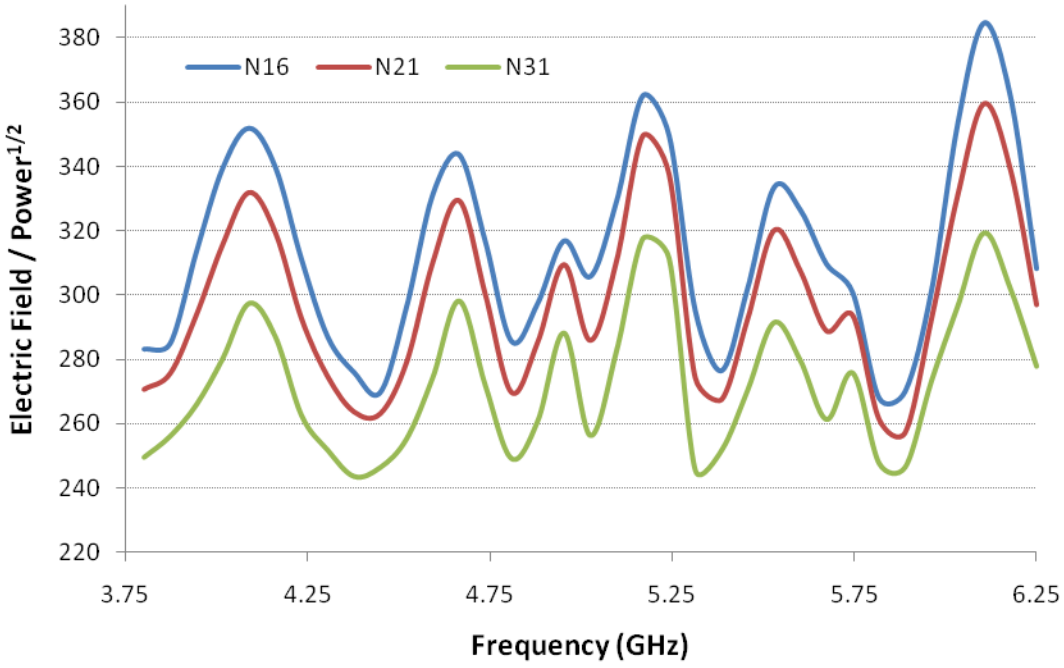

Figure 5.5: Electric Field / Power$^{1/2}$ for the TE_{11} mode at each index of refraction.

The maximum peak power from the vircator to date is estimated at 135 MW [24]. Without the antenna connected, the vircator has not experienced any window breakdown at this power level [41]. Assuming that this power level is at every frequency, the maximum value for the electric field / Power$^{1/2}$ is found at 6.11 GHz. In the worst case scenario, the a peak electric field is 44.6 kV/cm for an index of refraction of 1.6, 41.7 kV/cm for an index of refraction of 2.1, and 37.1 kV/cm for an index of refraction of 3.1. Currently, it is believed these values will not produce the conditions necessary for breakdown, and the 20.4 cm taper length will be the first constructed device for experiment.

The effect of taper length on the maximum possible peak electric field was examined. The TE_{11} mode was analyzed with an index of refraction of 1.6. Values for

higher indices of refraction will correspond to lower magnitudes of the peak electric field, exhibiting the same trend as Figure 5.5. For each taper, the maximum electric field / Power$^{1/2}$ value was found in the 4 to 6 GHz range, and it was assumed that each frequency carries equal weight. The results, shown in Figure 5.6, demonstrate that a longer taper will not significantly reduce the peak electric field on the interface. If the assumptions hold true, more power will be transferred with a longer taper, but the peak electric field on the interface will not increase substantially. The downside of this result is that if breakdown is present when the system is tested, other methods need to be explored to decrease the production of secondary electron emission on the dielectric surface, such as adding a TiN or slightly conductive coating [2].

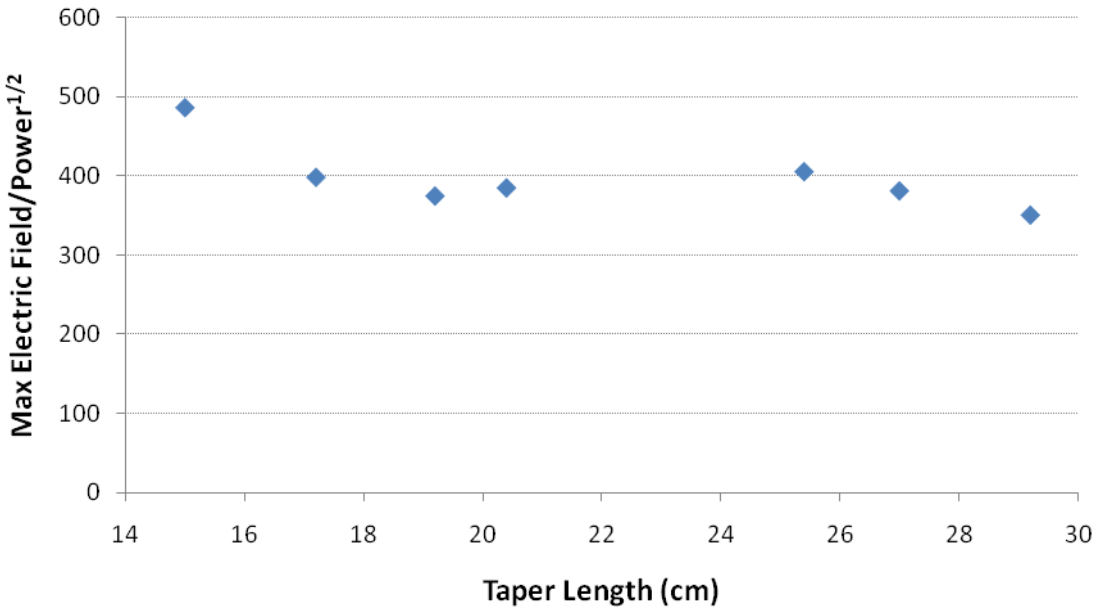

Figure 5.6: Maximum Electric Field/Power$^{1/2}$ of the TE_{11} mode for taper lengths between 15 and 30 cm long with an index of refraction of 1.6 in the dielectric window.

Window Curvature Results

Adding curvature to the air – dielectric boundary was explored in order to examine if the reflection coefficient could be improved in the 4 to 6 GHz range. Reducing the reflection coefficient will increase the power transfer of the system. Initial curves simulated showed that the reflection coefficient was improved. For that reason, the particle swarm optimization method was utilized to minimize the reflection coefficient by finding the optimal position of 4 points on the interface. These four points created planes which refracted incoming waves at different angles. Waves close to the outer diameter of the device need to be refracted more than waves at the center of the device, and the optimization results proved this by creating sharper angle planes near the edge, as shown in Figure 5.7.

In this proof of concept experiment, the index of refraction of the dielectric material was set to 1.6, and the dielectric window coupled to a 20.4 cm long taper. After 7 sets of runs of particle swarm, with each successive run using the optimized result from the previous run, it was concluded that the reflection coefficient would not improve further. A cross section of the proposed lens is shown in Figure 5.7. The reflection coefficient versus frequency for the flat window is compared to the optimized window in Figure 5.8. It is shown that a substantial decrease in the reflection coefficient across the spectrum exists. A major downside to the optimization process is time to solution. Because each individual set of parameters takes on the order of 45 minutes to run, finding the optimal system using particle swarm took approximately 2.5 weeks. For that reason, the algorithm was not tested on multiple tapers or other indices of refraction at this time. As future work continues on this project, the manufacturability of such a dielectric

window needs to be investigated. Also at concern is the effect on breakdown. Field enhancement will exist as a result of the curved surface and sharp points. As these concerns are explored, further simulations using the particle swarm technique should be performed. As work continues on this project, this curved dielectric window should be constructed and tested if deemed economical and manufacturable.

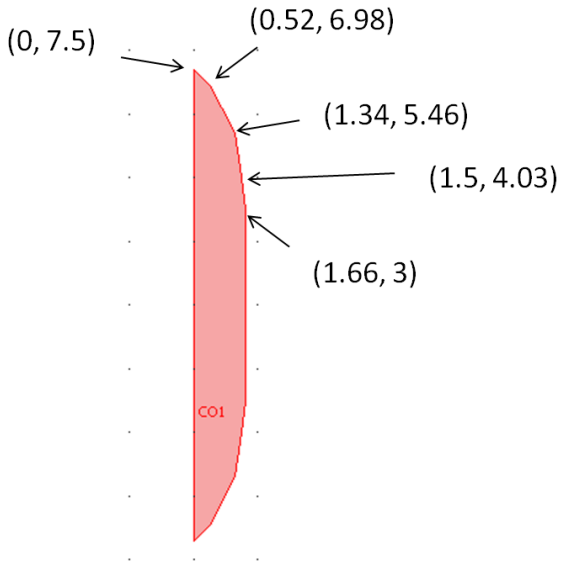

Figure 5.7: Geometry of optimal lens shape for the dielectric window with index of refraction of 1.6. Coordinates are on a centimeter scale.

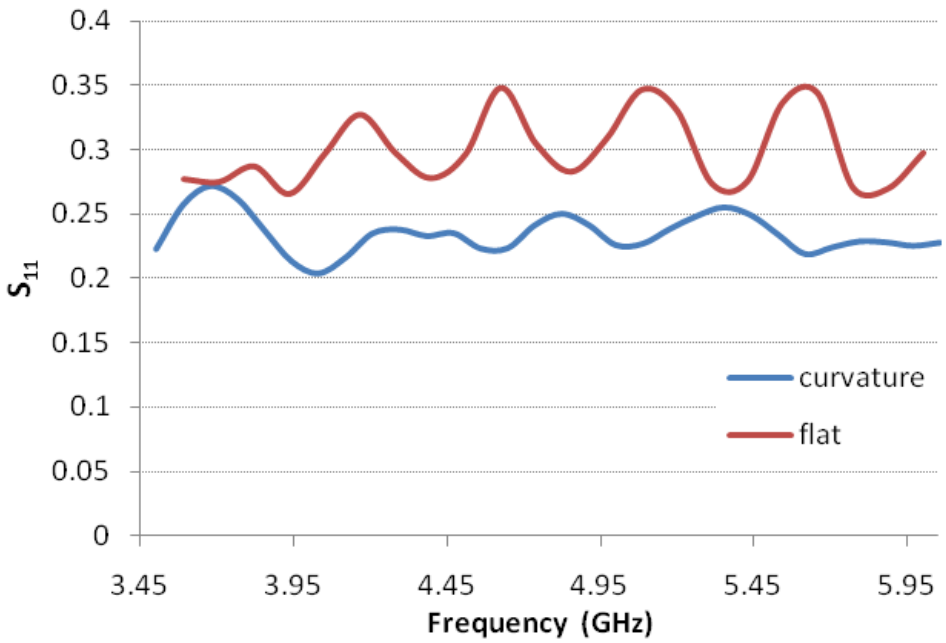

Figure 5.8: Reflection coefficient versus frequency of a dielectric window with index of refraction equal to 1.6 for geometries of flat and the optimal curvature found from swarm analysis.

Chapter 6

Conclusions and Future Work

Conclusions

The University of Missouri has performed electromagnetic simulations for a compact radiating system designed for the compact triode vircator developed at Texas Tech University. The first stage of development was to design a conical horn antenna that maximized power transfer of the TE_{11} mode and produced a directivity of approximately 10 dB. Conical horn design theory from previous works was consulted, and a preliminary horn design was constructed. This design was then simulated in COMSOL Multiphysics, a finite element method software. The reflection coefficient across the 4 to 6 GHz range was analyzed, and it was shown that reflected power was not acceptable across the spectrum. Afterwards, studies were performed that would provide

insight into reflection characteristics. The radius of the feeding waveguide was varied, and it was found that this radius contributed to a shift in the reflection coefficient response. Next, the curvature of the waveguide to horn transition was studied, and it was found that the reflection coefficient across the spectrum did not have dependence on this curvature. The aperture geometry's effect on the reflection coefficient was studied, and it was found that a flat plane produced the best reflection characteristics. Once reflection characteristics were deemed acceptable, far field properties of the antenna were analyzed. Directivity of the device was calculated from the Kraus and Tai-Pereira approximation formulas, which utilized far field half power beamwidths. It was found that the design based on theory produced a more direct system than desired, and the directivity was reduced by decreasing the axial length of the conical horn. All modifications to the conical horn were motivated by simulation results, and a horn geometry was designed that had a reflection coefficient magnitude less the 0.05 in the entire 4 to 6 GHz range, and radiated the TE_{11} mode between approximately 12 and 15 dB across the entire operating range.

After the conical horn was designed, a coupling device between the high power microwave source and the antenna was developed. A taper geometry is selected because the output aperture of the source is at the maximum diameter set by the design constraints. The taper geometry will produce reflections, and experiments were run to reduce the reflection coefficient. A simulation setup was found that reduced simulation time from days to hours, and was used to find the effect of taper length upon the reflection coefficient. It was found that as the taper angle decreased, the reflection coefficient across the spectrum also decreased. A tradeoff between compactness and

taper length was found. The electric field magnitude and power flow in the taper were also examined.

Once the effects of the taper were known, a dielectric interface was added to the system and simulations were run to investigate the impact of the dielectric upon the reflection coefficient and window breakdown. The dielectric materials analyzed had indices of refraction of 1.6, 2.1, and 3.1. It was found that the reflection coefficient versus frequency increased when a dielectric window was added and as the value of its index of refraction increased. The TE_{11}, TE_{12}, TE_{13}, and TM_{11} modes were investigated as they have the potential to exist in the system. A power law regression was used to find the relationship between the peak electric field and the power level of each mode. The resulting electric field / $Power^{1/2}$ coefficient leads to the ability to find the peak electric field on the dielectric window, and therefore the ability to predict breakdown of the surface. It was found that the peak electric field on the dielectric surface was loosely dependent on the taper length of the device. A longer taper would increase the power transfer, but had little effect on the peak electric field on the surface. It was found that adding curvature to the dielectric window would decrease the reflection coefficient across the spectrum. A particle swarm optimization method was utilized to find the optimal curvature for a taper length of 20.4 cm with a dielectric material with index of refraction equal to 1.6. The feasibility of constructing this window and its affect on window breakdown still need to be explored.

Coupling the knowledge from all studies performed, a proposed design for testing is drawn. The radiating system with all dimensions is shown in Figure 6.1. The first

round of testing should construct the antenna out of aluminum, as that proves most economical.

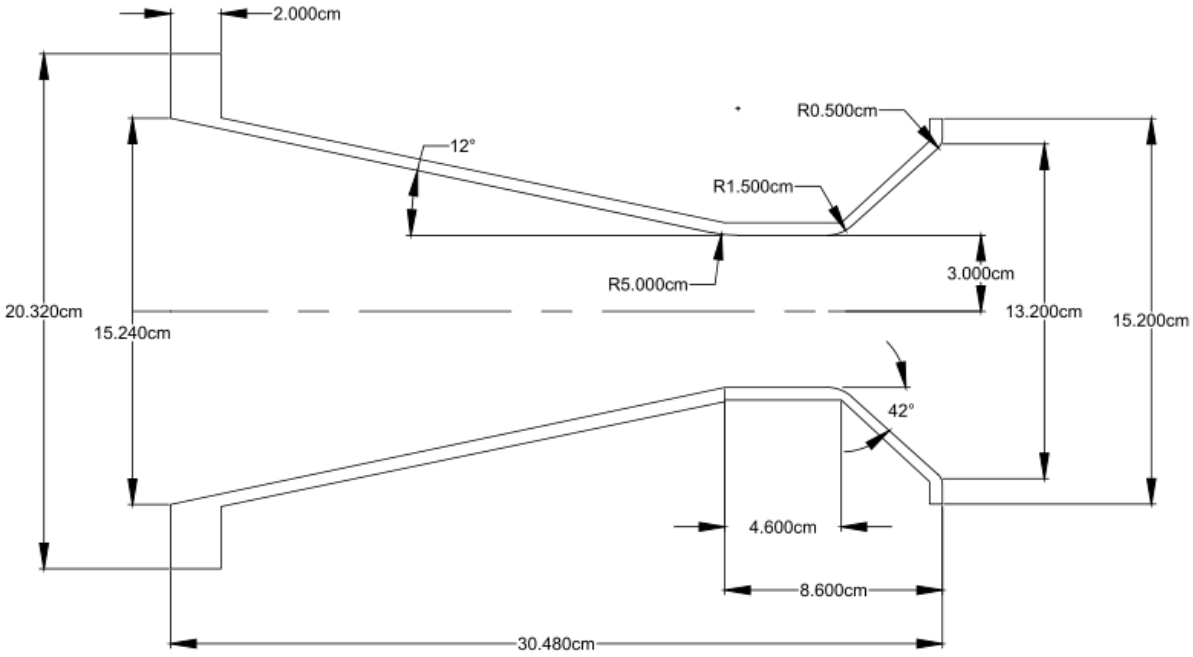

Figure 6.1: Dimensions of the compact radiating system to be built and tested.

Future Work

The material presented goes into much depth of the design of a radiating system, but the next step is to verify the expected properties through experiment. After initial testing of the device shown in Figure 6.1, the results of the experiment should be compared to theory, and the device should be altered based on results presented in this thesis if any variance from simulation exists.

The use of microwave optics on the dielectric window should also be further explored, as only the preliminary research has been completed through particle swarm analysis. Much has been studied in the realm of microwave optics at low powers [42],

and the findings at low powers could very well be applicable to high powers. Creating an effective microwave optic system may lead to making the radiating system more compact. The benefits of adding curvature to the dielectric window will need to be investigated through experiment, as not much information is known about the curvature's effect on window breakdown. Also, it may be possible to use layered films on the dielectric surface to produce an antireflecting boundary [43]. The use of thin film should be explored to reduce the reflections due to dielectric discontinuity.

If window breakdown of the dielectric surface is found to be an issue, and it is believed to be due to the reflection of higher order modes, it could be possible to create an aperture on the taper that couples only higher order modes. The aperture would cause those higher order modes to radiate outside the device and not be reflected back toward the source. Minimization of the reflected wave would most likely decrease the electric field magnitude on the dielectric window. Information regarding microwave aperture coupling is found in [44],[45].

Each area of further research greatly depends on the results from the comparison of simulation and experiment. Once the experiment has been performed, and the results analyzed, it is certain that many other potential outlets for future work will present themselves.

Appendix A: COMSOL Multiphysics RF Module

Once preliminary horn design was complete with the consultation of previous works, the device was simulated in COMSOL Multiphysics, a finite element software [46]. Before the process behind setting up the simulation is discussed, how the RF module of COMSOL operates will be reviewed [34]. The following paragraphs describe how to setup a simulation by first discussing subdomain and boundary conditions, then moving toward meshing of the problem, solver selection, and finally to how to analyze simulation results.

When loading COMSOL, there is an option to select between a space dimension of either 2D, 3D, or axially symmetric. All simulations for the radiating system were completed in the 3D and in the RF Module of COMSOL. There are three different solver systems in the RF module to apply to the simulation and include: Electromagnetic Waves, Boundary Mode Analysis, and Electo-Thermal Interaction. The Electro-Thermal Interaction solver system solves the simulation domain for the exchange of heat between an object and RF waves. The Boundary Mode Analysis system solves for the electric and magnetic fields of a plane with an arbitrary boundary in a 3D system. The user selects from an option of TE, TM, or Hybrid-Mode Waves to perform the analysis. The final solver system in the module is the Electromagnetic Waves solver. It will solve a system in a mode of harmonic propagation, eigenfrequency analysis, or transient analysis. This solver system is selected for the radiating system.

After the RF Module is opened, the user is set to the drawing domain by default. There are multiple methods to draw a system in COMSOL. The first method is to draw

the object in 3D. COMSOL provides basic shapes such as cubes, cones, cylinders, ellipsoids, and spheres to create a geometry. The next method is to enter create a work plane in 2D from the 3D space. The user is able to draw the shape in 2D via lines, 2nd and 3rd order Bezier curves, squares, circle, ellipses, and fillets. Once an object is drawn in 2D, it is the extruded or revolved to embed it into the 3D geometry. In both of the 3D and 2D modes, functions exist to edit the shapes, such as array, mirroring, rotating, chamfering, filleting, and scaling, as well as functions to do the union, intersection, and difference between multiple objects. The third method to enter geometries into COMSOL is to use the import from CAD file module built into COMSOL. This feature is useful for simulation domains that have complex shapes.

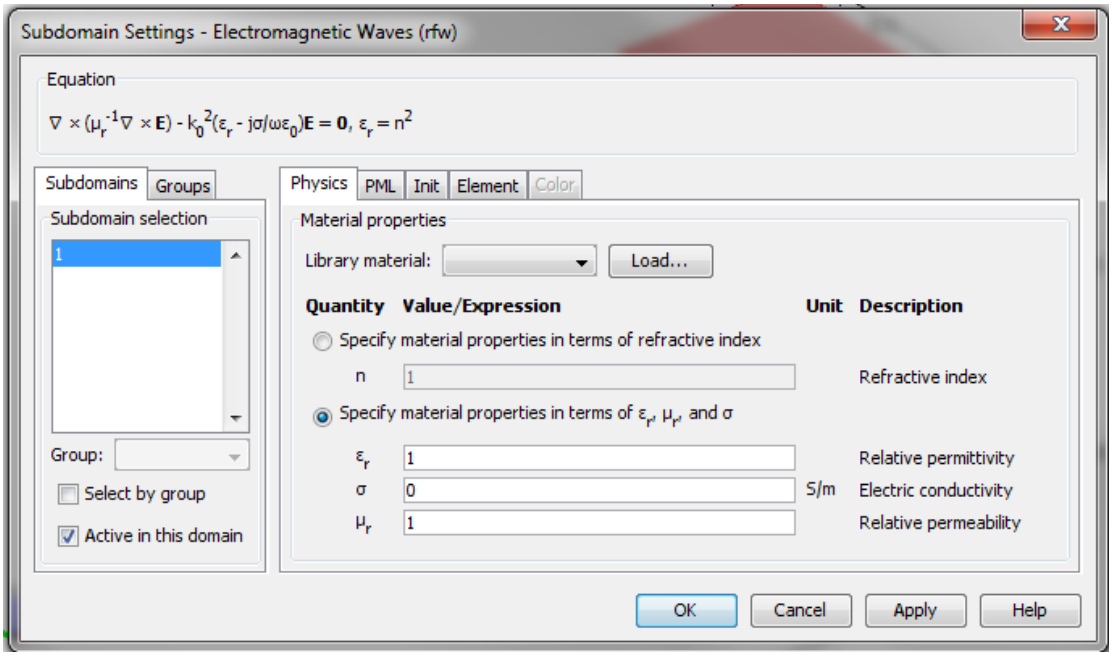

Figure A.1: Screenshot of subdomain screen in COMSOL Multiphysics.

Once the system has been drawn or imported into COMSOL, the simulation properties under the physics menu must be defined for the system. The first settings to

set are subdomain settings. These settings set the properties of solid objects in the simulation domain, and the input screen can be seen in Figure A.1. When using the RF toolbox, there are two ways to set the electromagnetic properties of the system. The first option is to set the refractive index, and the second option is to set the material properties in terms of relative permittivity, electric conductivity, and relative permeability. If these values are not known, COMSOL provides a material library in which the values of these properties can be imported for common materials. If the action is successful, the values will be in bold font in the respective value's field. If the value is not in bold, the user must enter the value.

After the physics settings are set, there are three additional tabs of settings that only apply for special cases. The element tab allows for custom shape functions, integration orders, and constraint orders. There is also a tab for initial conditions for the subdomain. Initial conditions for the x, y, and z components of the electric field, as well as the divergence condition variable can be set. The default value for each of these inputs is zero. The final tab is the PML settings, which stands for perfectly matched layer. These settings are utilized if a subdomain is used to simulate an absorbing boundary condition. The PML is used widely in antenna problems that radiate into free space so its implementation will be explained in detail.

In the RF module, for a PML that absorbs waves in the direction *t*, the PML implementation in COMSOL uses the following coordinate transformation inside the PML:

$$t' = t\frac{\lambda}{\delta t}(1 - i) \tag{A.1}$$

where t is the coordinate, and δt is the width representing the infinite element region. The values of t and δt are populated via COMSOL from its ability to deduce them from the drawn geometry. They are stored in a variable referred to as a guess variable under the naming convention of <param>_guess_<application mode>. When the width of the guess variable is equal to the actual width of the PML region, the coordinate scaling alters the wavelength such that it is equal to the PML region width. In small geometries, where the size of the geometry is smaller than the wavelength of the system, it is better to keep the wavelength unchanged in the PML region. To obtain this effect, enter lambdaS_<application mode> as the PML region width. To further reduce reflections, the scattering boundary condition is set on the outer region of the PML.

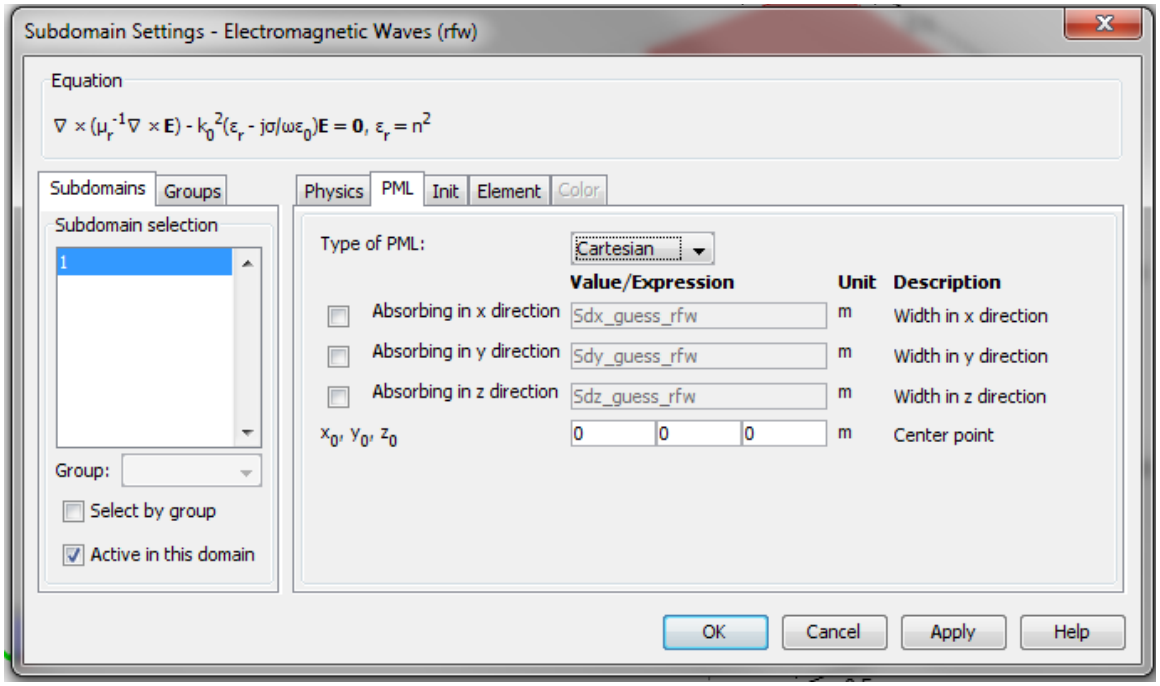

Figure A.2: PML tab in the subdomain settings in COMSOL Multiphysics.

To set up a PML, a PML type must be selected in the PML tab, which is seen in Figure A.2. The PML type is dependent on the geometry and the type of waves traveling

in the subdomain. The options are cartesian, cylindrical, spherical, and user defined. The cartesian PML absorbs waves in the x, y, and/or z directions. The user can select any combination of directions for absorption, e.g. x and y; x, y, and z; etc. The cylindrical type is beneficial in 2D simulations, as the user can select waves to be absorbed in the radial direction. In 3D, in the cylindrical setting the user can select absorption in the radial, z, or both directions. The spherical PML type is the most beneficial for antenna problems, due to the fact that the radiated waves are spherical waves in the near field region. The spherical PML will absorb waves in the radial direction. For each of the PML types, the value entered in the input field is the scaled PML length *L*.

Once subdomain settings have been set, the boundary conditions of the subdomains need to be defined for the simulation. These are found under the Physics menu in COMSOL. In the RF module, the user can choose from the following boundary conditions: Magnetic Field, Surface Current, Perfect Magnetic Conductor, Electric Field, Perfect Electric Conductor, Scattering Boundary Condition, Matched Boundary, Impedance Boundary, Port, Periodic Condition, Lumped Port, or Circuit Port. Each of the selectable boundary conditions provided by COMSOL applies the properties for that condition to the general form of the boundary conditions shown in equations (A.2) and (A.3).

$$-\hat{n} \times (\mathbf{E}_2 - \mathbf{E}_1) = \mathbf{M_s} = 0 \tag{A.2}$$

$$\hat{n} \times (\mathbf{H}_2 - \mathbf{H}_1) = \mathbf{J_s} \tag{A.3}$$

For all interior boundaries of a simulation domain, the default boundary condition is set to Continuity by COMSOL. This condition ensures continuity of the tangential

components of the electric and magnetic fields by setting the boundary condition to that of equations (A.4) and (A.5)

$$\hat{n} \times (\mathbf{E}_1 - \mathbf{E}_2) = 0 \tag{A.4}$$

$$\hat{n} \times (\mathbf{H}_1 - \mathbf{H}_2) = 0 \tag{A.5}$$

For all exterior boundaries of a simulation domain, COMSOL's default boundary condition is a Perfect Electric Conductor. The boundary of the Perfect Electric Conductor, shown in equation (A.6), sets the tangential electric field component to zero.

$$\hat{n} \times \mathbf{E} = 0 \tag{A.6}$$

The user is able to change the default condition to any of the other conditions listed above. They will each be described as follows:

- The Magnetic Field and Electric Field conditions set the tangential field of the respective type to the value specified by the user.
- The Perfect Magnetic Conductor condition sets the tangential component of the magnetic field equal to zero.
- The Surface Current boundary condition allows the user to specify a surface current density on either an interior or exterior boundary. The surface current is specified as a three dimensional vector. Since the surface current must flow along the surface, COMSOL will project the given vector on to the surface. For an exterior boundary, the surface current equation is given by equation (A.7), and for interior boundary, given by equation (A.8).

$$-\hat{n} \times \mathbf{H} = \mathbf{J_s} \tag{A.7}$$

$$\hat{n} \times (\mathbf{H_1} - \mathbf{H_2}) = \mathbf{J_s} \tag{A.8}$$

- The Magnetic Potential condition allows the user to set the tangential component of the magnetic vector potential. This condition can be used to give a tangential electric field by integrating the desired value with respect to time.
- The Scattering Boundary Condition is utilized when the user wants the boundary to be transparent for a scattered wave. This boundary condition is also transparent to incoming plane waves. This condition can handle plane, cylindrical, and spherical scattered waves. The equation for the boundary condition for each type of wave is shown in equation (A.9)

$$\mathbf{E} = \begin{cases} \mathbf{E}_{sc} e^{-jk(\mathbf{n}\cdot\mathbf{r})} + \mathbf{E}_0 e^{-jk(\mathbf{k}\cdot\mathbf{r})} & \text{Plane Wave} \\ \frac{\mathbf{E}_{sc} e^{-jk(\mathbf{n}\cdot\mathbf{r})}}{\sqrt{r}} + \mathbf{E}_0 e^{-jk(\mathbf{k}\cdot\mathbf{r})} & \text{Cylindrical} \\ \frac{\mathbf{E}_{sc} e^{-jk(\mathbf{n}\cdot\mathbf{r})}}{r_s} + \mathbf{E}_0 e^{-jk(\mathbf{k}\cdot\mathbf{r})} & \text{Spherical} \end{cases} \tag{A.9}$$

  where $\mathbf{E}_0$ is the incident wave in the **k** direction.
- The Matched Boundary Condition is utilized at boundaries that do not represent a physical boundary at a system. It is often used to make a boundary totally nonreflecting. When the electric field is being solved and is the dependent variable, the Matched Boundary Condition is transparent to TE and TEM modes, and is modeled by equation (A.10)

$$\hat{n} \times (\nabla \times \mathbf{E}) - j\beta(\mathbf{E} - (\hat{n} \cdot \mathbf{E})\hat{n}) = -2j\beta(\mathbf{E_0} - (\hat{n} \cdot \mathbf{E_0})\hat{n}) \tag{A.10}$$

  where $\mathbf{E_0}$ is the incident field and β is the propagation constant of the guided wave structure that the boundary condition is replacing.

- The Impedance Boundary Condition is used at boundaries where the fields are known to penetrate only a short distance outside the boundary, and is utilized in order to eliminate the need to create another simulation domain. The Impedance Boundary Condition is modeled by equation (A.11).

$$\sqrt{\frac{\mu_r \mu_0}{\varepsilon_c}}\ \hat{n} \times \mathbf{H} + \mathbf{E} - (\hat{n} \cdot \mathbf{E})\hat{n} = \ (\hat{n} \cdot \mathbf{E_s})\hat{n} - \mathbf{E_s} \qquad \text{(A.11)}$$

where ε_s and μ_r are the material properties for the domain outside the simulation domain. For equation (2.38) to be valid in the simulation, the term N = $\left|\sqrt{\frac{\mu\varepsilon_c}{\mu_1\varepsilon_1}}\right|$ must be much greater than 1, where μ_1 and ε_1 are the material properties for the inner domain.

- The Transition Boundary Condition is utilized on interior boundaries to model a thin sheet of conducting or dielectric medium. The surface impedance η is a function of the material properties of the sheet, and must be entered on the material properties tab of this boundary condition.
- The Lumped Port condition is used to model a voltage signal applied between two conductors.
- The Circuit Port condition is an extension of the Lumped Port condition, and is used to make connection to SPICE circuits. The condition sets a surface current equal to the current from a circuit node divided by the equivalent width of the boundary.

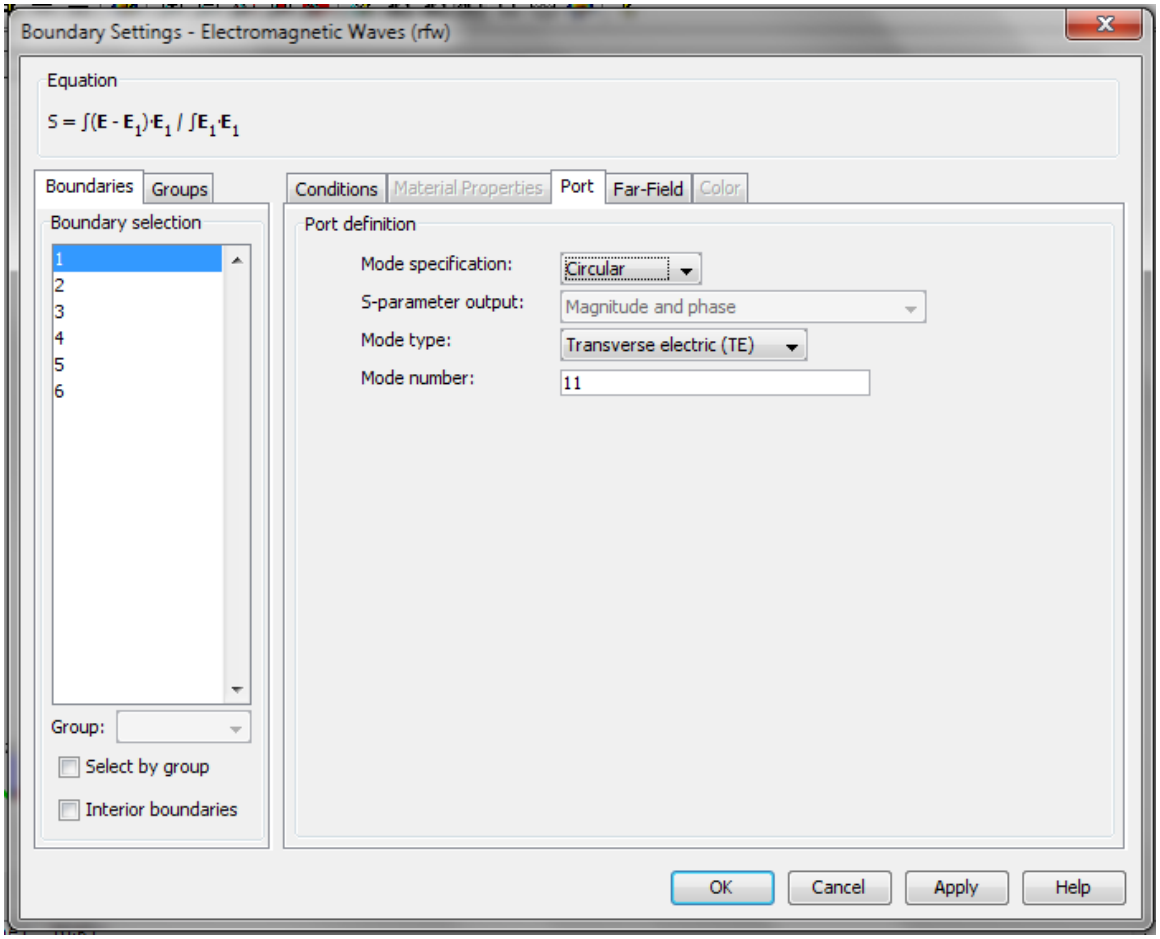

Figure A.3: Port tab for the Port boundary condition in COMSOL Multiphysics 3.5a.

- The Port boundary condition sets the same boundary condition as the Matched Boundary Condition, but allows functionality for generating S parameters. On the coefficients tab of the Port condition, the user can enter the input power level and phase. The most control over the Port condition is on the port tab, as shown in Figure A.3. The user is able to specify the mode specification from a list of user defined, rectangular, circular, numeric, or coaxial. The user defined option lets the user enter expressions for the fields manually. The numeric mode imports data from the boundary mode analysis application mode. The rectangular,

circular, and coaxial modes all apply to a port of homogeneous media. For the rectangular and circular modes, the user specifies the Mode type as either Transverse Electric (TE) or Transverse Magnetic (TM) and the Mode number. For a mode of TE_{mn}, the Mode number would be represented by an entry of "mn."

Once the subdomain and boundary settings are set in the simulation, the simulation domain must be meshed. Meshing is the act of partitioning the subdomains and boundaries into elements such that a selected solver can solve the model. COMSOL provides numerous methods for meshing geometries that includes free, mapped, extruded, revolved, swept, and boundary layer meshes. For the work done in this thesis, the free meshing method was used. In the free mesh method, the number of mesh elements and the shape of them are determined by the shape of the geometry. The default mesh shape is tetrahedron. The user is able to customize the size of mesh elements by setting constraints at the global, subdomain, boundary, edge, and point levels. All of the constraints are presented at the global level, and can be further constrained at lower levels to include only certain subdomains, boundaries, edges, etc.

COMSOL provides a list of predefined mesh sizes that range from extremely fine to extremely coarse. The user can also customize a predefined mesh size by modifying the maximum element size, maximum element scaling factor, element growth rate, mesh curvature factor, mesh curvature cutoff, and resolution of narrow regions. The maximum element size specifies the maximum allowed element size, which by default is set to one tenth of the maximum distance in the geometry. The maximum element scaling factor scales the maximum element size, and has a default value of one. The element growth rate determines the maximum rate at which the element size grows from a region of small

elements to a region with large elements. The value must be greater than or equal to one. The mesh curvature factor determines the size of boundary elements compared to the curvature of a geometric boundary. A lower value will give a finer mesh along curved boundaries. The maximum allowed element size along the boundary is equal to the curvature radius of the boundary multiplied by the curvature factor. The mesh curvature cutoff field will prevent too many elements around curved parts of a geometry, which prevents excessive computation times. The resolution of narrow regions field allows the user to control the number of element layers created in narrow regions. Lastly, the optimize quality check box determines if an optimization process will be carried out at the end of the meshing process. This optimization is helpful when attempting to solve large 3D electromagnetic problems.

When solving large 3D electromagnetic problems with COMSOL, an iterative solver is used because direct linear solvers require too much memory, and if solvable, excessive computation times. Converging to a solution in an iterative solver depends on a stability, or Nyquist, criterion, related to the element size of the mesh. Therefore it is imperative to ensure a proper mesh is created. For 3D electromagnetic wave problems, the Nyquist criterion is such that there must be at least two mesh elements per wavelength everywhere in the geometry. In an iterative solver, due to the fact that a direct solver is used to solve subdomain and boundary equations in the coarsest mesh, it is desirable to be as close to the Nyquist criterion as possible in order to reduce memory usage and decrease computation time.

The iterative solver that works well for 3D electromagnetic wave problems is the generalized minimum residual method or GMRES. GMRES solves a linear system of the

form $A*x = b$ by approximating the exact solution by a vector in Krylov space that minimizes the norm of the residual. The specifics of the GMRES algorithm are presented in work by Saab and Schultz in [35]. At a high level, the GMRES method completes one step of the Arnoldi method (finding eigenvalues), then finds the eigenvalue that minimizes the norm of the residual, approximates the value of the vector x, and then repeats if the residual is not yet small enough. In COMSOL, a preconditioner is added to the GMRES method to provide convergence faster. The preconditioner is a matrix M such that $M^{-1}* A* x = M^{-1}*b$. The system converges faster due to the fact that the result of $M^{-1}* A$ is closer to the identity matrix. For most 3D electromagnetic problems, the geometric multigrid preconditioner is the best selection. Convergence to a solution for an iterative solver is implemented in COMSOL by the following convergence criterion, equation (A.4)

$$\rho|M^{-1}\,(b - Ax)| < tol \cdot |M^{-1}b| \tag{A.12}$$

where ρ is the factor in error estimate, set to 400 by default, M is the preconditioned matrix, and *tol* is the relative tolerance set in COMSOL, set to 10^{-6} by default. The solver will iterate until the condition in equation (A.4) is met, or until the maximum number of allowed iterations is achieved, at which point an error message is thrown.

After the solver converges to a solution, the results can be viewed in numerous ways that are all found in the postprocessing menu. Under the plot parameters selection from the postprocessing menu, the user can select from plots types that include the following: slice, isosurface, subdomain, boundary, edge, arrow, principal stress/strain, streamline, particle tracing, max/min, deformation, and animation. The type of plot that best depicts the solution is dependent on the area of interest and geometry of the object.

The user is also able to only look at particular portions of the solution using the cross-section plot parameters or the domain plot parameters under the post processing menu.

Two important quantities for 3D antenna problems are scattering parameters (S parameters) and far field radiation characteristics. Both of these quantities are accessed in the postprocessing menu. The S parameters are complex, frequency dependent matrices that describe the transmission and reflection of electromagnetic energy at various ports. The S parameter matrix is as follows for an *n* port device

$$S = \begin{bmatrix} S_{11} & \cdots & S_{1n} \\ \vdots & \ddots & \vdots \\ S_{n1} & \cdots & S_{nn} \end{bmatrix} \tag{A.13}$$

The S parameter matrix is utilized in the following relationship

$$\begin{bmatrix} b_1 \\ b_2 \\ \vdots \\ b_n \end{bmatrix} = [S] \begin{bmatrix} a_1 \\ a_2 \\ \vdots \\ a_n \end{bmatrix} \tag{A.14}$$

where the vector **a** is the incident wave and vector **b** is the reflected wave. From equations (A.13) and (A.14), it is shown that S_{11} is the forward reflection coefficient, S_{21} is the forward transmission coefficient from port 1 to port 2, S_{12} is the transmission from port 2 to port 1, etc. The S parameters can be calculated from known voltages, electric fields, or power levels. For high frequency problems where voltages are not a well defined entry into the simulation, COMSOL computes the S parameters using the electric field and/or the power flow. If the electric field pattern, $\mathbf{E}_n$, is known on a port, and assuming that the field are normalized with respect to the integral of the power flow

across each port cross section, the S parameters can be calculated by equations (A.15) and (A.16).

$$S_{nn} = \frac{\int_{port\ n}((\mathbf{E}_c - \mathbf{E}_n)\cdot \mathbf{E}_n^{\ *})dA_n}{\int_{port\ n}(\mathbf{E}_n \cdot \mathbf{E}_n^{\ *})dA_n} \tag{A.15}$$

$$S_{mn} = \frac{\int_{port\ m}(\mathbf{E}_c \cdot \mathbf{E}_m^{\ *})dA_m}{\int_{port\ m}(\mathbf{E}_m \cdot \mathbf{E}_m^{\ *})dA_m} \tag{A.16}$$

where $\mathbf{E}_c$ is the computed electric field on the port, which consists of the excitation electric field and the reflected electric field, and *m* is any port that is not the excitation port *n*. If the magnitude of the S parameters is only necessary, they are calculated using the power flow. This is advantageous because the electric field patterns $\mathbf{E}_n$ does not need to be known. The definition of the S parameters in terms of power flow is found in equation (A.17).

$$S_{mn} = \sqrt{\frac{\text{Power reflected from port } m}{\text{Power incident on port } n}} \tag{A.17}$$

The power flow is given by the time average Poynting vector, $\mathbf{S}_{av}$, and the power flow out of a port is given by the normal component of the Poynting vector, as show in equation (A.18).

$$\mathbf{n} \cdot \mathbf{S}_{\text{av}} = \mathbf{n} \cdot \frac{1}{2}\,\text{Re}(\mathbf{E} \times \mathbf{H}^*) \tag{A.18}$$

If the wave mode is known, the power flow can be expressed in terms of the electric field and the impedance. These relationships are shown in equations (A.19) to (A.21).

$$\mathbf{n} \cdot \mathbf{S}_{\text{av}} = \frac{1}{2\, Z_{TE}} |\mathbf{E}|^2 \tag{A.19}$$

$$\mathbf{n} \cdot \mathbf{S}_{\text{av}} = \frac{1}{2\, Z_{TM}} |\mathbf{n} \times \mathbf{E}|^2 \tag{A.20}$$

$$\mathbf{n} \cdot \mathbf{S}_{\text{av}} = \frac{1}{2\, Z_{TEM}} |\mathbf{E}|^2 \tag{A.21}$$

where Z_{TE} is equal to $\frac{\omega\mu}{\beta}$, Z_{TM} is equal to $\frac{\beta}{\omega\varepsilon}$, and Z_{TEM} is equal to $\sqrt{\frac{\mu}{\varepsilon}}$, and β is the propagation constant, μ is the permeability, ω is the angular frequency, and ε is the permittivity.

The far field is also at interest because it defines how the antenna will behave at regions at large distances from the radiating source. It is defined as the region of space where the electric and magnetic field are orthogonal to each other and form TEM waves. The fields radiated by an antenna are spherical waves close to the source. The amplitude variation due to the radius r in each component (r,θ,φ) are of the form $1/r^n$. By neglecting higher order terms of $1/r^n$, the r variations are separable from the θ and φ terms, and can be seen that the radiated electric and magnetic fields only have θ and φ components in the far field region. A full derivation of this fact is found in [4].

To enable far field calculation, a variable must be declared on the desired boundaries in the far field tab under boundary settings in COMSOL. The far field is calculated from the near field on the boundary from the Stratton-Chu formula, which is found in equation (A.22).

$$\mathbf{E}_p = \frac{jk_0}{4\pi} \mathbf{r}_0 \times \int [\mathbf{n} \times \mathbf{E} - \eta_0 \mathbf{r}_0 \times (\mathbf{n} \times \mathbf{H})] \exp(jk_0 \boldsymbol{r} \cdot \boldsymbol{r}_0)\, dS \tag{A.22}$$

where **E** and **H** are the fields at the aperture, the surface S enclosing the antenna, $\mathbf{r}_0$ is the unit vector pointing from the origin to the point *p*, **n** is the unit normal vector to the surface S, η_0 is the free space wave impedance, k_0 is the free space wave number, **r** is the radius vector of the surface S, and $\mathbf{E}_p$ is the calculated far field at point *p*. Note that the far field radiation pattern is with respect to power. Because the far field is computed in free space, $\mathbf{H} = \frac{\mathbf{r}_0 \times \mathbf{E}_p}{\eta_0}$, and thus the pointing vector is proportional to the square of the magnitude of the electric field, $\mathbf{E}_p$. In COMSOL, the field pattern is returned to the variable normEfar, and the power pattern in the variable normEfardB.

Appendix B: Electric Field per Input Power$^{1/2}$ Graphs

This appendix shows the plots of the Electric Field / Power$^{1/2}$ for all taper lengths discussed in Chapter 4. For a given taper length, the first plot shows the studied modes with a dielectric window for an index of refraction of 1.6, the second plot for an index of refraction of 2.1, and the third plot for an index of refraction for 3.1.

15 cm Taper length

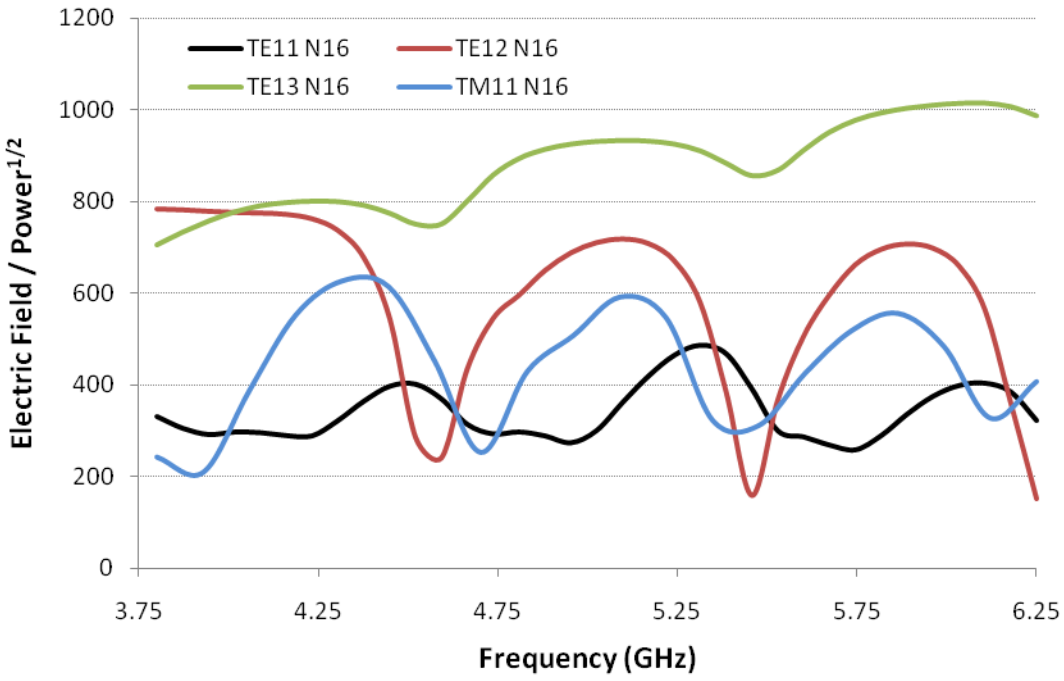

Figure B.1: Taper length of 15 cm and refractive index equal to 1.6.

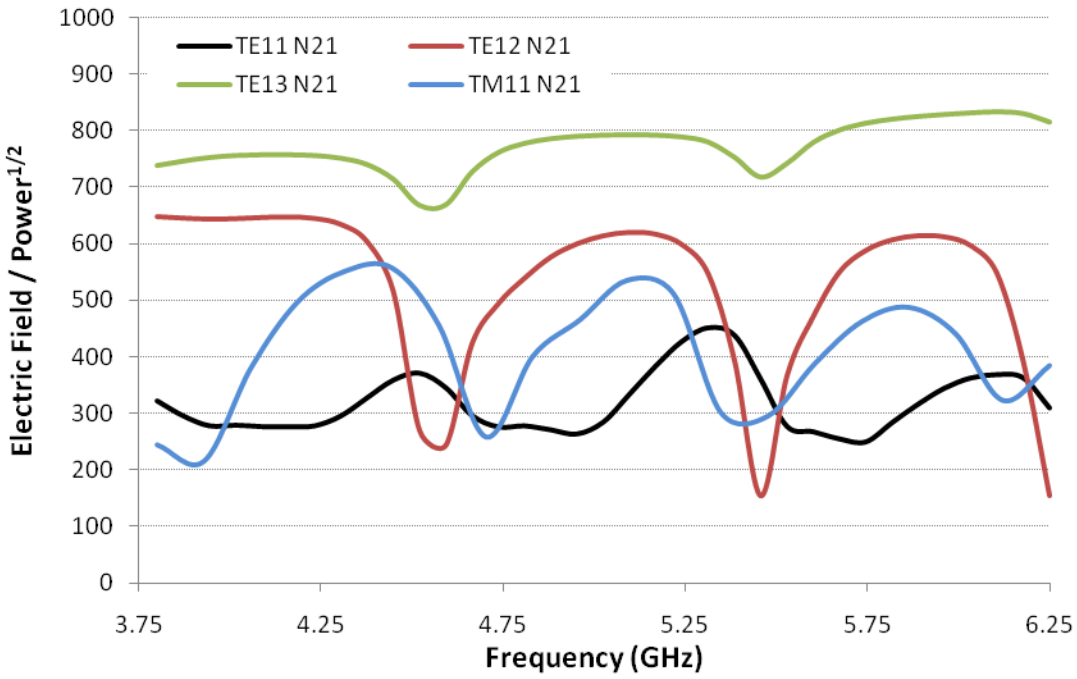

Figure B.2: Taper length of 15 cm, refractive index equal to 2.1.

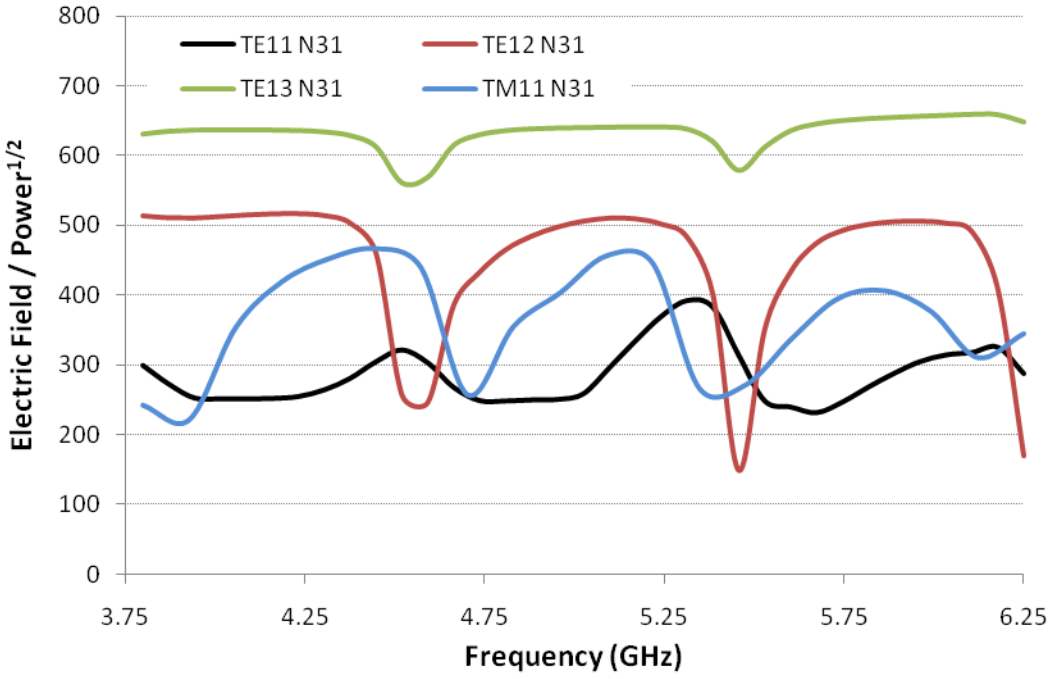

Figure B.3: Taper length of 15 cm, refractive index equal to 3.1.

17.2 cm Taper Length

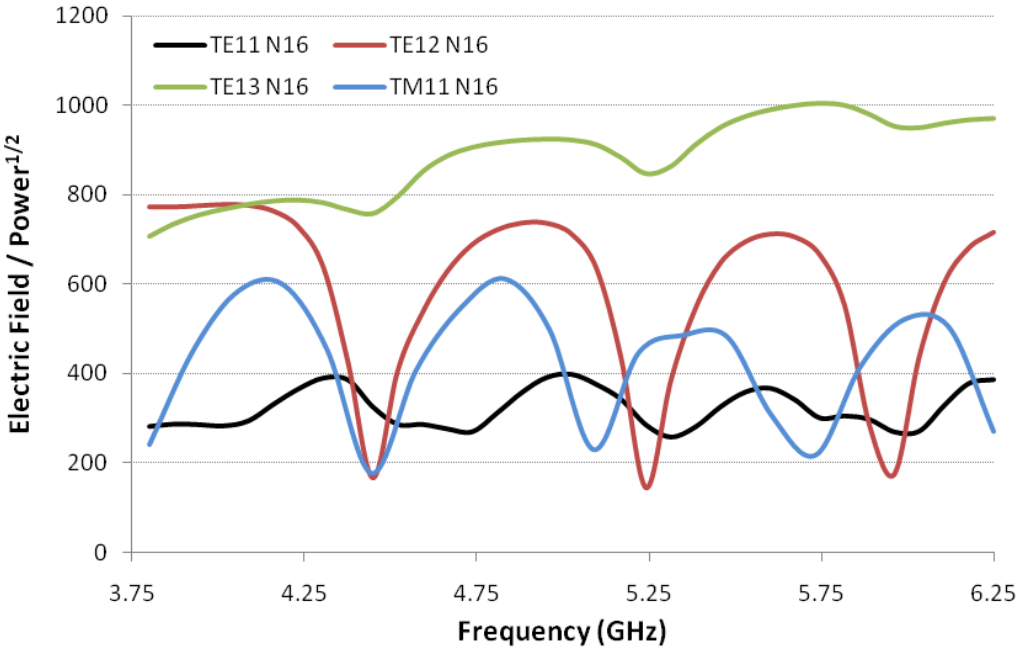

Figure B.4: Taper length of 17.2 cm, refractive index equal to 1.6.

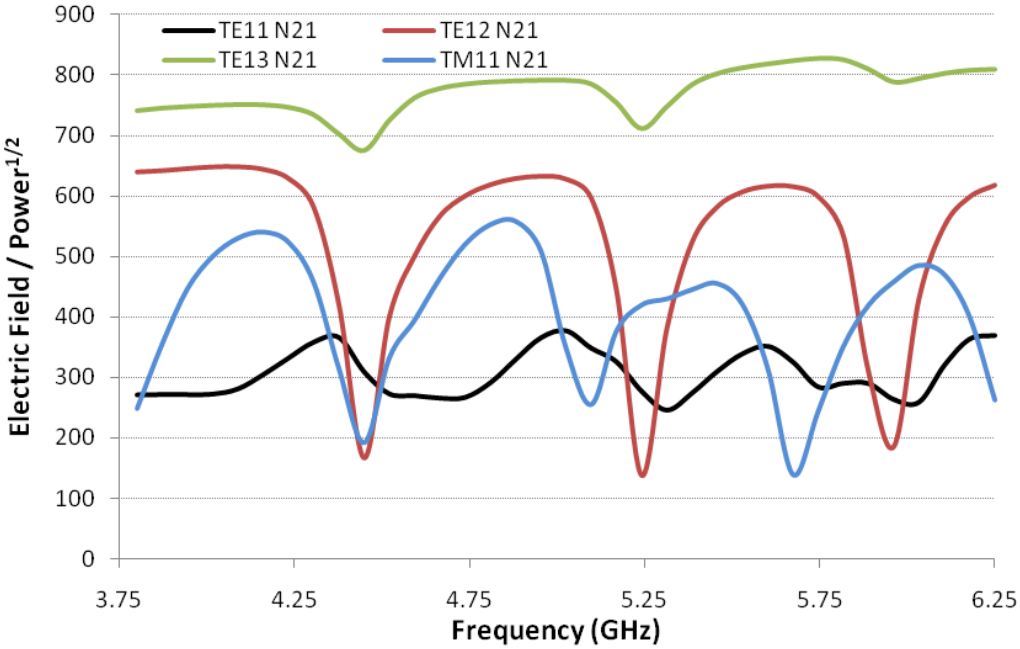

Figure B.5: Taper length of 17.2 cm, refractive index of 2.1.

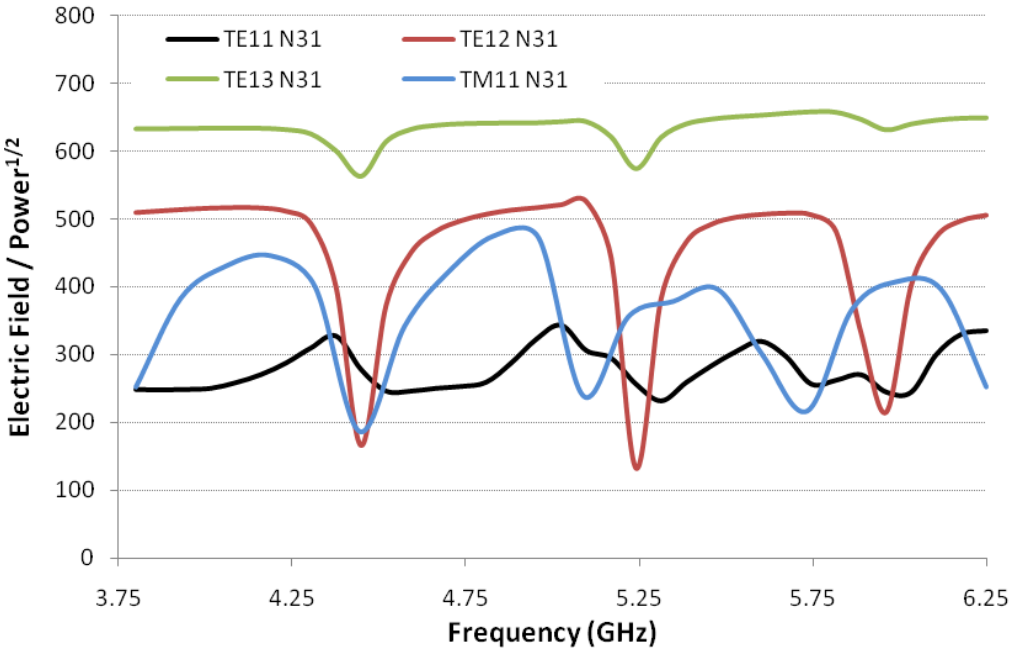

Figure B.6: Taper length of 17.2 cm, refractive index of 3.1.

19.2 cm Taper Length

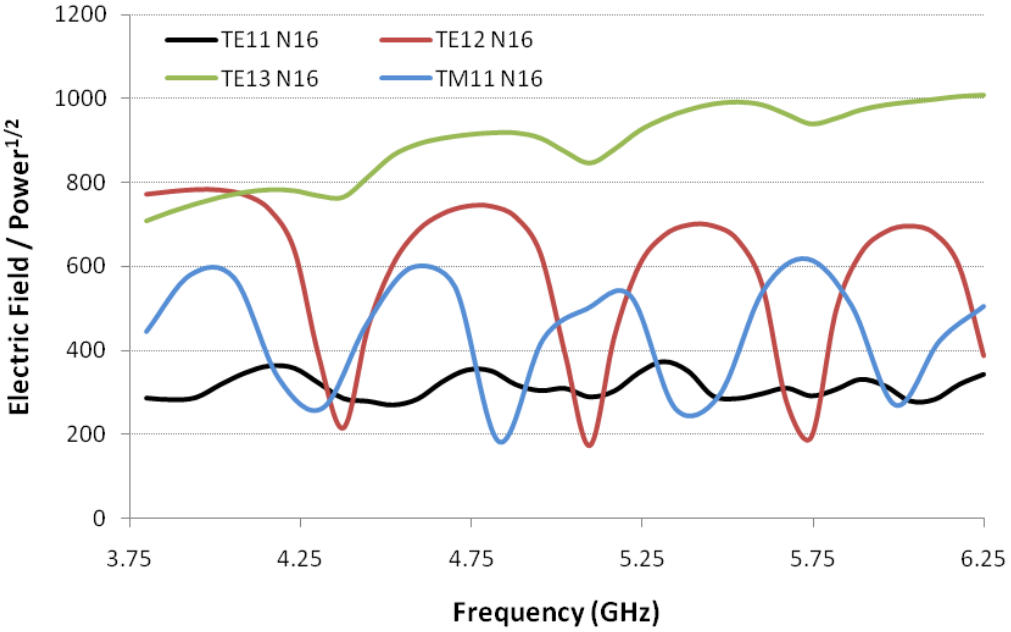

Figure B.7: Taper length of 19.2 cm, refractive index of 1.6.

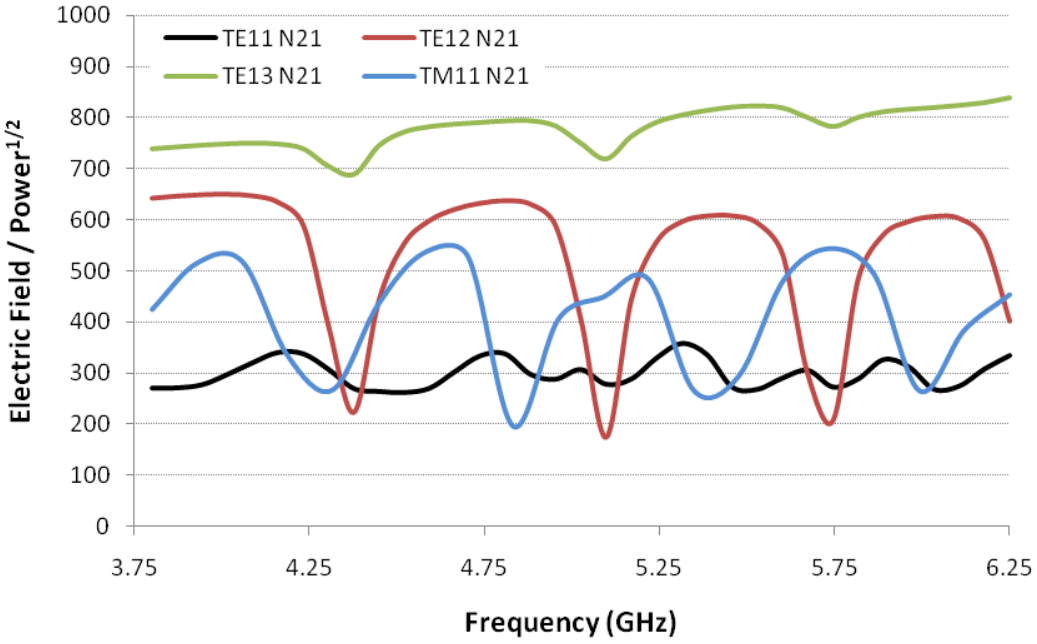

Figure B.8: Taper length of 19.2 cm, refractive index of 2.1.

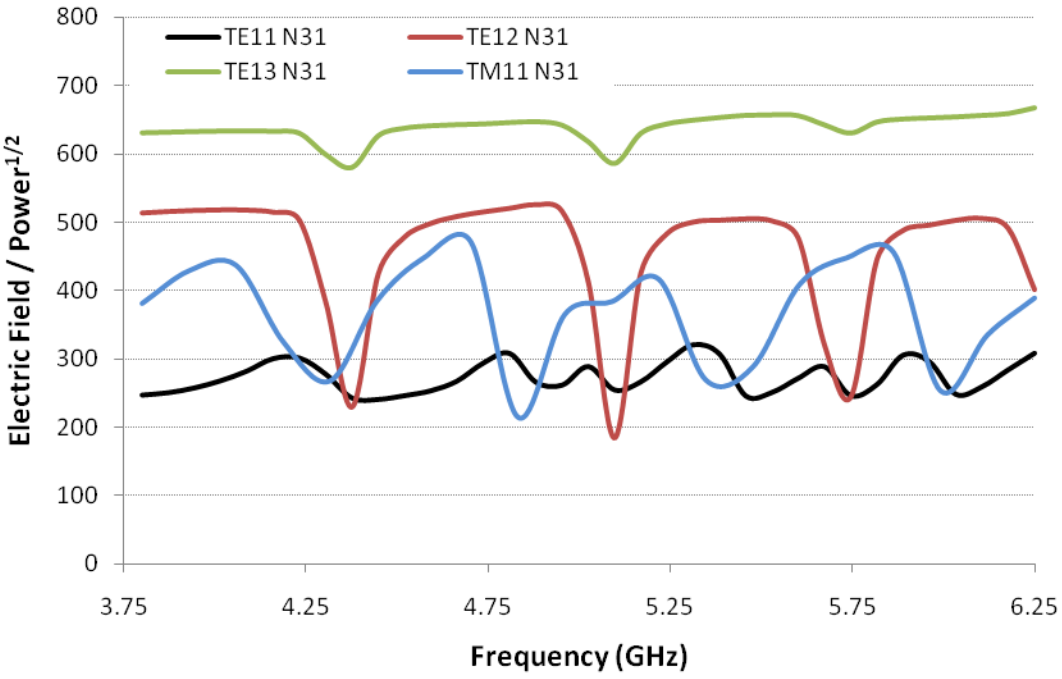

Figure B.9: Taper length of 19.2 cm, refractive index of 3.1.

20.4 cm Taper length

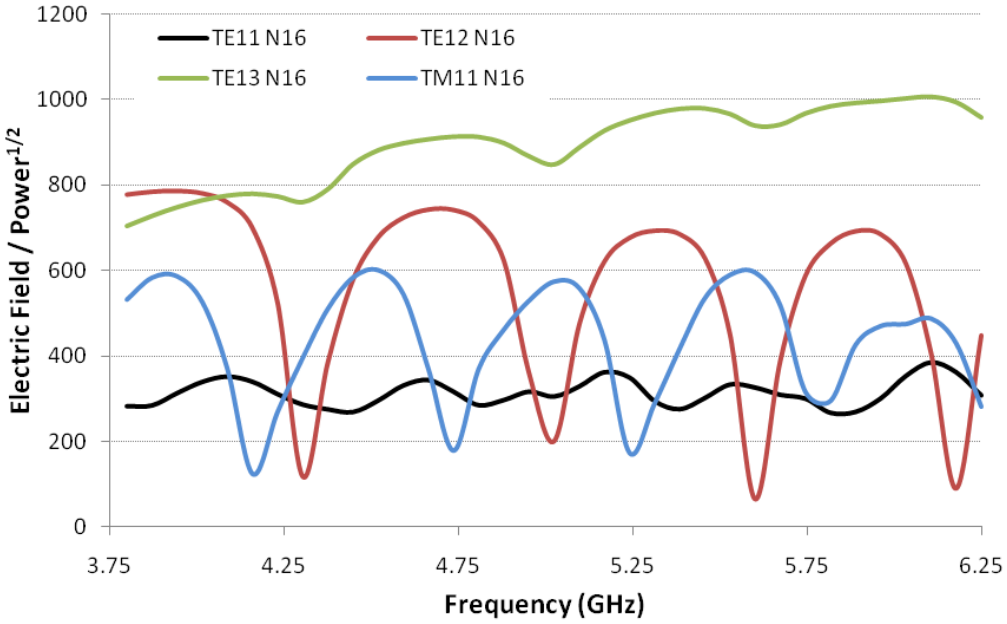

Figure B.10: Taper length of 20.4 cm, refractive index equal to 1.6.

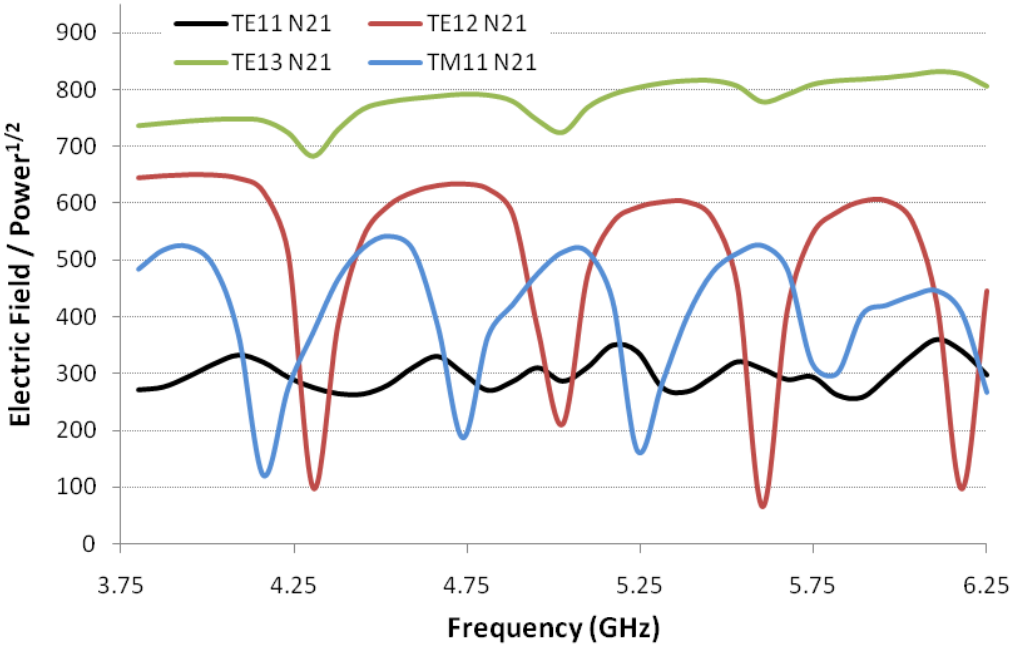

Figure B.11: Taper length of 20.4 cm, refractive index equal to 2.1.

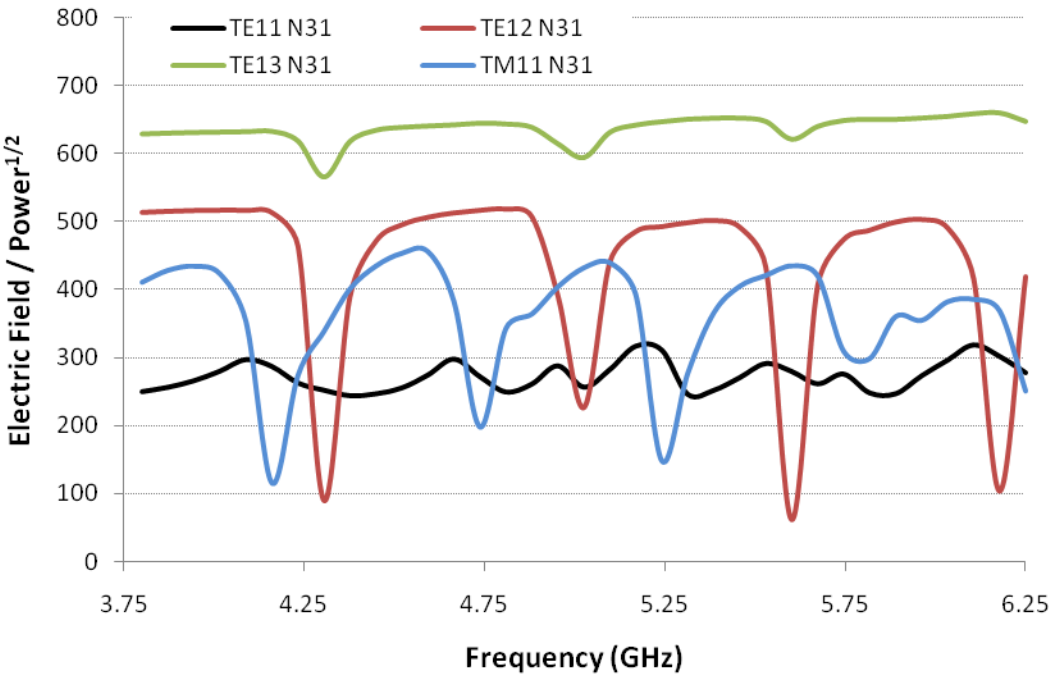

Figure B.12: Taper length of 20.4 cm, refractive index equal to 3.1.

25.4 cm Taper length

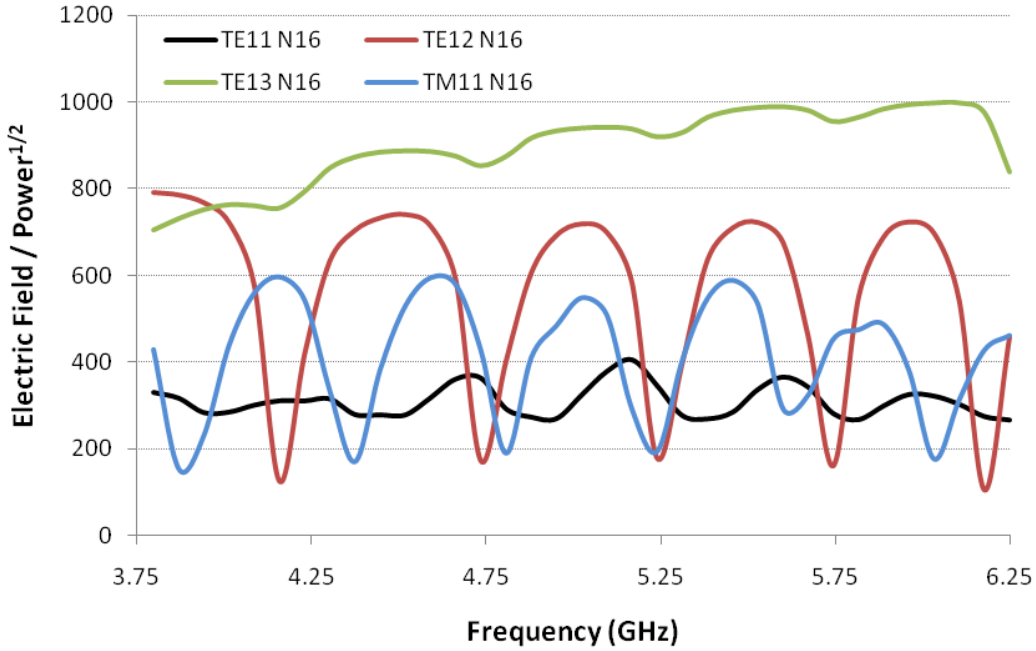

Figure B.13: Taper length of 25.4 cm, refractive index equal to 1.6.

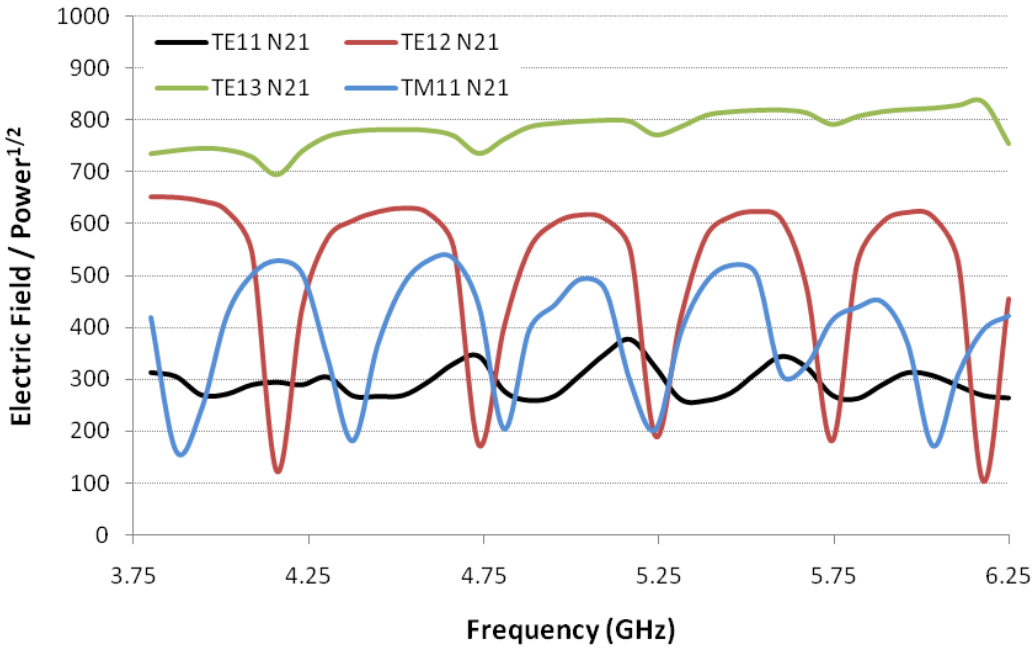

Figure B.14: Taper length of 25.4 cm, refractive index equal to 2.1.

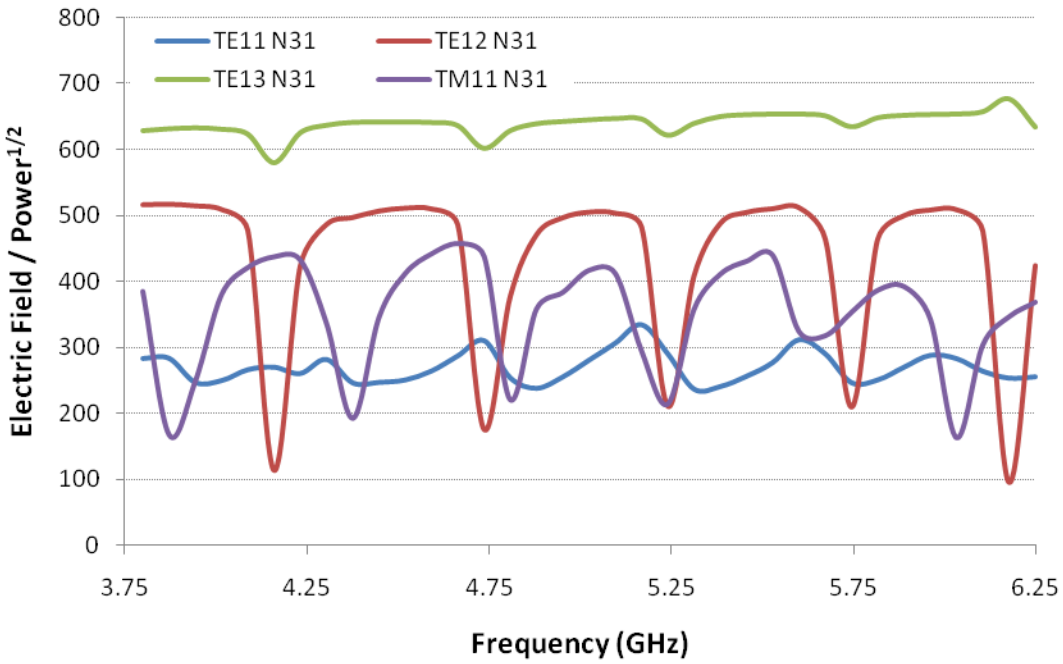

Figure B.15: Taper length of 25.4 cm, refractive index equal to 3.1.

29 cm Taper Length

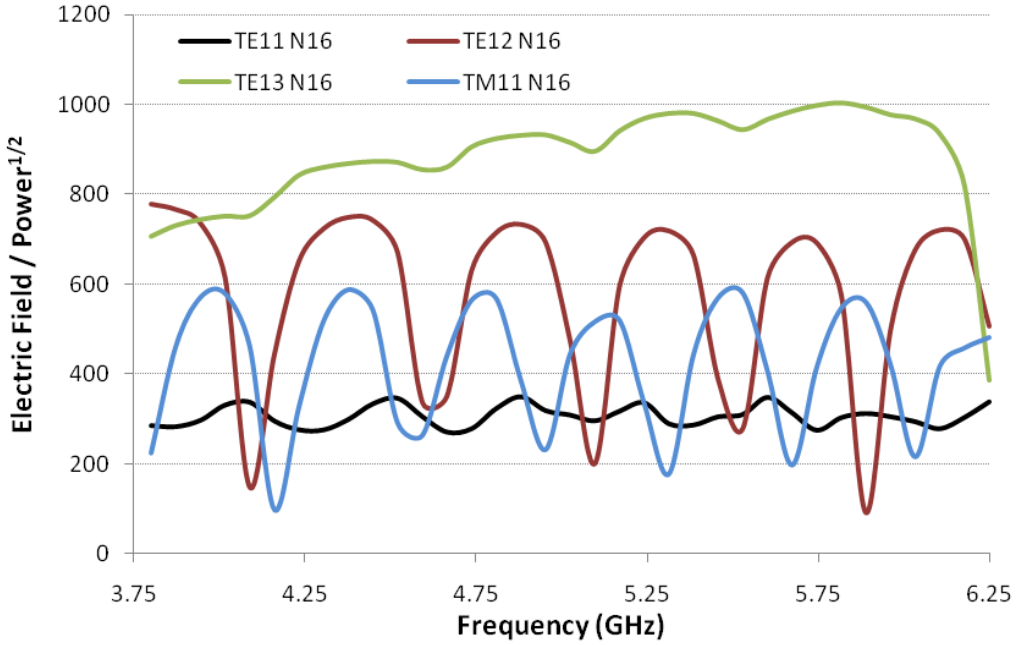

Figure B.16: Taper length of 29 cm, refractive index equal to 1.6.

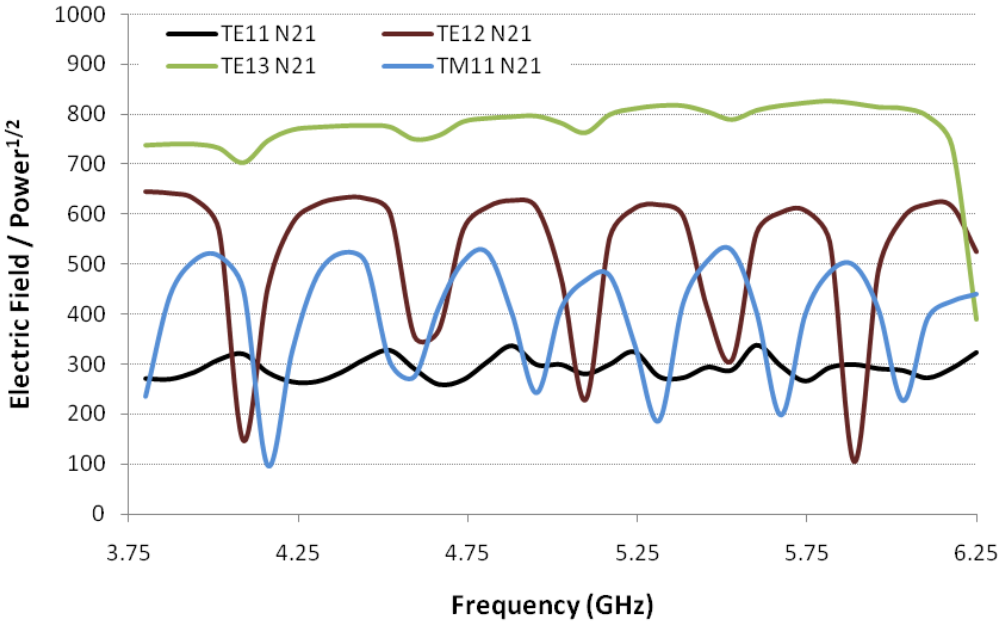

Figure B.17: Taper length of 29 cm, refractive index equal to 2.1.

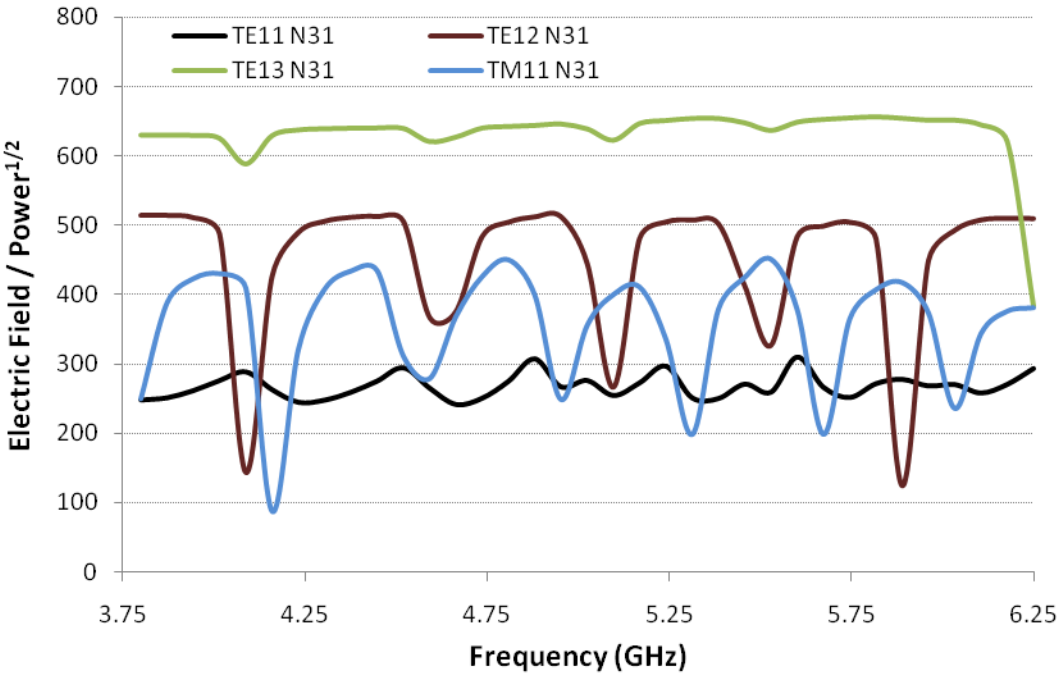

Figure B.18: Taper length of 29 cm, refractive index equal to 3.1.

Appendix C: MATLAB Code for Calculating Max Electric Field and Regression Analysis

Main file – findMaxField.m

```
%% Analyze max field of window dielectric surface %%%
% Erik Becker   7/8/2010
%
%
close all;
clc;
clear all;

%% call user interface and get info.
global u0
global u1
global u3
global cont
global h

get_input_info

cont = 1;
while(cont)
    pause(1);
end
pause(.25);

export_to_excel = get(u0,'Value');
S_param_on = get(u1,'Value');
only_one_file = get(u3,'Value');
close(h);
pause(1);

%% import data of interest and format it
load param_col

%get file names to analyze -> user enters files with
TangentialFieldxxxx.
if only_one_file == 1
    [filename, ext, user_canceled] =
uigetfile('*.txt','MultiSelect','Off');
    numFiles = 1;
else
    [dummyfilename, ext, user_canceled] =
uigetfile('*.txt','MultiSelect','On');
    temp = size(dummyfilename);
    numFiles = temp(2);
end

% for regCoeff export
```

```
excel_col = 0;
letter = 66;

for snuffleupogus = 1:numFiles
    pos1  = [350,200,270,55];
    WB = waitbar(0,'Please wait...','Position',pos1);

    if only_one_file ~= 1
       filename = dummyfilename{1,snuffleupogus};
    end
    % file names must be changed each time!!!!
    importfile([ext filename]);
    WB = waitbar(.05);

    test = strrep(filename,' ', '');
    test = strrep(test,'.txt','');
    dataIn = eval(test);
    identifier = strtok(filename,'T');
    identifier = ['T' identifier];

    %add in second input file if it exits.
    exists = strfind(filename, '1 to 200');
    k = size(exists);
    if k(1) ~= 0
        test = strrep(filename,'1 to 200','201 To 350');
        importfile([ext test]);
        test = strrep(test,' ', '');
        test = strrep(test,'.txt','');
        temp = eval(test);
        temp(:,3) = temp(:,3)+200;
        dataIn = [dataIn; temp];
    end

    WB = waitbar(.1);

    sizeBigFile = size(dataIn);
    sizeParam = size(colParams);

    %get number of sample points for each solution

    temp = 1;
    while dataIn(temp,3) == 1
        temp = temp+1;
    end

    graphSize = temp-1;

    dummyTemplate = zeros(graphSize,4);

    for i = 1:sizeParam(1)

        eval(sprintf('Param%d = dataIn((i-1)*graphSize+1:(i-
1)*graphSize+graphSize,:);',i));
```

```
    end

    % find max field for each
    MaxField = zeros(sizeParam(1),3);

    for i = 1:sizeParam(1)
        eval(sprintf('[maxF index] = max(Param%d(:,4));',i));
        MaxField(i,3) = maxF;
        eval(sprintf('MaxField(i,1) = Param%d(index,1);',i));
        eval(sprintf('MaxField(i,2) = Param%d(index,2);',i));
    end

    WB = waitbar(.3);
    % note function show_param_plot will display any surface of
    % parameters
    finalData = [colParams MaxField];

    %% make graphs

    %find number of frequencies used by finding how many powers
    %Frequency is column 2, Power Column 3, Column 6 is max field,
Column 4 is
    %x of max field, and column 5 is y of max field

    testValue = finalData(1,3); %get first power level
    count = 1;
    while finalData(count,3) == testValue
        count = count+1;
    end

    numFrequencies = count-1;
    numPowers = sizeParam(1)/numFrequencies;

    PowerLevel = zeros(numPowers,1);

    for i = 1:numPowers
        PowerLevel(i,1) = finalData((i-1)*numFrequencies+1,3);
        %[frequency maxField]
        eval(sprintf('freqPlot%d = [ finalData((i-
1)*numFrequencies+1:(i-1)*numFrequencies+numFrequencies, 2)
finalData((i-1)*numFrequencies+1:(i-
1)*numFrequencies+numFrequencies,6)];',i));
    end

    % plot the Max fields for each power vs frequency

    % HARDCODED ONE DAY TRY TO FIGURE OUT HOW TO STOP THIS  know there
are 10
    % powers
    WB = waitbar(.5);
    figure(1)
    plot(freqPlot1(:,1), freqPlot1(:,2), freqPlot2(:,1),
freqPlot2(:,2), freqPlot3(:,1), freqPlot3(:,2), ...
```

```
        freqPlot4(:,1), freqPlot4(:,2), freqPlot5(:,1), freqPlot5(:,2),
freqPlot6(:,1), freqPlot6(:,2), ...
        freqPlot7(:,1), freqPlot7(:,2), freqPlot8(:,1), freqPlot8(:,2),
freqPlot9(:,1), freqPlot9(:,2), ...
        freqPlot10(:,1), freqPlot10(:,2));
    legend(num2str(PowerLevel));
    xlabel('Frequency');
    ylabel('Peak Electric Field');

    % do normailzed plots
    temp = 0;
    for i = 1:numPowers
        eval(sprintf('temp =
freqPlot%d(:,2)./max(freqPlot%d(:,2));',i,i));
        eval(sprintf('freqPlot%d = [freqPlot%d temp];',i,i));
    end

    figure(2)
    plot(freqPlot1(:,1), freqPlot1(:,3), freqPlot2(:,1),
freqPlot2(:,3), freqPlot3(:,1), freqPlot3(:,3), ...
        freqPlot4(:,1), freqPlot4(:,3), freqPlot5(:,1), freqPlot5(:,3),
freqPlot6(:,1), freqPlot6(:,3), ...
        freqPlot7(:,1), freqPlot7(:,3), freqPlot8(:,1), freqPlot8(:,3),
freqPlot9(:,1), freqPlot9(:,3), ...
        freqPlot10(:,1), freqPlot10(:,3));
    legend(num2str(PowerLevel));
    xlabel('Frequency');
    ylabel('Peak Electric Field');

    % freq plot -> col 1 = frequency, col 2 is peak field, col 3 is
normalized

    constant = zeros(numFrequencies,numPowers);

    for j = 1:numPowers
    for i = 1:numFrequencies

        % const = peak field * inputpower / normalized field
        eval(sprintf('constant(i,j) =
freqPlot%d(i,1)/freqPlot%d(i,3)*PowerLevel(j,1);',j,j));

    end
    end

    % plot for a given frequency

    PowerY = zeros(numPowers,numFrequencies);

    for j = 1:numFrequencies
    for i = 1:numPowers
        eval(sprintf('PowerY(i,j) = freqPlot%d(j,2);',i));
    end
    end
```

```
    figure(3)
    for i = 1:numFrequencies
        plot(PowerLevel, PowerY(:,i));
        hold on;
    end
    xlabel('Power Level');
    ylabel('Peak Electric Field');

    temp = [PowerLevel PowerY];
    exportfile = strrep(filename,'.txt','');
    exportfile2 = strrep(filename,'.txt','');
    exportfile = [exportfile ' PowerVsField'];
    exportfile2 = [exportfile2 ' PeakVsFreq'];

    WB = waitbar(.75);

    if export_to_excel == 1
        try
            delete([exportfile '.xls']);
            delete([exportfile2 '.xls']);
        catch ME1
        end

        warning off MATLAB:xlswrite:AddSheet
        %header = freqPlot1(:,1)';
        header = cell(1,35);
        for i = 1:numFrequencies
            %header(i) = java.lang.String(num2str(freqPlot1(i,1)));
            header{i} = sprintf('%.3e', freqPlot1(i,1));
        end
        xlswrite(exportfile, header, 'Test','B1:AJ1');
        xlswrite(exportfile, {'PowerLevel'}, 'Test', 'A1:A1');
        xlswrite(exportfile, temp,'Test', 'A2:AJ11');

        WB = waitbar(.8);

        %B is 66
        j = 66;
        blah = 0;
        %warning off all
        for i = 1:numFrequencies
            if blah == 1
                h = [65 j];
            else
                h = j;
            end

            temp =
sprintf('=EXP(INTERCEPT(LN(%s2:%s11),LN($A$2:$A$11)))',h,h);
            range = sprintf('%s12:%s12',h,h);
            xlswrite(exportfile,{temp},'Test',range);
            j = j+1;
            if j == 91
                blah = 1;
                j = 65;
```

```
            end

        end


        %read in regression coefficients
        regCoefficients = xlsread(exportfile, 'Test', 'B12:AJ12');
        regCoefficients = [freqPlot1(:,1)'; regCoefficients];
        regCoefficients = regCoefficients';
        figure(4)
        plot(regCoefficients(:,1), regCoefficients(:,2));

    end

    %Brian's 'superior' way to find regression coefficients
    regCoeff = zeros(numFrequencies,1);
    for i = 1:numFrequencies
        temp2 = polyfit(log(PowerLevel(:,1)),log(PowerY(:,i)),1);
        regCoeff(i,1) = exp(temp2(2));
    end

    figure(5)
    plot(freqPlot1(:,1)',regCoeff);
    xlabel('Frequency');
    ylabel('Power Law Regression Coefficient');

    if export_to_excel == 1
        %export power levels
        header = {'Frequency ' 'Peak Electric Field ' 'Normalized Peak
Electric Field'};
        for i = 1:numPowers
            tab = sprintf('Power%d',PowerLevel(i,1));
            %dataToWrite = sprintf('freqPlot%d;',i);
            xlswrite(exportfile2,header,tab,'A1:C1');
            eval(sprintf('temp = freqPlot%d;',i));
            xlswrite(exportfile2,temp,tab,'A2:C36');
        end
    end

    WB = waitbar(.9);

    if S_param_on == 1
        Sparam = get_S_param(identifier,numFrequencies);
        figure(6)
        plot(Sparam(:,1), Sparam(:,2));
    end
    xlabel('Frequency');
    ylabel('S11');

    %normalize coefficients and S param and graph on the same
    figure(7)
    normRegCoeff = regCoeff./max(regCoeff);
    plot(freqPlot1(:,1)',normRegCoeff);
    hold on;
```

```
    if S_param_on == 1
        normSparam = zeros(numFrequencies,1);
        temp = Sparam(:,2)./max(Sparam(:,2));
        normSparam = temp;
        plot(Sparam(:,1), normSparam, 'Color', 'red');
    end
    xlabel('Frequency');
    ylabel('normalized data');
    legend('regression coefficients', 'Sparam');
    WB = waitbar(.95);


    %save relevant data to file to make graphs....  only if look at
many files
    if only_one_file ~= 1
        regFilename = 'regressionCoeffData.xls';
        if snuffleupogus == 1
            delete(regFilename);
        end
        tab = 'Regression Data';
        textToWrite = 'Frequency';
        xlswrite(regFilename,{textToWrite},tab,'A1');
        textToWrite = identifier;

        if excel_col == 1
           ha = [65 letter];
        else
           ha = letter;
        end

        %letter = 65;  moved up top

        cellToWrite = sprintf('%s1',ha);
        xlswrite(regFilename,{textToWrite},tab,cellToWrite);

        xlswrite(regFilename,freqPlot1(:,1),tab,'A2');
        cellToWrite = sprintf('%s2',ha);
        xlswrite(regFilename,regCoeff(:,1),tab,cellToWrite);

        letter = letter+1;
        if letter == 91
           excel_col = 1;
           letter = 65;
        end

    end

    WB = waitbar(1);
    close(WB);

end
```

References

[1] J. Benford, J. A. Swegle, and E. Schamiloglu, *High Power Microwaves, Second Edition*, 2nd ed. Taylor & Francis, 2007.

[2] R. J. Barker and E. Schamiloglu, *High-Power Microwave Sources and Technologies*, 1st ed. Wiley-IEEE Press, 2001.

[3] R. Cairns and A. Phelps, *Generation and Application of High Power Microwaves: Proceedings of the Forty Eighth Scottish Universities Summer School in Physics, St Andrews, August ... 48.)*, 1st ed. Taylor & Francis, 1997.

[4] C. A. Balanis, *Antenna Theory: Analysis and Design, 3rd Edition*, 3rd ed. Wiley-Interscience, 2005.

[5] F. Olsson, M. Jansson, D. Aberg, M. Karlsson, and B. Bergman, "Experiments and Simulations of a Compact UWB Pulse Generator Coupled to an Exponential Flared TEM-Horn Antenna," in *IEEE International Power Modulators and High Voltage Conference, Proceedings of the 2008*, pp. 405-408, 2008.

[6] F. Olsson, M. Jansson, D. Aberg, M. Karlsson, B. Bergman, and R. Beverly, "High Power Radiating System Based on a Compact Printed Circuit Board Marx Generator," in *IEEE International Power Modulators and High Voltage Conference, Proceedings of the 2008*, pp. 529-531, 2008.

[7] D. V. Giri, *High-power Electromagnetic Radiators: Nonlethal Weapons and Other Applications*. Harvard University Press, 2004.

[8] W. Prather et al., "Ultra-wideband source and antenna research," *Plasma Science, IEEE Transactions on*, vol. 28, no. 5, pp. 1624-1630, 2000.

[9] A. V. Gaponov-Grekhov and V. L. Granatstein, *Applications of High-Power Microwaves*. Artech House Publishers, 1994.

[10] J. McSpadden and J. Mankins, "Space solar power programs and microwave wireless power transmission technology," *Microwave Magazine, IEEE*, vol. 3, no. 4, pp. 46-57, 2002.

[11] W. Brown and E. Eves, "Beamed microwave power transmission and its application to space," *Microwave Theory and Techniques, IEEE Transactions on*, vol. 40, no. 6, pp. 1239-1250, 1992.

[12] V. Baryshevsky, A. Borisevich, A. Gurinovich, G. Drobyshev, P. Molchanov, and A. Senko, "A compact high power microwave (HPM) source," in *Pulsed Power Conference, 2009 IET European*, pp. 1-4, 2009.

[13] A. Young et al., "A Compact, Self-Contained High Power Microwave Source Based on a Reflex-Triode Vircator and Explosively Driven Pulsed Power," in *IEEE International Power Modulators and High Voltage Conference, Proceedings of the 2008*, pp. 147-150, 2008.

[14] D. Price, "Compact pulsed power for directed energy weapons," *J. Directed Energy*, vol. 1, no. 48, 2003.

[15] Y. J. Chen, A. A. Neuber, J. Mankowski, J. C. Dickens, M. Kristiansen, and R. Gale, "Design and optimization of a compact, repetitive, high-power microwave system," *Review of Scientific Instruments*, 2005. .

[16] S. Calico, M. Scott, and M. Clark, "Development of a compact Marx generator for high-power microwave applications," in *Pulsed Power Conference, 1997. Digest of*

Technical Papers. 1997 11th IEEE International, vol. 2, pp. 1536-1541 vol.2, 1997.
[17] T. Holt, A. Young, M. Elsayed, J. Walter, A. Neuber, and M. Kristiansen, "Images From the Development of a High-Power Microwave System," *Plasma Science, IEEE Transactions on*, vol. 36, no. 4, pp. 1414-1415, 2008.
[18] E. Schamiloglu, K. Schoenbach, and R. Vidmar, "On the road to compact pulsed power: adventures in materials, electromagnetic modeling, and thermal management," in *Pulsed Power Conference, 2003. Digest of Technical Papers. PPC-2003. 14th IEEE International*, vol. 1, pp. 3-8 Vol.1, 2003.
[19] Y. Minamitani, Y. Ohe, and Y. Higashiyama, "Nanosecond High Voltage Pulse Generator Using Water Gap Switch for Compact High Power Pulsed Microwave Generator," *Dielectrics and Electrical Insulation, IEEE Transactions on*, vol. 14, no. 4, pp. 894-899, 2007.
[20] C. Davis, A. Neuber, A. Young, J. Walter, J. Dickens, and M. Kristiansen, "Optimization of an FCG-Based High-Power Microwave System Using Nonexplosive Pulsed Power," *Plasma Science, IEEE Transactions on*, vol. 37, no. 12, pp. 2321-2327, 2009.
[21] J. Gardelle, B. Cassany, T. Desanlis, P. Modin, and J. Donohue, "Production of high power microwaves with a compact Marx generator," in *Plasma Science, 2004. ICOPS 2004. IEEE Conference Record - Abstracts. The 31st IEEE International Conference on*, p. 279, 2004.
[22] B. Cassany, T. Desanlis, P. Eyl, A. Galtie, P. Modin, and L. Voisin, "Prototype of a high power compact Marx generator for microwave applications," in *Pulsed Power Conference, 2003. Digest of Technical Papers. PPC-2003. 14th IEEE International*, vol. 2, pp. 1177-1179 Vol.2, 2003.
[23] P. Appelgren et al., "Study of a Compact HPM System With a Reflex Triode and a Marx Generator," *Plasma Science, IEEE Transactions on*, vol. 34, no. 5, pp. 1796-1805, 2006.
[24] J. Walter, J. Dickens, and M. Kristiansen, "Performance of a compact triode vircator and Marx generator system," in *Pulsed Power Conference, 2009. PPC '09. IEEE*, pp. 133-137, 2009.
[25] R. K. Livesley, *Finite Elements: An Introduction for Engineers*, First Edition. Cambridge University Press, 1983.
[26] S. S. Quek and G. Liu, *Finite Element Method: A Practical Course*. Butterworth-Heinemann, 2003.
[27] D. H. Norrie and G. D. Vries, *Introduction to Finite Element Analysis*. Academic Press Inc, 1978.
[28] M. G. Schorr and F. J. Beck, "Electromagnetic Field of the Conical Horn," *Journal of Applied Physics*, vol. 21, no. 8, p. 795, 1950.
[29] A. King, "The Radiation Characteristics of Conical Horn Antennas," *Proceedings of the IRE*, vol. 38, no. 3, pp. 249-251, 1950.
[30] "Horn Antennas," in *Antenna Handbook: Theory, Applications and Design (Y. T. Lo and S. W. Lee)*, New York: Van Nostrand Reinhold Co., 1988.
[31] A. W. Love, "Horn Antennas," in *Antenna Engineering Handbook (R. C. Johnson and H. Jasik)*, New York: , 1984.
[32] W. Burnside and C. Chuang, "An aperture-matched horn design," *Antennas and Propagation, IEEE Transactions on*, vol. 30, no. 4, pp. 790-796, 1982.

[33] C. A. Balanis, *Advanced Engineering Electromagnetics*, Solution Manual. Wiley, 1989.
[34] COMSOL, Inc, "COMSOL Multiphysics Help Guide."
[35] Y. Saad and M. H. Schultz, "GMRES: A Generalized Minimal Residual Algorithm for Solving Nonsymmetric Linear Systems," *SIAM Journal on Scientific and Statistical Computing*, vol. 7, no. 3, pp. 856-869, Jul. 1986.
[36] C. Lee, S. Lee, and S. Chuang, "Plot of Modal Field Distribution in Rectangular and Circular Waveguides," *Microwave Theory and Techniques, IEEE Transactions on*, vol. 33, no. 3, pp. 271-274, 1985.
[37] A. Neuber, J. Dickens, D. Hemmert, H. Krompholz, L. Hatfield, and M. Kristiansen, "Window and cavity breakdown caused by high power microwaves," in *Pulsed Power Conference, 1997. Digest of Technical Papers. 1997 11th IEEE International*, vol. 1, pp. 135-140 vol.1, 1997.
[38] J. Krile, G. Edmiston, J. Dickens, H. Krompholz, and A. Neuber, "Window Flashover Initiation under Pulsed Microwave Excitation," in *IEEE International Power Modulators and High Voltage Conference, Proceedings of the 2008*, pp. 560-563, 2008.
[39] G. Edmiston, A. Neuber, L. McQuage, J. Krile, H. Krompholz, and J. Dickens, "Contributing Factors to Window Flashover under Pulsed High Power Microwave Excitation at High Altitude," *Dielectrics and Electrical Insulation, IEEE Transactions on*, vol. 14, no. 4, pp. 783-789, 2007.
[40] P. F. Goldsmith, *Quasioptical Systems: Gaussian Beam Quasioptical Propogation and Applications*. Wiley-IEEE Press, 1997.
[41] J. Walter, "Private Communication. 2010.."
[42] S. Cornbleet, *Microwave and Geometrical Optics*. Academic Press, 1994.
[43] F. L. Pedrotti, L. M. Pedrotti, and L. S. Pedrotti, *Introduction to Optics*, 3rd ed. Benjamin Cummings, 2006.
[44] D. M. Pozar, *Microwave Engineering*, 2nd ed. Wiley, 1997.
[45] R. E. Collin, *Foundations for Microwave Engineering*, 2nd ed. Wiley-IEEE Press, 2000.
[46] *COMSOL*. COMSOL, Inc.